

USE OF MRI TO STUDY EXCITOTOXIC SPINAL CORD INJURY

By

SARA ANN BERENS

A DISSERTATION PRESENTED TO THE GRADUATE SCHOOL
OF THE UNIVERSITY OF FLORIDA IN PARTIAL FULFILLMENT
OF THE REQUIREMENTS FOR THE DEGREE OF
DOCTOR OF PHILOSOPHY

UNIVERSITY OF FLORIDA

2006

Copyright 2006

by

SARA ANN BERENS

This document is dedicated to my fiancé, Jason, and my family for their continued love and encouragement.

ACKNOWLEDGMENTS

First, I would like to thank my committee members, Drs. Robert Yeziarski, Tom Mareci, Steve Blackband, and Doug Anderson, for their guidance and encouragement. Each has contributed to my development as a scientist in many different ways. I would like to thank my mentor, Dr. Yeziarski, for teaching me all there is to know about spinal cord injury and pain, as well as performing surgeries; Dr. Mareci, for shaping my knowledge of MR imaging, as well as showing me how to operate several of the magnet systems; Dr. Blackband, for providing me a foundation on the principles of MR Imaging; and Dr. Anderson for providing his expertise on spinal cord injury. I appreciate their encouragement to write as often as I did, through publications and grants; it made the final writing process less strenuous.

I am indebted to all of the current and former lab members of the Yeziarski and Mareci labs that I have had the opportunity to work with over the years. In particular, I would like to thank Dr. Chen-Guang Yu for performing some of the surgeries; Jacquie Rodgers, for moral support and lending a helping hand in the care of my animals; my lab mate, Chris King, for moral support, helping with surgeries and animal care when I could not be there, for sharing an understanding of similar frustrations, and for being a friend; and Victoria Henry, for her continued moral support and guidance, problem solving skills, all of our many lunch walks, and, most importantly, for being my “work mom.”

I appreciate all those who have contributed to my success in imaging, especially Danny Colvin and Christy Amwake, for building the surface coils; Evren Özarlan for

helping me collect and analyze my *in vitro* MR data; Lari McEdwards, Suril Patel, Matthew Feldman, and Aaron Richardson for providing assistance in data analysis; Ty Black for his expertise and problem solving on the analysis software; and Nelly Volland, Chris Taylor, Min Sig Hwang, Hector Sepulveda, Lan Hoang Minh, Allan Elfström, Matthew Feldman, and Rashid Jawdat for providing me the opportunity to take a lunch break during my many long hours of imaging.

I would also like to give credit to the Advanced Magnetic Resonance Imaging and Spectroscopy (AMRIS) facility in the McKnight Brain Institute of the University of Florida and the staff. I thank Raquel Torres and Xeve Silver for their help in placing tail vein catheters and general technical support; Barbara Beck and Kelly Jenkins, for their expertise in coil setup, designing the volume coil, and helping me solve signal and tuning problems; Gary Blaskowski, for technical support and making sure the instrument ran smoothly; and Jim Rocca and Dan Plant for checking up on me and making sure everything was running properly. I am also grateful for the significant financial support provided by the McKnight Brain Institute.

I would also like to thank Dr. Joseph Riley for his expertise and help with complicated statistics.

On a more personal note, I would also like to thank my family for their continuous love, support, and encouragement throughout the years, and for shaping me to become the person I am today. The countless phone calls and emails helped combat stress, allowing me to keep my sanity. My fiancé, Jason, deserves special recognition, for taking the brunt of my frustration, letting me vent when things got tough, enduring all of

my tribulations first hand, for caring and loving me, and for supporting me in all I set out to do, never allowing me to give up.

TABLE OF CONTENTS

	<u>page</u>
ACKNOWLEDGMENTS	iv
TABLE OF CONTENTS.....	vii
LIST OF TABLES.....	x
LIST OF FIGURES	xi
ABSTRACT.....	xiii
CHAPTER	
1 INTRODUCTION AND LITERATURE REVIEW	1
Spinal Cord Injury	1
Overview	1
Primary and Secondary Injury Mechanisms.....	2
Excitotoxic Model of Spinal Cord Injury.....	3
<i>In Vivo</i> Magnetic Resonance Imaging.....	4
Overview	4
Dynamic Contrast-Enhanced Magnetic Resonance Imaging, Blood-Spinal Cord-Barrier.....	6
<i>In Vitro</i> Magnetic Resonance Imaging.....	7
Neuroprotective Strategies for Treatment of Spinal Cord Injury	9
Overview	9
Neuroprotective Effects of Agmatine.....	10
2 METHODOLOGICAL DEVELOPMENT	13
Overview.....	13
Anesthetic/Experimental Drugs.....	13
Magnetic Resonance Imaging.....	15
Catheter Placement.....	15
4.7T Coil Development	15
11.1T Coil Development	16
Coil Setup.....	18
11.1T Revised Imaging Protocol.....	19

4.7T versus 11.1T Images	19
Magnetic Resonance Imaging Obstacles	20
Heating Effects of the 11.1T Imaging Protocol.....	20
Signal-to-Noise Ratio	23
3 EVALUATION OF THE PATHOLOGICAL CHARACTERISTICS OF SPINAL CORD INJURY WITH MAGNETIC RESONANCE IMAGING.....	25
Introduction.....	25
Materials and Methods	26
Animal Preparation.....	26
Intraspinal Injection Procedure.....	27
<i>In Vivo</i> MR Imaging.....	28
<i>In Vivo</i> High Resolution MR Imaging Data Acquisition	28
<i>In Vivo</i> DCE-MR Imaging Data Acquisition	30
<i>In Vitro</i> MR Microscopy	31
Histological Procedures.....	31
Data Analysis.....	32
Results.....	33
<i>In Vivo</i> High Resolution MR Imaging.....	33
<i>In Vivo</i> DCE-MR Imaging.....	37
<i>In Vitro</i> MR Microscopy	38
Histologic Findings	40
Discussion.....	41
4 USE OF MAGNETIC RESONANCE IMAGING TO STUDY THE NEUROPROTECTIVE EFFECTS OF AGMATINE FOLLOWING SPINAL CORD INJURY IN THE RAT	47
Introduction.....	47
Materials and Methods	48
Animals, Surgery, and <i>In Vivo</i> MR Imaging	48
Neuroprotection.....	48
<i>In Vivo</i> High-Resolution Magnetic Resonance Imaging Data Acquisition.....	48
<i>In Vivo</i> DCE-MR Imaging Data Acquisition	50
<i>In Vitro</i> Three-Dimensional MR Microscopy	51
Data Analysis.....	51
Volume Analysis	52
Results.....	53
<i>In Vivo</i> High Resolution Magnetic Resonance Imaging	53
<i>In Vivo</i> Dynamic Contrast-Enhanced Magnetic Resonance Imaging	60
Volume Analysis	62
Discussion.....	68

5	DIFFUSION WEIGHTED MR IMAGING OF THE EXCISED QUISQUALIC ACID LESIONED RAT SPINAL CORD	72
	Introduction.....	72
	Materials and Methods	73
	Animals, Surgery, and Neuroprotection.....	73
	<i>In Vitro</i> Three Dimensional MR Microscopy and Diffusion Weighted Imaging.....	73
	Data Analysis.....	74
	Results.....	75
	Discussion.....	85
6	CONCLUSION.....	90
	Summary of Findings	90
	Future Directions	91
	LIST OF REFERENCES.....	93
	BIOGRAPHICAL SKETCH	107

LIST OF TABLES

<u>Table</u>	<u>page</u>
4-1 Summary of Significant Differences in Longitudinal Profiles of Edema, Cavitation, and Blood Vessel Leakage, and BSCB Disruption.	67
4-2 Summary of Significant Differences in Volumes of Edema, Blood Vessel Leakage, and Cavitation.	67

LIST OF FIGURES

<u>Figure</u>	<u>page</u>
2-1 Comparison of MR images collected on the 4.7T magnet versus the 11.1T magnet.	20
2-2 Temperature measurements collected on the 4.7T and 11.1T magnets using a tissue equivalent phantom simulating rat abdomen.	22
2-3 Comparison of images collected with high versus low SNR on the 11.1T magnet.	24
3-1 Representative pathologic findings in the same animal (S05) at the same location observed <i>in vivo</i> (T2-weighted, TR/effective TE = 2000 ms/62.5 ms; NA = 6), <i>in vitro</i> (TR/TE = 2500 ms/20 ms; NA = 8), and in histologic sections. .	34
3-2 Sagittal images for all QUIS-injured animals.	35
3-3 Transverse images for all QUIS-injured animals.	36
3-4 Total injury lengths determined by using <i>in vivo</i> , <i>in vitro</i> , and histologic methods for each QUIS-injured animal.	37
3-5 Summary of <i>in vivo</i> , <i>in vitro</i> , and histologic data collected for a representative QL2 animal (S06).	38
3-6 Summary of <i>in vivo</i> , <i>in vitro</i> , and histologic data collected for a representative QL1 animal (X03).	39
4-1 Surgery and MR imaging timeline.	50
4-2 Representative T2-weighted (TR/effective TE = 2000 ms/62.5 ms; NA = 12) MR images for each injury/treatment group for each day.	54
4-3 Longitudinal profile of the presence of edema for all injury/treatment groups as determined from <i>in vivo</i> T2-weighted transverse MR images.	55
4-4 Longitudinal profile of the presence of cavitation for all injury/treatment groups as determined from <i>in vivo</i> T2-weighted transverse MR images.	56

4-5	Longitudinal profile of the presence of blood vessel leakage for all injury/treatment groups as determined from <i>in vivo</i> T2-weighted transverse MR images.	57
4-6	Longitudinal profile of the total pathology injury length (the presence of edema, blood vessel leakage, and cavitation combined) for all injury/treatment groups as determined from <i>in vivo</i> T2-weighted transverse MR images.	58
4-7	Summary of DCE-MRI BSCB disruption. Peak enhancement is represented as a percentage.	61
4-8	Volume of edema for all injury/treatment groups as determined from <i>in vivo</i> T2-weighted transverse MR images.	62
4-9	Volume of blood vessel leakage for all injury/treatment groups as determined from <i>in vivo</i> T2-weighted transverse MR images.	63
4-10	Volume of cavitation for all injury/treatment groups as determined from <i>in vivo</i> T2-weighted transverse MR images.	64
4-11	Volume of total injury (volume of edema, blood vessel leakage, and cavitation combined) for all injury/treatment groups as determined from <i>in vivo</i> T2-weighted transverse MR images (days 1, 3, 7, 15, and 25) and <i>in vitro</i> transverse 3D MRM images (day 30).	66
5-1	S_0 ($b = 100 \text{ s/mm}^2$) transverse MR image from a QUIS lesioned animal showing regions of interest drawn for analysis of the white matter.	76
5-2	S_0 ($b = 100 \text{ s/mm}^2$) transverse MR image from a QUIS lesioned animal showing regions of interest drawn for analysis of the gray matter.	76
5-3	Average diffusivity and fractional anisotropy values for Control white matter.	78
5-4	Average diffusivity and fractional anisotropy values for Saline-SCI white matter.	79
5-5	Average diffusivity and fractional anisotropy values for QUIS-SCI white matter.	80
5-6	Average diffusivity and fractional anisotropy values for Control gray matter.	81
5-7	Average diffusivity and fractional anisotropy values for Saline-SCI gray matter.	82
5-8	Average diffusivity and fractional anisotropy values for QUIS-SCI gray matter.	83
5-9	Probability maps calculated from diffusion weighted datasets collected from excised normal and QUIS injured spinal cords.	84

Abstract of Dissertation Presented to the Graduate School
of the University of Florida in Partial Fulfillment of the
Requirements for the Degree of Doctor of Philosophy

USE OF MRI TO STUDY EXCITOTOXIC SPINAL CORD INJURY

By

Sara Ann Berens

August 2006

Chair: Robert P. Yeziarski
Major Department: Neuroscience

Spinal cord injury (SCI) is an important cause of morbidity and mortality in modern society. Understanding the mechanisms responsible for acute and chronic spinal cord injury pathology as well as secondary consequences and the development of effective strategies for therapeutic intervention is of great clinical importance. Although most of what is known about the pathological changes associated with experimental SCI has come from histological studies, the ability to non-invasively characterize spinal cord pathology provides a way to study the temporal profile of pathological changes in the injured spinal cord using the same animal at multiple time points. A technique with the capability of achieving this objective is high-resolution magnetic resonance imaging (MRI), which is becoming a preferred method for the visualization of SCI. Three-dimensional magnetic resonance microscopy and diffusion weighted imaging (DWI) are additional techniques that can be used to study SCI. Collectively, these MRI methods were used to evaluate the progression of excitotoxic injury, including changes in pathology, blood-spinal cord-barrier integrity, and white and gray matter fiber tracts, as

well as evaluate the neuroprotective effects of a pharmacological agent with known neuroprotective properties on the excitotoxic lesion.

It was found that high-resolution MRI can be used to study experimental SCI quantitatively and qualitatively with high field magnets using customized coils and optimized methods. This method had the sensitivity to detect significant differences in pathological characteristics between two different strategies of injury, as well as effectively evaluate the progression of pathological changes longitudinally in the same animal. Magnetic resonance imaging had the capability to monitor the efficacy of a pharmacological agent with known neuroprotective properties to protect the injured spinal cord. Additionally, structure and orientation of white and gray matter fiber tracts were evaluated with sophisticated diffusion weighted MR imaging methods. Diffusion weighted MR imaging had the sensitivity to detect fiber patterns in a normal cord and reveal changes in fiber orientation in quisqualic acid lesioned spinal cords. With continued improvements and application of these techniques, it will be possible to determine additional insights into the mechanism responsible for the progression of secondary pathologic changes following spinal injury.

CHAPTER 1 INTRODUCTION AND LITERATURE REVIEW

Spinal Cord Injury

Overview

Spinal cord injury (SCI) is an important cause of morbidity and mortality in modern society (Dumont et al., 2001; Fehlings et al., 2001; Sekhon and Fehlings, 2001; Carlson and Gorden, 2002). An estimated 600,000 Americans are living with functional deficits due to SCI (Carlson and Gorden, 2002; Hulsebosch, 2002), with about 11,000 new cases each year, costing an estimated \$9.7 billion annually. At present, the recommended treatment for acute SCI is methylprednisolone, a drug that has been documented to affect several important components of spinal injury including inflammation and free-radical formation (Bracken, 2001; Xu et al., 2001; Rabchevsky et al., 2002). In spite of intense research directed to repair the injured spinal cord, current long-term treatment is limited to rehabilitative physiotherapy (Wells et al., 2003). Because the success of these strategies is highly variable, many patients with SCI remain physically impaired as a result of their injury (Dumont et al., 2001; Fehlings et al., 2001; Sekhon and Fehlings, 2001; Carlson and Gorden, 2002; Wells et al., 2003). Therefore, understanding the mechanisms responsible for acute and chronic spinal cord injury pathology as well as secondary consequences and the development of effective strategies for therapeutic intervention is of great clinical importance.

Primary and Secondary Injury Mechanisms

The pathophysiology of SCI involves both primary and secondary injury mechanisms. Primary injury is a direct result of mechanical trauma leading to hemorrhage, membrane disruption, and vascular damage. This initial insult initiates a progressive wave of secondary injury, which activates a cascade of pathophysiological mechanisms that exacerbate the injury. This spread of damage is thought to be due to activation of biochemical events leading to cellular death (apoptosis and necrosis). There are several mechanisms that contribute to this wave of destruction including breakdown of the blood-spinal-cord barrier (BSCB), ischemia, formation of free radicals and nitric oxide, invasion of neutrophils, activation of astrocytes and microglia, apoptosis of oligodendrocytes, Wallerian degeneration, and oxygen radical-mediated lipid peroxidation (Anderson et al., 1985; Hall et al., 1992; Anderson and Hall, 1993; Hausmann, 2003).

Following ischemic or traumatic SCI, there is a transient increase in extracellular excitatory amino acids (EAA), which results in glutamate receptor-mediated excitotoxic events (Mills et al., 2001). Activation of glutamate receptors initiates numerous intracellular signaling pathways, causing long-lasting pathological and ultimately functional deficits following SCI. Additionally, there is accumulation of intracellular sodium, producing edema and a concomitant elevation in intracellular calcium (Young et al., 1982; Stokes et al., 1983). Influx of calcium is also associated with glutamate receptor activation and the increased release of EAAs leading to activation of calcium-activated proteases (e.g., calpains), formation of free radicals, stimulation of nitric oxide synthase (NOS), activation of proteases and endonucleases, mitochondrial damage, and

induction of apoptosis (Lu et al., 2000; Carlson and Gorden, 2002; Germano et al., 2002; Hausmann, 2003; Kwon et al., 2004; Park et al., 2004; Profyris et al., 2004).

Following spinal cord injury, damage is not restricted to the spinal cord. Studies have shown that damage occurs to ascending pathways, leading to deafferentation of supraspinal structures (Yeziarski, 2002). With deafferentation, it is likely that cortical and subcortical regions could undergo significant reorganization, resulting in widespread supraspinal functional changes following spinal injury (Morrow et al., 2000). Recently, Lee et al. (2004) evaluated the role of apoptosis in the secondary injury of the brain following acute spinal injury. They found evidence for cell death in the sensorimotor cortex caused by injury. This would indicate that apoptosis can occur remotely in regions distant from the lesion epicenter. Similarly, evidence of apoptosis was found in the pyramidal cell layer of the motor cortex after spinal transection injury (Hains et al., 2003). Realizing that injury is not limited to the spinal cord, but can have remote effects on the brain, is important, because in designing therapeutic treatments, one needs to take into consideration all available targets in order to maximize potential sites of intervention.

Excitotoxic Model of Spinal Cord Injury

In recent years, studies have shown that there exists a striking similarity between clinical and experimental SCI pathophysiology. In order for an animal model to have clinical relevancy, it needs to imitate the pathological features of human SCI, as well as be reliable, consistent, and reproducible. The excitotoxic model of spinal cord injury is a reduced injury model that has been shown to result in pathological changes similar to those associated with traumatic and ischemic SCI (Yeziarski et al., 1993; Yeziarski et al., 1998) and parallels the pathological sequela associated with human SCI (Kakulas, 1987;

Bunge et al., 1993; Bunge et al., 1997). It is produced by the intraspinal injection of the AMPA/metabotropic receptor agonist, quisqualic acid (QUIS). Previous studies have shown that the excitotoxic injury model results in pathophysiological changes, pain behaviors, NMDA receptor phosphorylation and up-regulated gene expression for NMDA receptors, opioid peptides (PPE and PPD), substance P receptor, inflammatory genes (iNOS and COX-2), apoptotic genes (FAS-L and TNF-related apoptosis-inducing ligand, TRAIL), and cytokine genes (IL-1 β and TNF- α) (Yeziarski and Park, 1993; Yeziarski et al., 1993; Liu et al., 1997a; Brewer and Yeziarski, 1998; Yeziarski et al., 1998; Brewer et al., 1999; Schwartz et al., 1999a; Fairbanks et al., 2000; Morrow et al., 2000; Abraham et al., 2001; Gorman et al., 2001; Plunkett et al., 2001; Yeziarski, 2001; Pattany et al., 2002; Siddall et al., 2002; Yeziarski 2002; Yeziarski and Burchiel, 2002; Caudle et al., 2003; Yu et al., 2003; Yu and Yeziarski, 2005). The similarities between QUIS induced pathology and clinical pathology of SCI support the use of the excitotoxic model in the study of pathophysiology and secondary injury mechanisms following spinal injury. Another advantage of the excitotoxic injury model is that it does not produce the mortality, morbidity, or challenges with animal husbandry that result from ischemic or contusion models of injury.

***In Vivo* Magnetic Resonance Imaging**

Overview

Although most of what is known about the pathological changes associated with experimental SCI (i.e., edema, neuronal loss, hemorrhage, and cavitation) has come from histological studies, the ability to non-invasively characterize spinal cord pathology provides a way to study the temporal profile of pathological changes in the injured spinal cord using the same animal at multiple time points. A technique with the capability of

achieving this objective is high-resolution magnetic resonance imaging (MRI), which is becoming a preferred method for the visualization of SCI (Falconer et al., 1994; Ohta et al., 1999; Bilgen et al., 2000).

Clinically, MRI has been a useful tool for the study of secondary complications associated with SCI. For example, MRI can play an important role in the study of post-traumatic syringomyelia. The excitotoxic injury model has been shown to produce similar pathological changes to those observed in this condition (Yeziarski et al., 1993; Schwartz et al., 1999a). Considering the lack of understanding of the pathological mechanism responsible for cavity formation in the injured cord (Madsen et al., 1994), it may be possible to gain insight into the mechanism of cavitation using *in vivo* MR imaging at different time-points following excitotoxic SCI.

In the past, clinicians have relied on patient descriptions of behavioral changes in determining clinical outcome (Williams, 1990, Oakes, 1996). However, recently MRI has been used to monitor changes associated with intraspinal transplantation, graft-mediated functional recovery and changes in syrinx morphology after transplantation (Wirth et al., 2002), and to differentiate between cyst, scar, or tumor formation with the help of MR contrast agent administration (Schwartz et al., 1999a). With the importance and many uses for MRI, continued research is needed to enhance this technique and expand its uses to provide a better understanding of the mechanisms responsible for the pathological changes associated with SCI. For example, an important question related to SCI is the temporal profile of pathological changes in the acute and chronic stages post-injury. Using *in vivo* MRI, it is possible to monitor these changes in the same animal.

Dynamic Contrast-Enhanced Magnetic Resonance Imaging, Blood-Spinal Cord-Barrier

In recent years, the integrity of the BSCB has been studied using MRI. Normally, the BSCB maintains a highly regulated homeostatic environment in the spinal cord as a result of tight junctions between neighboring capillary endothelial cells surrounded by pericytes and astroglial foot processes (Purves et al., 2001). The BSCB functions to limit the penetration of a wide range of hydrophilic (water-soluble) molecules, proteins, and cellular elements into the spinal cord. This barrier is disrupted in spinal injury, making it permeable to toxic substances via vesicular transport from intravascular to interstitial spaces (Popovich et al., 1996). Dynamic contrast-enhanced MRI is a method for studying this disruption. Breakdown of the barrier is detected with the use of an exogenous, water-soluble, paramagnetic contrast agent, gadolinium-diethylene-triamine-pentaacetic, bis-methylamine (Gd). Normally, Gd circulates throughout body tissues except in the central nervous system (CNS) because of the highly regulated blood-nervous-tissue barrier. However, when the BSCB is disrupted, Gd can leak into the interstitial tissue; i.e., it no longer remains intravascular (Bilgen et al., 2001). These BSCB breaches can be observed with great sensitivity as an enhancement on T1-weighted MR images. Long-term analysis can also reveal how long the BSCB remains permeable.

Current studies have shown that the BSCB plays a vital role in activating and regulating secondary events following SCI, specifically, the post-traumatic inflammatory response and edema formation (Hausmann, 2003); however, the exact mechanism of SCI-induced inflammatory response is not fully understood. Following injury, there is an ischemic environment at the injury epicenter as well as in adjacent areas of the white

matter (Tator and Koyanagi, 1997). Edema develops and spreads, paralleling necrotic tissue at the epicenter (Tator and Fehlings, 1991). Changes further associated with this disruption of microvasculature networks include hemorrhage, vasospasm, thrombosis, and impaired autoregulation, which in turn leads to further breakdown of the BSCB (Tator, 1991; Tator and Fehlings, 1991). Disruption of the BSCB results in inflammatory invasion of neutrophils, macrophages, and T-cells (Bareyre and Schwab, 2003), which further contributes to secondary injury mechanisms (Lu et al., 2000; Hausmann, 2003; Kwon et al., 2004; Profyris et al., 2004). Understanding the time course of permeability of the BSCB and the subsequent pathological consequences would be of significant benefit to understanding the secondary mechanisms associated with spinal cord injury.

***In Vitro* Magnetic Resonance Imaging**

Three-dimensional magnetic resonance microscopy (3D MRM) and diffusion weighted imaging (DWI) are additional techniques that can be used to study SCI. These techniques allow for *in vitro* measurements, where motion artifacts are eliminated (Lemaire et al., 1990). This allows the signal-to-noise ratio (SNR) to be optimized. In addition, prolonged scan times and higher field strengths are not limiting factors (Guilfoyle et al., 2003). Both techniques allow for greater sensitivity in accessing macroscopic changes in the injured cord, and with DWI, the integrity of the white and gray matter can be evaluated, which is limited or not capable with conventional *in vivo* methods of MRI. Diffusion imaging is also sensitive in evaluating spinal cord axonal integrity, degree of injury, and extent of neuroprotection following injury (Ford et al., 1994a; Nevo et al., 2001), and can be used to detect cyst formation in gray matter following excitotoxic spinal cord injury, before conventional MRI is able to detect cavities (Schwartz et al., 1999b).

Diffusion weighted MR imaging is developing into an important tool to characterize the organization of white matter in the brain and spinal cord (Beaulieu, 2002; Guilfoyle et al., 2003). Diffusion imaging is based on intrinsic properties within gray and white matter, and relies on the phenomenon that water diffusion is highly anisotropic in tissues of the central nervous system. The overall tissue microstructure influences the mobility of diffusing water molecules, as the tissue components (i.e., myelin sheath and axon cellular membranes) act as barriers and create individual compartments. Diffusion characteristics are used to identify structural subtypes, where anisotropy is directly related to the geometry of the fibers (Beaulieu, 2002). The direction of fibers may be inferred by the direction of greatest water diffusion, and by seeking out adjacent anisotropic voxels, a fiber can be mapped (Melhem et al., 2002). Following spinal injury, there is a decrease in anisotropy; i.e., there are less geometric restrictions to water translational motion resulting in decreased preferential water diffusion in a particular direction. Having the capability to map white matter fibers allows for the determination of the effects of injury on selected sensory and motor fiber tracts in the white matter, which thus far is not apparent with other imaging techniques.

Following spinal cord injury, apoptosis of oligodendrocytes occurs, which leads to chronic demyelination, ultimately causing anterograde neurodegeneration of ascending and descending white matter tracts (Li et al., 1996; Crowe et al., 1997; Liu et al., 1997b; Yong et al., 1998; Springer et al., 1999; Hausmann, 2003). This process of disintegration of the axon from its myelin sheath and breakdown of axons is known as Wallerian degeneration. Oligodendrocytes appear to be the predominant cellular target of glutamate in white matter tissue. Recent studies have shown oligodendrocytes to be particularly

sensitive to excitotoxic insult (Yoshioka et al., 1996; Matute et al., 1997; McDonald et al., 1998). Diffusion weighted imaging has the capability of detecting changes associated with this progressive condition (Becerra et al., 1995; Werring et al., 2000; Thomalla et al., 2004).

Neuroprotective Strategies for Treatment of Spinal Cord Injury

Overview

An important consideration in the study of SCI is the fact that in the treatment of injury there is believed to be an optimal time for intervention. Secondary injury processes, including a number of cellular and biochemical cascades, are potential targets for neuroprotection (Amar and Levy, 1999; Dumont et al., 2001; Sekhon and Fehlings, 2001; Carlson and Gorden, 2002; Hausmann et al., 2002; Hulsebosch, 2002). Various neuroprotective strategies targeting secondary injury have been examined experimentally, including inhibitors of lipid peroxidation, nitric oxide, calpain, apoptosis, caspase, glutamate receptor antagonists, anti-inflammatory agents, and other compounds of uncertain mechanisms (Amar and Levy, 1999; Blight and Zimber, 2001; Hall, 2001). Strategies have been demonstrated to improve outcome after brain and spinal injury in pre-clinical studies, but are largely unsuccessful in clinical trials (Albers et al., 1995; Gaviria et al., 2000; Martinez-Vila and Sieira, 2001; Faden, 2002; Hong and Liu, 2003; Wells et al., 2003). Reasons for the failure may be that previous research strategies 1) do not address the therapeutic window and effective dose required for treatment optimization; and 2) only target a single injury mechanism (Yam et al., 2000; Tekkok and Goldberg, 2001; Akins et al., 2002; Faden, 2002; Wells et al., 2003). Spinal cord injury is a complex condition in which multiple cell death (apoptosis and necrosis) and cell signaling pathways are in delicate balance with one another (Amar and Levy, 1999;

Dumont et al., 2001; Carlson and Gorden, 2002). It is likely that a single drug with multiple targets or a combination drug treatment strategy that affects multiple components of the secondary injury cascade will exert superior neuroprotective efficacy (Carlson and Gorden, 2002; Faden, 2002; Wells et al., 2003). Therefore, understanding the temporal profile of different secondary injury processes, as well as the impact of agents with known neuroprotective effects, is critical in order to design a reasonable strategy of intervention.

Neuroprotective Effects of Agmatine

Previous studies have been carried out to examine the effects of putative neuroprotective agents on the spread of damage following excitotoxic injury (Yeziarski, 2002; Yu et al., 2003). One drug that has been shown to have therapeutic effects is the neurotransmitter/neuromodulator, agmatine. Agmatine $[(\text{NH}_2(\text{CH}_2)_4\text{NH}_2\text{C}(\text{NH}=\text{O})\text{HN})]$ is a butyl chain with a guanidino group at one end and an amino group at the other, and is synthesized by the decarboxylation of arginine. It meets the criteria for an endogenous neurotransmitter/neuromodulator in that a) it is synthesized in the central nervous system (Li et al., 1994; Li et al., 1995; Fairbanks et al., 2000); b) it is stored in axon terminals in association with storage vesicles (Reis et al., 1998); c) it can be released by depolarization (Reis and Regunathan, 1998); d) it is inactivated by reuptake and/or degraded enzymatically by agmatinase (Sastre et al., 1996; Sastre et al., 1997); and e) it can bind to (Anis et al., 1990) and modulate (Yang and Reis, 1999) the actions of the NMDA subclass of glutamate receptors.

Because of the polar character of agmatine, questions have come about as to the extent to which it crosses the blood-central nervous system-barrier. Evidence has indicated that agmatine administered peripherally does readily cross the barrier in a

concentration-dependant manner and has direct effects on the central nervous system (Piletz et al., 2003). In addition, there have been numerous studies (for review, see Nguyen et al., 2003) conducted in which systemically administered agmatine has affected phenomena mediated by central processing. However, there is no data suggesting a mechanism for such transport into nervous tissue, although an agmatinergetic transporter has been suggested (Nguyen et al., 2003).

Pharmacologically, treatment with exogenous agmatine is non-toxic (Gilad et al., 1996; Fairbanks et al., 2000), blocks NMDA receptors (Olmos et al., 1999; Yang and Reis, 1999), inhibits all isoforms of nitric oxide synthase (Auguet et al., 1995; Galea et al., 1996), reduces glutamate excitotoxicity (Fairbanks et al., 2000; Zhu et al., 2003), and exerts significant neuroprotective effects in models of ischemic brain injury (Gilad et al., 1996; Gilad et al., 2000), and traumatic and excitotoxic spinal injury (Fairbanks et al., 2000; Yu et al., 2000). Recently, it was shown that systemic treatment with agmatine significantly reduces neuronal loss (Fairbanks et al., 2000; Yu et al., 2000; Yu et al., 2003), improves locomotor function (Yu et al., 2000), and affects multiple signaling pathways following SCI. For example, molecular changes brought about by agmatine include inhibiting NF- κ B activity, up-regulating AKT activity, and down-regulating pain- and injury-related gene expression following excitotoxic and traumatic spinal cord injury. These data suggest that agmatine may serve as a multifaceted agent that targets many of the secondary processes involved in the mediation of cell death and the progression of secondary injury in SCI. The multiple sites of action of this endogenous molecule make agmatine a promising therapeutic agent for treatment of spinal cord injury and secondary

complications, as well as a useful pharmacological agent to study the impact of neuroprotective interventions with known therapeutic targets.

CHAPTER 2 METHODOLOGICAL DEVELOPMENT

Overview

During the course of experiments described in Chapters 3-5, new methodologies were learned and developed. With any new protocol, challenges arise that need to be addressed before the method is successful. Below is a description of these learned and newly developed procedures, as well as associated complications and solutions to address each issue.

Anesthetic/Experimental Drugs

With each experiment, there is a significant amount of preparation involved, from animal care, anesthetics, treatment, experimentation, to a successful recovery. With anesthetics, it is crucial to administer proper doses, as well as prepare correct concentrations of the anesthetic mixture. It is equally important that each component of the cocktail be high in quality and freshly mixed. When any one of these components is overlooked, problems can surface.

An example of a problem that occurred with anesthetics was encountered during post-surgery survival with the last group of animal surgeries. At first, the anesthetic used in Chapter 3 [mixture of ketamine (100 mg/mL, 3.0 mL), acepromazine (10 mg/mL, 1.0 mL), and xylazine (20 mg/mL, 3.0 mL; mixture at 0.65 mL/kg, subcutaneously)] was believed to be the cause of the problem. It was believed that during times of infrequent surgeries, the cocktail mixture could have deteriorated, so fresh mixtures were made. However, animals were still not surviving, regardless of post-operative care. After

talking with Animal Care Services and other labs using similar anesthetics on rats, a different cocktail recipe was developed [mixture of ketamine (100 mg/mL, 0.5 mL) and xylazine (100 mg/mL, 0.1 mL)] in hopes that rats would have a more successful recovery following surgery, and that the anesthetic would act more effectively, i.e., animals would remain anesthetized for the duration of surgery, with no supplements required. Tests were done with two doses of this new recipe (mixture at 0.75 mL/kg and 1.0 mL/kg) and through two different routes of administration (intraperitoneally versus subcutaneously). Based on results, it was decided that 1.0 ml/kg administered intraperitoneally was the most effective dose and route of administration. Intraspinous injection surgeries went on as scheduled, using the new cocktail recipe; however, animal survival was still an issue.

Next, we tested the experimental drug, agmatine, to determine if it was the cause of failed recovery. At first, it was suspected that the higher experimental dose (100 mg/kg) was too high, as there have been previous reports that higher doses of agmatine caused hypothermia (Yeziarski, unpublished observations). So, the dose was decreased to 80 mg/kg, however, this did not remedy the problem. To further test the agmatine, a fresh supply was made; one rat received a dose of the old supply and one rat received a dose of the fresh supply. The rat that received the old agmatine supply, died several hours later, while the one that received the fresh supply survived. Therefore, on the next scheduled surgeries, rats received the new anesthetic cocktail and a dose of the fresh Agmatine supply at the lower dose (80 mg/kg). However, after a third attempt, animals were still not surviving; they seemed to die due to respiratory distress. Once again, Animal Care Services was contacted and made aware of the problem in hopes that they might shed light on this ongoing problem. At this time, we discovered that the higher concentration

of xylazine (100 mg/mL vs 20 mg/mL) was known to cause pulmonary edema in rodents. Therefore, it was thought that the cocktail had never been the problem in the first place, and that the agmatine had been the main cause of animal survival problems. So, we switched back to the original cocktail recipe and used the fresh supply of agmatine (80 mg/kg), and finally the last group of animal surgeries were performed successfully, with no further survival issues. During the time the above problems were being addressed, a total of 16 animals were lost following preliminary MRI's and subsequent intraspinal injection of QUIS.

Magnetic Resonance Imaging

Catheter Placement

A tail vein catheter was needed to administer contrast agent used in the dynamic contrast-enhanced MR imaging. Placing a tail vein catheter requires patience and a great deal of practice to perfect. Once the animal was anesthetized with a mixture of oxygen and isoflurane, as described in Chapter 3, the catheter was filled with a heparin/sterile saline solution (also described in Chapter 3), and inserted into the tail vein. Correct placement was confirmed with blood flow into the catheter, at which point, 2-3 cc of the heparin/sterile saline solution was injected to prevent further clotting. The catheter was then taped in place.

4.7T Coil Development

Initial experiments were carried out on the 4.7T magnet system (please see Chapter 3). A highly-sensitive quadrature MR surface coil was constructed for this system, by Danny Colvin, specifically for imaging the rat spinal cord. The coil consisted of two rectangular coil elements (3 x 3 cm) placed next to each other on the inside of a half-cylinder cradle 4 cm in diameter. Each coil was constructed using copper tape, 5 mm in

width, with a 3.3 pF ceramic-chip capacitor (American Technical Ceramics (ATC), model 3R3C) inserted in series with the copper tape in the middle of each arc at the ends of each rectangle to provide distributed capacitance around the coil. The rectangular coils were overlapped along the inner edges to cancel their mutual inductance. The overlapping coils formed an arc of 120 degrees with an overall arc length of 5.5 cm. Each coil was individually tuned and matched with a combination of fixed series capacitors of 1 pF (ATC, model 1R0C) and variable series and parallel capacitors (Johanson Manufacturing Corp, Boonton, NJ, model 5641) arranged on a custom circuit board. The tune and match circuit was interfaced to the transmitter-receiver with an input-voltage balancing network on the same circuit board and a 50 ohm coaxial cable containing a parallel-resonance trap on the coaxial shield to eliminate surface currents. The trap was created by forming a loop in the cable and attaching a 4.7 pF ceramic-chip capacitor (ATC, model 4R7C) to the shield of the cable across the loop.

11.1T Coil Development

Following the first study, as described in Chapter 3, it was decided to move all MR imaging to the 11.1T magnet system for the remainder of the *in vivo* experiments (see Chapter 4). This would allow for greater signal-to-noise, resulting in a much higher resolution image, showing greater detail of injury pathology. Two MR coils were used in the measurements of MR images. A circularly polarized, transmit-only “birdcage” coil was used for excitation of resonance and was provided by the Advanced Magnetic Resonance Imaging and Spectroscopy Facility of the McKnight Brain Institute (see “Coil Setup” for description). Then, the resonance signal was measured with a smaller receive-only, circular-polarized coil placed very near the spine. This coil was constructed by Christy Amwake. The receive-only coil was passively decoupled from the transmit coil

during excitation and the transmit-only coil was actively decoupled from the receive-only coil during signal measurement.

The receive-only circularly polarized MR surface coil was constructed specifically for imaging the rat spinal cord at 470 MHz. The coil consisted of two rectangular inductive elements (3 x 3 cm) placed next to each other (with a common side) on the outside of a half-cylinder cradle 4.7 cm in outside-diameter and 77 cm long. Each rectangular section was constructed using copper tape (5 mm in width), with the outer inductor-corner copper tape angled at 45 degrees to the sides. Four 4.7 pF non-magnetic ceramic-chip capacitors (American Technical Ceramics (ATC), model ATC100B-4R7F-WN-1000XC) were inserted in series with the copper tape around the outside of these inductors. These capacitors were inserted in the middle of each arc (at the ends of each rectangular section, opposite the input circuit), and in the middle of the outer side of each rectangular section, in order to provide distributed capacitance around the coil. The common copper-tape element, joining the two inductors, was constructed with a variable non-magnetic capacitor (1-16 pF, Voltronics, Denville, NJ) and inserted in series in the middle of the element. This variable capacitor was used to cancel the mutual inductance between the two inductive sections. The coil formed by the two rectangular sections had an arc of 170 degrees with an overall arc length of 8 cm. Each inductor was passively decoupled from the MR transmitter coil during excitation of the signal. This was accomplished by adding a hand-wound inductor and double-headed non-magnetic diodes (M/A-COM, Lowell, MA, model MA45471) in parallel with 4.7 pF capacitor located in the middle of each inductor arc. The hand-wound inductor was a 2 mm inner diameter solenoid of 2.5 turns made from 20 AWG magnet wire. Each MR coil inductor was

individually tuned and matched with two variable series and one parallel non-magnetic capacitor (1-16 pF, Voltronics, Denville, NJ) arranged on a custom circuit board. Each tune and match circuit was interfaced to the receiver with a 50 ohm coaxial cable containing a parallel-resonance trap on the coaxial shield to eliminate surface currents. The trap was created by forming a loop in the co-axial cable, approximately 2 cm in diameter, and attaching two parallel 4.3 pF non-magnetic ceramic-chip capacitor (ATC, model ATC100B-4R3B-WN-1000XC) to the shield of the cable across the loop. This configuration of coil outputs provided two points along one side of the coil arc, separated by approximately 90 degree, for interface to the receiver to provide detection of the circular polarized signal. This was accomplished by combining the two detected signals, within a 90-degree splitter-combiner (Anaren Corp, East Syracuse, NY, model 10013-3), to provide a single input to the receiver.

Coil Setup

Separate transmit and receive coils were used to increase the SNR and achieve greater depth penetration. A volume coil used for transmission allowed for the development of 90 degree tip angles over a large region of the sample, eliminating the fast changing tip angle variation with depths that occurs with surface coil excitation. On the other hand, the surface coil provides greater sensitivity than the volume coil because of its smaller size.

In setting up the coils, it is important to avoid mutual coupling between the transmit-only volume coil and the receive-only surface coil or signal loss and mismatch will occur. Specifically, it is critical that the surface coil be decoupled during transmission and the birdcage be decoupled during reception. The transmit-only birdcage on the 11.1T is an eight leg, shielded, low-pass birdcage of 8.8 cm diameter and length.

It is turned off during reception by switching high impedance circuits into every leg of the coil. This effectively blocks current from flowing in the coil. The high impedance circuit is a series combination of an inductor and diode placed in parallel with a capacitor on the leg. The inductor and capacitor have equal reactance and creates high impedance when the diode is forward biased (parallel resonance). Conversely, during transmission, the diode is reverse biased removing the high impedance circuit from the leg and the birdcage is fully functional. The diode biasing is controlled by a pulsed signal from the spectrometer.

11.1T Revised Imaging Protocol

After switching to the 11.1T magnet, it was evident that the increase in field strength resulted in an increased sensitivity to breathing artifacts. For this reason, the imaging protocol originally used on the 4.7T magnet had to be modified accordingly for use on the 11.1T magnet system. The modifications made for the 11.1T imaging protocol are described in detail in Chapter 4. Most notably, the read direction was changed to head-foot (sagittal MR images) or left-right orientation (transverse MR images) to eliminate aliasing, and a slice saturation pulse was added to the sequence of high resolution images to eliminate breathing artifacts.

4.7T versus 11.1T Images

One of the most notable advantages in moving from the 4.7T magnet to the 11.1T magnet was the increase in SNR (see Fig. 2-1), and the lack of aliasing due to changes made in the protocol used for the 11.1T. The images collected on the 11.1T magnet had a much higher resolution and showed greater detail of injury pathology after excitotoxic spinal cord injury. In addition, there was an increase in gray-white matter contrast in T1-weighted transverse images collected on the 11.1T magnet.

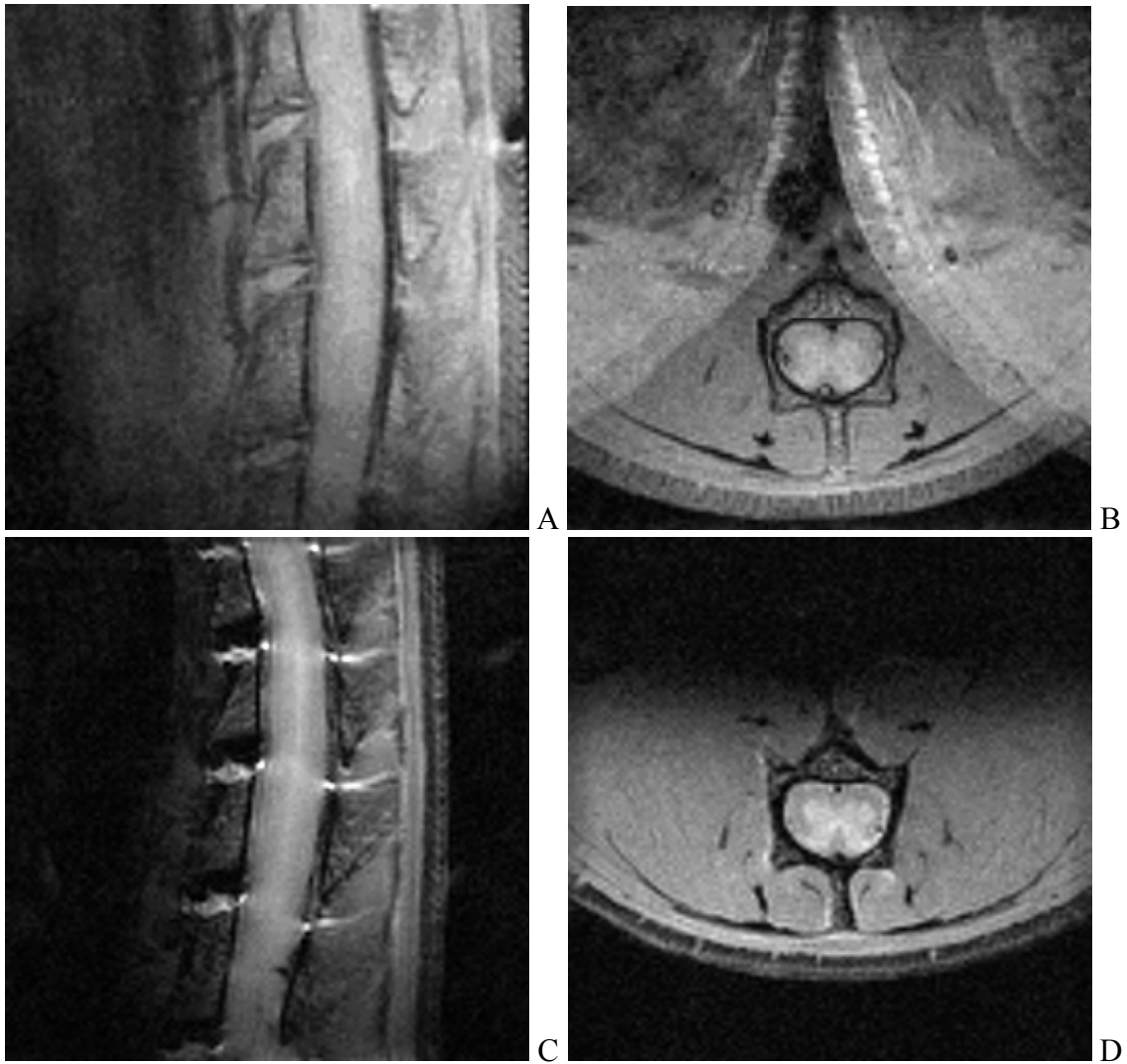


Figure 2-1. Comparison of MR images collected on the 4.7T magnet versus the 11.1T magnet. T1-weighted sagittal (A and C) and transverse (B and D) MR images collected *in vivo* pre-injury (Day 0) on the 4.7T magnet (A, B) or the 11.1T magnet (C, D).

Magnetic Resonance Imaging Obstacles

Heating Effects of the 11.1T Imaging Protocol

After moving to the 11.1T and optimizing the imaging protocol, there was a problem in animal survival during the MRI's. At first, it was thought that the animals were becoming too deeply anesthetized and an anesthetic scavenger line was needed in the magnet to remove excess anesthesia. In addition, the cradle apparatus was lowered to

ensure the animals had ample room to breath. A deltapase isothermal pad (Braintree Scientific, Inc., Braintree, MA) was also placed on the animal during the MRI acquisition. In thinking that the problem had been solved, experiments proceeded, however, the issue of animal survival persisted, and experiments were postponed until the problem could be solved. At this point, it was thought that temperature might be an issue, as animals were coming out of the magnet following imaging sessions much warmer than expected. Temperature measurements were performed on both the 4.7T and 11.1T magnets using a tissue equivalent phantom simulating a rat abdomen (64.1% water, 32.0% sucrose, 1.6% salt, 2.3% TX-151; Beck et al., 2004), and compared. The data revealed that the new sequences that were devised for the 11.1T magnet (described in Chapter 4), which were identical to the 4.7T (described in Chapter 3) except they included slice saturation pulses to eliminate breathing artifacts (the 11.1T is much more sensitive to breathing), were causing extensive heating of the coils and ultimately overheating the animals by several degrees (see Figs. 2-2A, #5; 2-2B, # 1-6). The transverse images versus the sagittal images were causing a significant rise in temperature, which was due to the increase in duty cycle, not magnet frequency. A temperature and respiration monitoring system was then acquired for the 11.1T, which allowed for close monitoring of respiration and temperature, as well as a feedback loop for consistent temperature control. Transverse images in the dynamic contrast-enhanced MRI protocol were also eliminated from the sequence. The final imaging protocol for the 11.1T magnet included the first five pulse sequences shown in Figure 2-2B (described in Chapter 4). During this time, a total of 8 animals were lost due to overheating.

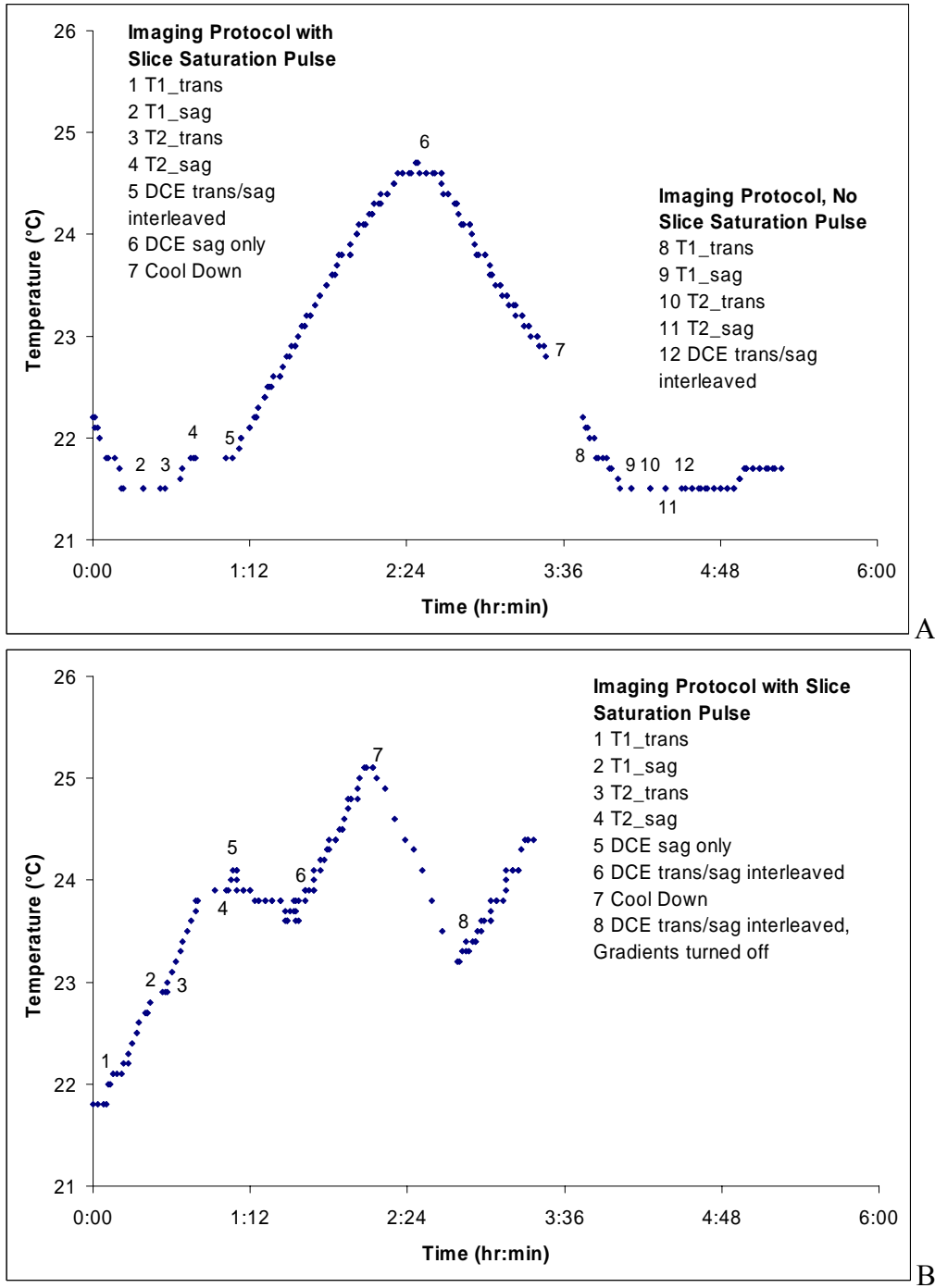


Figure 2-2. Temperature measurements collected on the 4.7T and 11.1T magnets using a tissue equivalent phantom simulating rat abdomen. The measurements were taken using (A) the protocol originally devised on the 4.7T (no slice saturation); and (B) the new protocol devised for the 11.1T (including slice saturation). The new protocol (included slice saturation) resulted in a heating of the phantom on both magnet systems, which did not occur using the old protocol (no slice saturation), thus confirming that the heating was a result of the increase in duty cycle, and not the increase in frequency.

Signal-to-Noise Ratio

The setup used for all *in vivo* imaging protocols is quite extensive and includes many components where problems can arise, including two coils, cables, and an abundance of hardware and software. One of the biggest issues, in addition to animal survival, was SNR problems. On numerous occasions, an imaging session would begin with problem solving due to low or lack of signal. When this occurred, the coils were inspected, all cables were checked to make sure they were not loose or faulty, correct cable connections were confirmed, and the decoupling box was tested to make sure it was functioning. Throughout the course of this project, several cables had gone bad, a fuse was replaced in the decoupling box, diodes were replaced in the volume coil, and capacitors were re-soldered on the surface coil. Occasionally, the problem was more severe and involved magnet hardware, such as the RF amplifiers or gradient power supplies, in which case new parts had to be ordered and as a result, the magnet became inoperable. As a result of poor signal, due to any combination of the above problems, the images had a low SNR when compared to images collected on days of optimal signal (see Fig. 2-3).

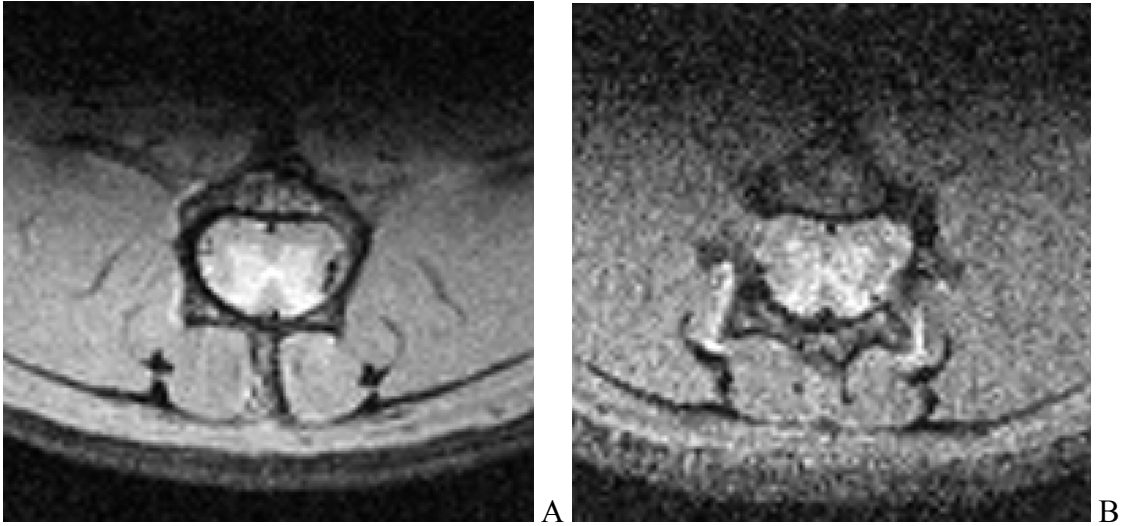


Figure 2-3. Comparison of images collected with high versus low SNR on the 11.1T magnet. (A) T1-weighted (TR/TE = 1000 ms/15 ms, NA = 4) transverse MR image with high SNR. (B) T1-weighted (TR/TE = 1000 ms/15 ms, NA = 4) transverse MR image with low SNR.

CHAPTER 3
EVALUATION OF THE PATHOLOGICAL CHARACTERISTICS OF SPINAL CORD
INJURY WITH MAGNETIC RESONANCE IMAGING*

Introduction

The intraspinal injection of the alpha-amino-3-hydroxy-5-methyl-4-isoxazole-propionate/metabotropic receptor agonist, quisqualic acid, produces an excitotoxic spinal cord injury SCI, which has been used to study the molecular, pathophysiologic, and behavioral characteristics of SCI (Yeziarski, 2002). These injections result in pathologic changes similar to those associated with ischemic and traumatic SCI (Yeziarski et al., 1993; Yeziarski et al., 1998). Although most of what is known about the pathologic changes associated with experimental SCI (ie, edema, neuronal loss, hemorrhage, and cavitation) has come from histologic studies, noninvasive high-resolution MR imaging is becoming a preferred method for the visualization of SCI (Falconer et al, 1994; Ohta et al., 1999; Bilgen et al., 2000). In recent years, MR imaging has become a valuable diagnostic tool in studies examining the pathologic changes following SCI (Flanders et al., 1990; Yamashita et al., 1990; Yamashita et al., 1991; Ohshio et al., 1993; Flanders et al., 1999; Selden et al., 1999; Rattliff and Voorhies, 2000; Ishida and Tominaga, 2002). One well-documented change associated with SCI is the breakdown of the blood–spinal cord barrier. The pathologic characteristics associated with BSCB disruption following SCI can be measured quantitatively with dynamic

* Reprinted with permission from Berens SA, Colvin DC, Yu CG, Yeziarski RP, Mareci TH. Evaluation of the Pathological Characteristics of Spinal Cord Injury with MR Imaging. *AJNR Am J Neuroradiol* 2005; 26(7):1612-1622. © by American Society of Neuroradiology

contrast-enhanced MR imaging, by using exogenous paramagnetic contrast agents (Runge et al., 1997; Bilgen et al., 2001; Bilgen and Narayana, 2001; Bilgen et al., 2002). Fine details of SCI pathology can also be determined with intact excised cords by using MR microscopy. With this technique, motion artifacts are eliminated, allowing the signal intensity-to-noise ratio to be optimized with prolonged scan times and higher field strengths (Guilfoyle et al., 2003).

Thus far, the pathologic characteristics determined with *in vivo* MR imaging have not been compared with *in vitro* MR imaging and histologic examination by using the excitotoxic injury model. We hypothesize that *in vivo* MR imaging has the sensitivity to detect significant differences in pathologic characteristics between two different strategies of injury, which can be correlated with *in vitro* MR imaging and histology. A preliminary description of this study has been reported (Berens et al., 2003).

Materials and Methods

All experiments were carried out in accordance with National Institutes of Health guidelines for the care and use of animals and approved by the University of Florida Institutional Animal Care and Use Committee. *In vivo* and *in vitro* MR methods, along with histologic techniques, were used, because these were the most direct measures of pathologic changes following injury. A comparison of findings with different methods was carried out.

Animal Preparation

The technique of intraspinal injection was similar to that described elsewhere (Yeziarski et al., 1998). In brief, Sprague-Dawley male rats weighing 250–300 g were anesthetized with a mixture of ketamine (3.0 mL), acepromazine (1.0 mL), and xylazine (3.0 mL; mixture at 0.65 mL/kg, subcutaneously). Supplemental doses of anesthetic were

given, if necessary, when rats responded to a noxious pinch applied to the glabrous skin of an extended hind paw. Animals were placed in a stereotaxic frame and the vertebral column immobilized with a vertebral clamp. One injection window for intraspinal injections was made by laminectomy between spinal segments T12–L2. Once the cord was exposed, the dura was incised longitudinally and reflected bilaterally.

A small hole for unilateral injections was made in the pia mater. After injection, muscles were closed in layers and the skin was closed with wound clips. The day following the final *in vivo* image acquisition, animals were anesthetized with sodium pentobarbital and euthanized by transcardial perfusion with normal saline followed by 10% formalin. Spinal cords were removed and stored in 10% formalin.

Intraspinal Injection Procedure

Before injection, QUIS, 125 mmol/L, was mixed in sterile saline, corrected to physiologic pH, and was then injected unilaterally at one level of the cord (T12–L2). To compare injury pathology between lesions at different depths, two types of injection strategies were used: injections at a depth of 500 μm (QUIS lesion 1 [QL1], two animals) and at a depth of 1000 μm (QUIS lesion 2 [QL2], five animals) below the surface (Yeziarski, 2001). Injections were made between the dorsal root entry zone and the dorsal vein on the right or left side, depending on vascularity on the surface of the cord. The total volume of QUIS injected was 1.2 μL in three tracks (0.4 μL /track; distance between tracks 0.5 mm in the rostrocaudal direction). A Hamilton microliter syringe with a glass micropipette extension (tip diameter, 5–10 μm) was used for intraspinal injections. The syringe was positioned in a microinjector unit (Kopf 5000; Kopf, Tujunga, CA) attached to a micromanipulator. A sham injury group was prepared by injecting saline in the same manner as described above.

***In Vivo* MR Imaging**

On the basis of previous correlations between the extent of pathology and the temporal onset of injury-induced behavioral changes, *in vivo* MR imaging was performed 17–24 days (mean, 22 days) after injury (Gorman et al., 2001; Yu et al., 2003). Animals were initially anesthetized by inhalation of a mixture of 5% isoflurane with oxygen at a flow rate of 2 L/min and maintained via a nose cone with a mixture of 2% isoflurane with oxygen at a flow rate of 1 L/min. To determine whether there was disruption of the BSCB following injury, DCE-MR imaging was performed with the intravenous injection of gadolinium-diethylene-triamine-pentaacetic, bis-methylamine ([Gd] Omniscan, Nycomed, Oslo). For intravenous delivery of Gd, the tail vein was cannulated with a 24-G, .75-inch intravenous catheter (Terumo Surflo, Webster Veterinary Supply, Inc., Sterling, MA). Before catheterization, the catheter was filled with heparin solution (mixture of 6 mL of saline and 0.2 mL of 1000 U/mL) to prevent clotting. Once the catheter was in place, a syringe filled with the appropriate volume (0.6 mL/kg body weight) of Gd (0.3 mmol/kg) was attached to the catheter and stabilized with surgical tape. A pulse oximeter was used on the tail to monitor heart rate and blood oxygenation saturation. Core body temperature was monitored during experiments by using a rectal probe and was kept between 35°C and 37°C. Respiration rate was also monitored during data acquisition.

***In Vivo* High Resolution MR Imaging Data Acquisition**

All *in vivo* NMR measurements were performed on a 4.7T, 33-cm-bore Oxford magnet (Oxford Instruments, Oxford, UK) at 200 MHz by using a Bruker BIOSPEC Avance DBX console (Bruker NMR Instruments, Billerica, MA) and 100 mT/m actively shielded gradients. A highly sensitive quadrature MR surface coil was constructed

specifically for imaging the rat spinal cord. The coil consisted of two rectangular overlapping coil elements (3 x 3 cm), constructed by using copper tape, placed on the inside of a half-cylinder cradle 4 cm in diameter. All data acquisition was performed with Bruker ParaVision software. General image processing and analysis of the time series DCE data were performed by using custom software written in the Interactive Data Language (Research Systems, Boulder, CO).

Rats were placed supine in a custom-built half cylinder cradle/coil apparatus. The 200-MHz quadrature MR surface coil was tuned with a Hewlett Packard HP8752C network analyzer (Hewlett Packard, Englewood, CO). The position of the animal was confirmed with pilot images to locate the injury site. Pilot images were T1 weighted (TR/TE = 500 ms/5 ms; NA = 1), with a field of view (FOV) of 6 cm in each direction, a 1 mm section, and a 128 x 128 matrix. Fat suppression was done by using a CHESS-type sequence (Haase et al., 1985). Once the position was confirmed, a set of fat-suppressed, high-resolution sagittal and transverse images was collected. Sagittal T1-weighted (TR/TE = 1000 ms/10.5 ms; NA = 4) spin-echo images were acquired over five sections, each 1 mm thick without a gap between sections. A TR of 1000 ms was chosen to provide optimum signal intensity strength with T1-weighting for anatomic definition. Additional acquisition parameters were a FOV of 4 cm x 2 cm, read out in the head-to-foot direction, and a matrix of 256 x 128. The scan time with these parameters was 8.67 minutes. Transverse T1-weighted (TR/TE = 1000 ms/10.5 ms; NA = 4) spin-echo images were acquired over 14 sections, each 1 mm thick without a gap between sections. Other acquisition parameters were a FOV of 2 cm x 2 cm, read out in the anteroposterior direction, and a matrix of 128 x 128. The scan time was 8.67 minutes.

Sagittal T2-weighted (TR/effective TE = 2000 ms/62.5 ms; NA = 6) fast spin-echo images with phase-encode segmentation were acquired over five sections, each 1 mm thick without a gap between sections. Additional acquisition parameters were a FOV of 4 cm x 2 cm, read out in the head-to-foot direction, phase-encode segmentation factor of 4, and a matrix of 256 x 128. The scan time with these parameters was 6.5 minutes.

Transverse T2-weighted (TR/effective TE = 2000 ms/62.5 ms, NA = 6) fast spin-echo images with phase-encode segmentation were acquired over 14 sections, each 1 mm thick without a gap between sections. Other acquisition parameters were a FOV of 2 cm x 2 cm, read out in the anteroposterior direction, phase-encode segmentation factor of 4, and a matrix of 128 x 128. The scan time with these parameters was 6.5 minutes.

***In Vivo* DCE-MR Imaging Data Acquisition**

After four sets of high-resolution images were collected, a series of dynamic contrast-enhanced images of the rat spinal cord was acquired. Transverse and sagittal images were acquired before and after the contrast agent was injected. Transverse images were acquired with a FOV of 2 cm x 2 cm and a matrix of 64 x 64, over eight sections, and sagittal images with a FOV of 4 cm x 2 cm and a matrix of 128 x 64, over three sections, both 1 mm thick without a gap between sections. Three sets (transverse and sagittal interleaved) of T1-weighted pre-contrast multi-section images (TR/TE = 330 ms/9.4 ms; NA = 8) were collected. After acquisition of the pre-contrast images, Gd was injected in approximately 5 seconds with continuous pressure, to prevent backflow, through the implanted catheter while the animal was in the magnet. Immediately after injection, 8–10 sets (6 minutes for each set) of T1-weighted post-contrast multi-section images (TR/TE = 330 ms/9.4 ms; NA = 8) were collected, with transverse and sagittal data-set acquisitions interleaved. We collected these images over a 60-minute time

frame, which was chosen on the basis of previous experience, with a peak enhancement for the cord at 3 minutes. The receiver gain was adjusted to one-third the value used for the high-resolution images because Gd provides approximately three times the contrast enhancement.

***In Vitro* MR Microscopy**

All *in vitro* NMR measurements were performed on a 14.1T, 51-mm-bore Oxford magnet, at 600 MHz, by using a Bruker BIOSPEC Avance DBX console. All data acquisition was performed with Bruker ParaVision software. Before imaging, spinal cords were placed in phosphate-buffered saline (PBS) overnight. The cords were placed in 5-mm tubes and imaged in PBS by using a standard 5-mm MR coil. Three sets of high-resolution multislice two-dimensional images oriented in three orthogonal directions were collected (TR/TE = 2500 ms/20 ms; NA = 8). The transverse images were acquired over 60 sections (200 μ m thick without a gap between sections; FOV = 5 mm x 5 mm; matrix = 256 x 256), the sagittal images were acquired over 20 sections (200 μ m thick without a gap between sections; FOV = 20 mm x 5 mm; matrix = 1024 x 256), and the coronal images were acquired over 20 sections (200 μ m thick without a gap between sections; FOV = 20 mm x 5 mm; matrix = 1024 x 256). Immediately after the final imaging session, spinal cords were placed in fixative. General image processing and analysis was performed by using custom software written in the Interactive Data Language (IDL, from Research Systems, Boulder, CO).

Histological Procedures

Once imaging was completed, spinal cords were placed in 10% sucrose overnight. Serial sections (75 μ m) were cut on a freezing microtome, collected in PBS, and mounted on gelatin-coated slides. Sections were stained with cresyl violet and cover-slipped. To

confirm that the hypointense signals from MR images correlated with hemorrhage, sections sampled from the injury site were stained with the Prussian-blue reaction (Bancroft and Cook, 1984).

Data Analysis

To compare results obtained with the three different methods used, total longitudinal injury lengths were determined. Statistical analysis of these data included a repeated-measures ANOVA test to determine differences in distances determined by the three methods (SPSS, Chicago, IL). This was followed by a paired comparison to interpret the significance of the ANOVA. To determine the total longitudinal injury length, the total number of transverse sections from each method, with evidence of excitotoxic (ie, cavity formation, hemorrhage, and neuronal loss) damage (Yeziarski et al., 1998; Gorman et al., 2001; Plunkett et al., 2001), were counted and multiplied by the section thickness appropriate for the method used. Transverse images were used for injury length calculation instead of sagittal images, because the boundaries of the injury (eg, neuronal loss in the dorsal horn—a classical characteristic of excitotoxic SCI) were best observed in transverse images. For the calculation of injury length by using *in vivo* MR imaging, T2-weighted transverse images were counted and multiplied by 1 mm; for *in vitro* MR imaging, transverse images were counted and multiplied by 200 μm ; and for histology, sections were counted and multiplied by 75 μm (Gorman et al., 2001). Histologic determination of injury length was done via microscopic examination with 4x and 10x objectives. In addition to injury length, pathologic characteristics (ie, cavity formation, central canal expansion, hemorrhage, and neuronal loss) of the injury were compared between the two types of injection strategies used (ie, QL1 vs QL2).

Injury lengths were also compared between QL1 and QL2. Statistical analysis of these data included a one-way between subjects ANOVA test to determine differences in injury severity between the four injury/treatment groups (SPSS, Chicago, IL). This was followed by a Tukey HSD post hoc test to interpret the significance of the ANOVA.

For DCE-MR imaging processing, regions of interest (region of interest) were selected in the injured and normal cord, muscle, and bone. A 1 mm x 2 mm elliptical region of interest was drawn in regions of injury and normal cord because the enhanced region was typically elliptical. A 1 mm circle region of interest was drawn for muscle and bone and was analyzed to determine the success of the Gd injection. Ten percent peak enhancement was used as the cutoff value because regions of interest of normal cord showed 10% peak enhancement because of the presence of contrast agent in the cord vasculature.

Results

In Vivo High Resolution MR Imaging

Figure 3-1 shows a comparison of the pathologic findings from the same animal (S05) at the same location for all three methods used in this study. The appearance of images was compared with normal controls. When an image region relative to a control region appeared darker, we classified it as hypointense. When an image region relative to a control region appeared brighter, we classified it as hyperintense. No signal intensity changes were observed in the normal cord on either T1-weighted or T2-weighted images (data not shown). The only significant information obtained from T1-weighted images of QUIS-injured animals was the injection tracks, which were seen as weak hypointense (ie, dark) signals.

Figures 3-2A and 3-3A show the sagittal and transverse T2-weighted *in vivo* images, respectively, for each injured animal. Using *in vivo* transverse images, it was possible to determine the anatomic level of the sections by examining the size and shape of the cord as well as gray and white matter. Injection tracts for QUIS injections were visible in both T2-weighted (Figs 3-1 and 3-3) and T1-weighted transverse images (not shown) in all animals. Hypointense signals can be seen within the cord on T2-weighted images of all QUIS-injured animals; however only T2-weighted *in vivo* images of QL2 animals (S01, S02, and S04–S06) showed hyperintense (ie, bright) signals.

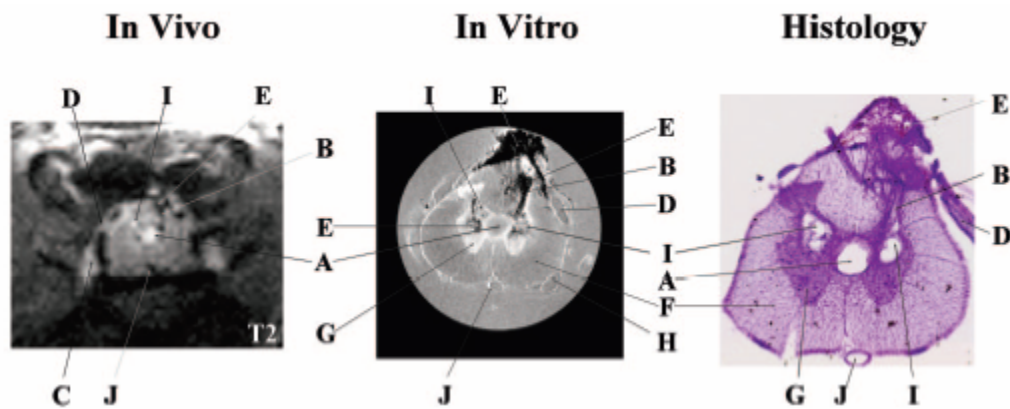


Figure 3-1. Representative pathologic findings in the same animal (S05) at the same location observed *in vivo* (T2-weighted, TR/effective TE = 2000 ms/62.5 ms; NA = 6), *in vitro* (TR/TE = 2500 ms/20 ms; NA = 8), and in histologic sections. Many of the same pathologic details are visible with all three methods albeit with different levels of resolution. *In vivo* and *in vitro* images are displayed with image size = 0.92 cm x 0.77 cm (*in vivo*) and 0.50 cm x 0.50 cm (*in vitro*). Letters label the most distinctive anatomic and pathologic characteristics observed in the three images as follows: A indicates expanded central canal; B, injection track; C, dorsal root ganglion; D, dorsal root; E, hemorrhage at injury site; F, white matter; G, gray matter; H, ventral root; I, cavity; J, anterior spinal vessel. *In vivo* images show cavitation as hyperintense signals due to T2 weighting, whereas, on *in vitro* images, cavities appear isointense in these proton attenuation-weighted images.

In vivo images showed consistent differences between QL1 and QL2 animals (Figs 3-4 to 3-6). It is important to note that hyperintense signals, indicating expansion of the

central canal and cavitation, were not seen in images from QL1 animals (Fig 3-3A, X01 and X03; Fig 3-6). Although the only difference in QUIS injection parameters was depth of injection, there were dramatic differences in the extent of pathologic damage (e.g., laterality, cavitation, and expansion of the central canal). There were also significant differences ($p < 0.001$, one-way between subjects ANOVA, $F = 34.134$, $p < 0.001$) in injury lengths between QL1 (X01 and X03) and QL2 animals (S01, S02, and S04–S06; Fig 3-4).

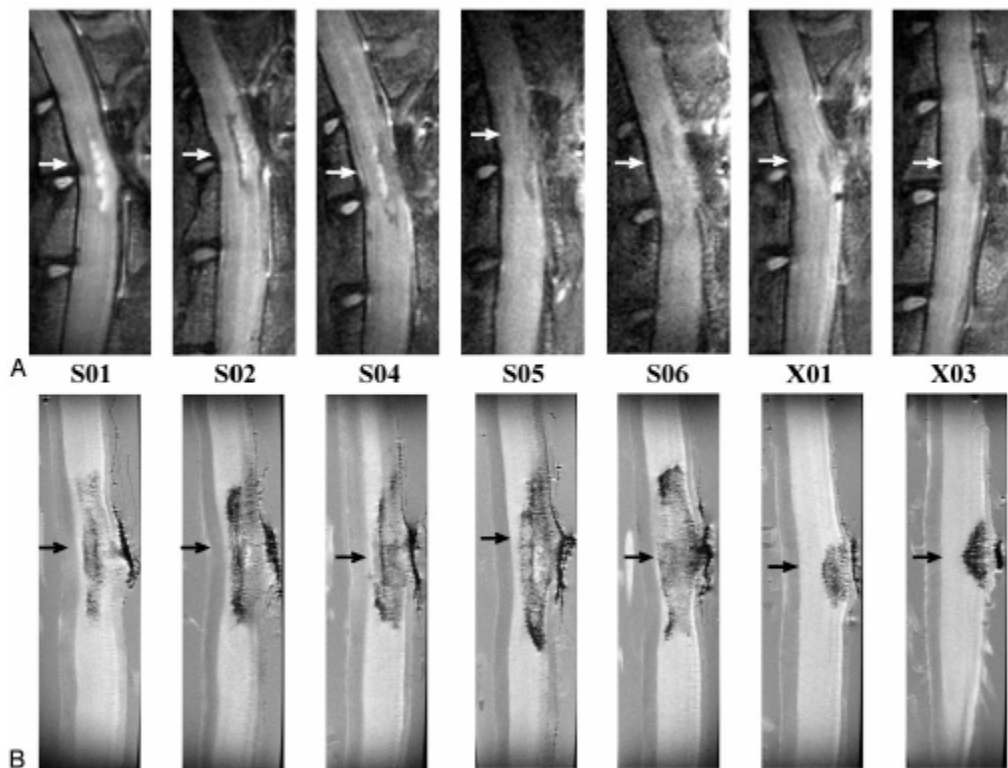


Figure 3-2. Sagittal images for all QUIS-injured animals. (A) *In vivo* (T2-weighted, TR/effective TE = 2000 ms/62.5 ms; NA = 6); and (B) *in vitro* (TR/TE = 2500 ms/20 ms; NA = 8). Images are oriented with rostral at the top and dorsal on the right. Arrows represent the location of the epicenter of the injury. The epicenter was defined as the region of maximal pathologic damage. Displayed image size = 0.77 cm x 2.15 cm (*in vivo*) and 0.40 cm x 1.50 cm (*in vitro*). Animals designated S01, S02, S04, S05, and S06 received QL2, whereas animals designated X01 and X03 received QL1. The vertebral column and laminectomy site were easily observed in both *in vivo* and *in vitro* sagittal images.

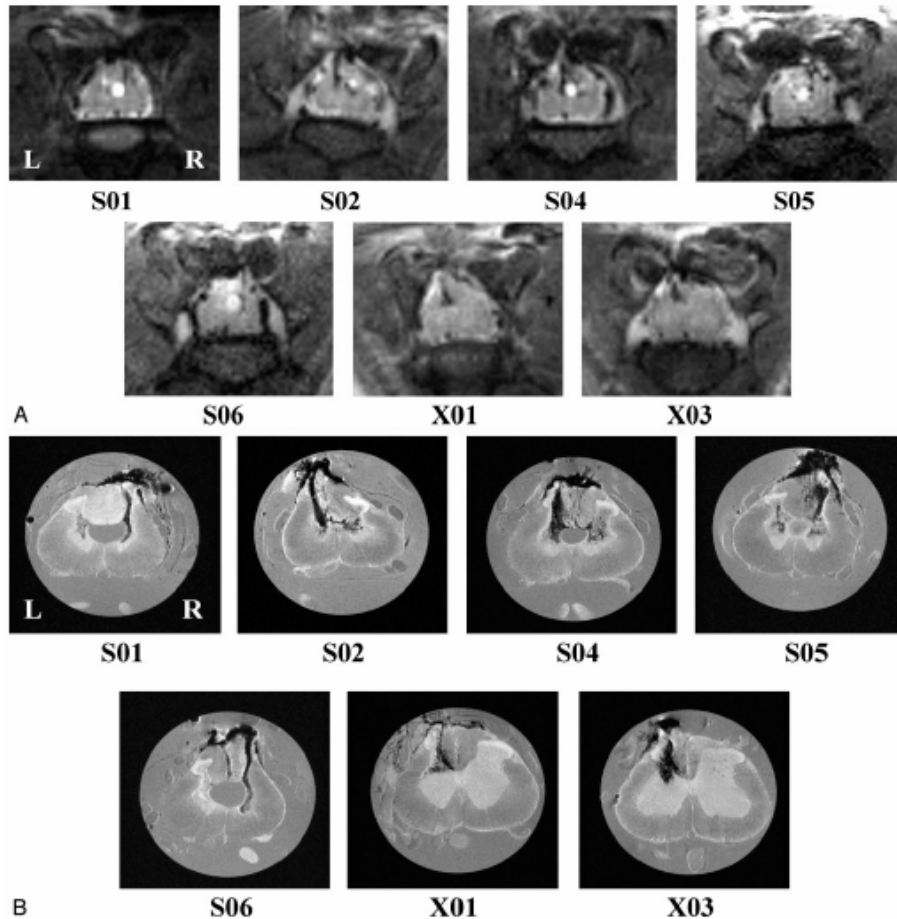


Figure 3-3. Transverse images for all QUIS-injured animals. (A) *In vivo* (T2-weighted, TR/effective TE = 2000 ms/62.5 ms; NA = 6); and, (B) *in vitro* (TR/TE = 2500 ms/20 ms; NA = 8). Images are sampled from the epicenter of the injury (arrows in Fig 3-2) and show comparable pathologic changes between methods. See Fig 3-1 for labeling of anatomic and pathologic findings. Images are oriented with dorsal at the top. L, left side of cord; R, right side of cord, for all images. Displayed image size = 0.92 cm x 0.77 cm (*in vivo*) and 0.50 cm x 0.50 cm (*in vitro*). A, Hypointense signals correlated with hemorrhage (see “Histologic Findings”) and hyperintense signals correlated with the presence of fluid filled cavities. For example, notice the hyperintense expanded central canal in the cord of animals S01, S02, and S04–S06 and the hyperintense cavity in the gray matter on the right side of the cord in animal S02. B, Hypointense regions were observed bilaterally in the gray matter in all QL2 animals (S01, S02, and S04–S06), whereas, in QL1 animals, evidence of hemorrhage was observed only ipsilateral to the side of QUIS injection (X01 and X03). In addition, hypointense areas were observed in the dorsal columns in all the QUIS-injured animals except S01. Central canal expansion was clearly defined in four of the five QL2 animals (S01 and S04–S06), and injection tracks were visible in all injured animals. Cavity formation was also seen in all QL2 animals bilaterally.

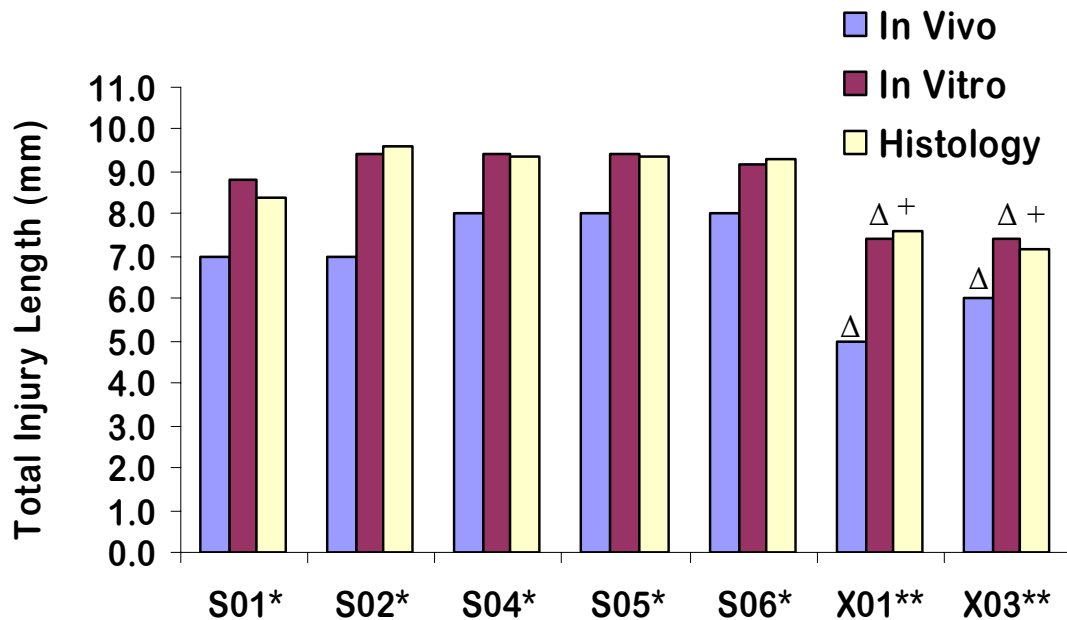


Figure 3-4. Total injury lengths determined by using *in vivo*, *in vitro*, and histologic methods for each QUIS-injured animal. Total injury lengths in millimeters reflect the presence of excitotoxic tissue damage. No significant differences are observed between *in vitro* and histology ($p > 0.05$). Significant differences are observed between *in vivo* and *in vitro*/histology ($p > 0.05$), but these differences are within the range of section thickness difference between *in vivo* and *in vitro* images. A single asterisk denotes the QL2 animals, and double asterisks denote the QL1 animals. Significant differences ($\Delta p < 0.001$, $+p < 0.01$) in injury lengths were found between QL1 and QL2 animals for all three methods.

***In Vivo* DCE-MR Imaging**

To determine whether there was BSCB disruption at the 17–24 day interval (mean = 22 days) post-injury, DCE-MR imaging was performed by using Gd as a contrast agent. Disruption of the BSCB was indicated by a significant Gd enhancement ($>10\%$) within the cord at the site of injury. No significant Gd enhancement was observed in the normal and sham groups and no significant Gd enhancement was observed within the cord at the site of injury in any of the QUIS-injured animals. Gadolinium enhancement,

however, was observed in surrounding muscle of all animals, approximately 300% peak signal intensity enhancement, which indicates that the procedure was performed correctly.

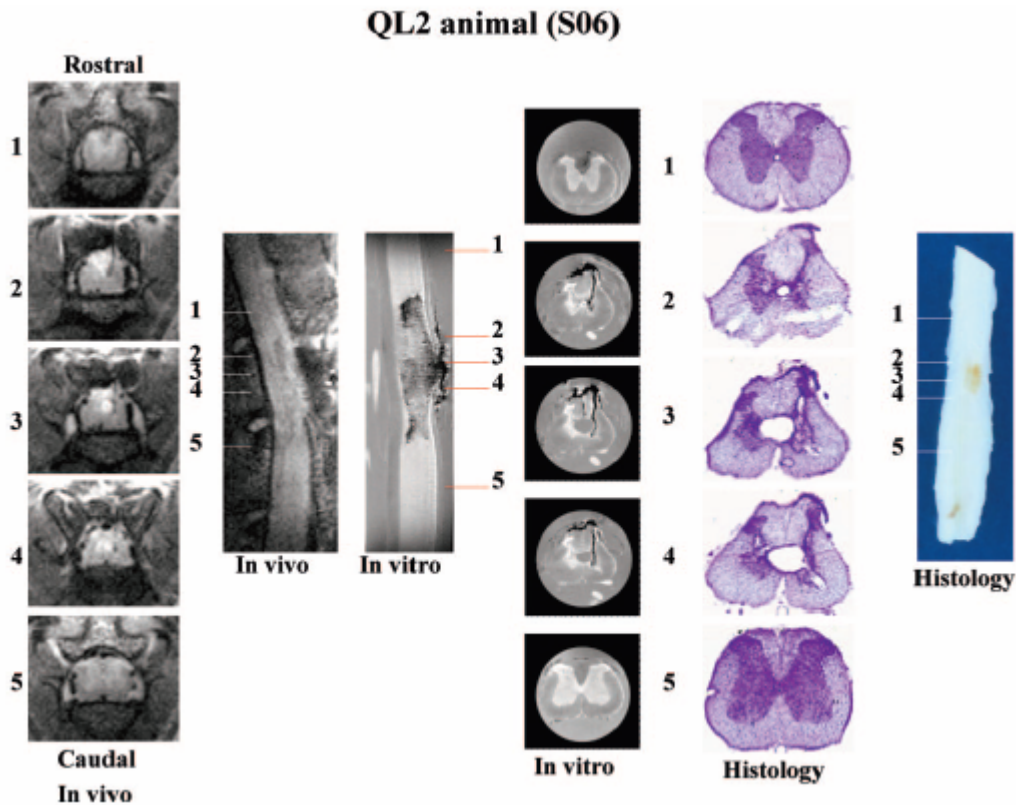


Figure 3-5. Summary of *in vivo*, *in vitro*, and histologic data collected for a representative QL2 animal (S06). Representative sections (1–5) are sampled from the same rostrocaudal location in the spinal cord with each method used. Image sizes are the same as in Figs 3-2 and 3-3. See Fig 3-1, for labeling of anatomic and pathologic findings. Although sagittal images show the rostral-caudal extent of the injury, transverse sections provide greater detail of the pathologic changes associated with this injury model.

***In Vitro* MR Microscopy**

Images obtained *in vitro* had greater resolution and more clearly defined the pathologic characteristics (i.e., neuronal loss, hemorrhage, and cavitation) of the injury compared with the *in vivo* MR images. No abnormal signals were observed in the normal control animal. For the saline-injected animal, however, a hypointense region was

observed at the site of injection, which correlated with hemorrhage (see “Histologic Findings”). Figures 3-2B and 3-3B illustrate the sagittal and transverse *in vitro* images, respectively, at the epicenter for each QUIS-injured animal. In both sagittal and transverse images, white matter and gray matter were clearly distinguishable and the cord level was easily determined. In all QUIS-injured animals, hypointense regions were observed at the site of injury, correlating with hemorrhage.

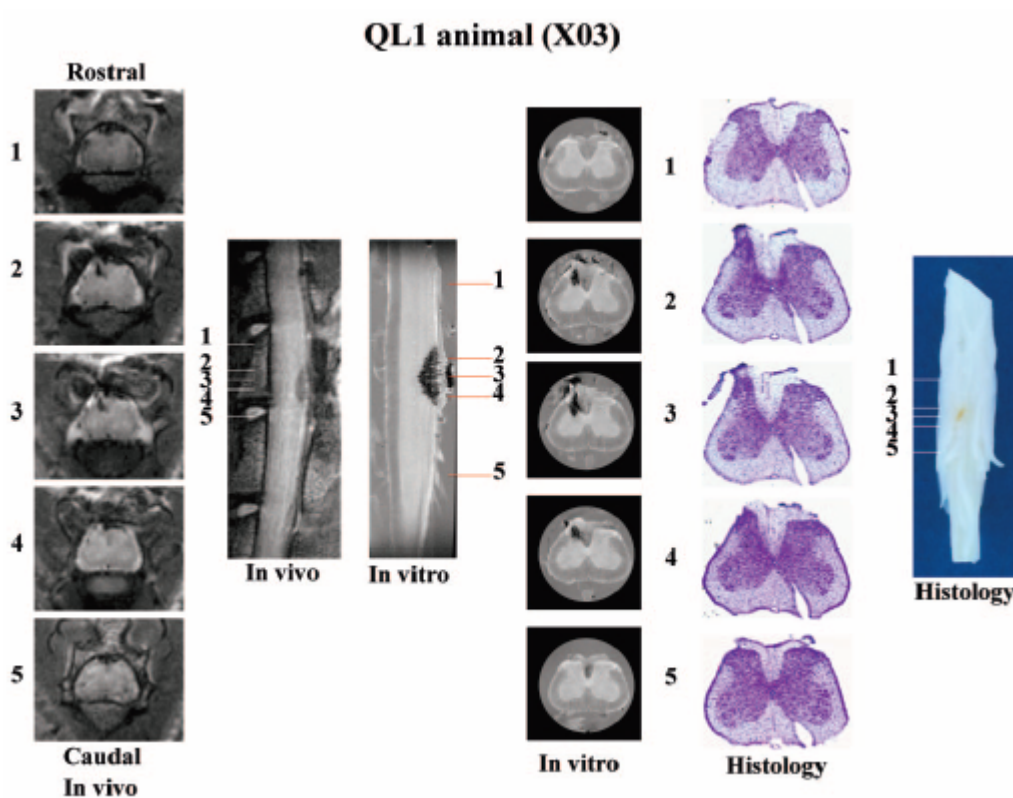


Figure 3-6. Summary of *in vivo*, *in vitro*, and histologic data collected for a representative QL1 animal (X03). Representative sections (1–5) are sampled with each method from the same rostrocaudal location in the spinal cord. Image sizes are the same as in Figs 3-2 and 3-3. See Fig 3-1, for labeling of anatomic and pathologic findings. Although sagittal images show the rostral-caudal extent of the injury, transverse sections provide greater detail of the pathologic changes associated with this injury model.

Total injury lengths measured with *in vitro* MR images were significantly greater than lengths determined with *in vivo* MR images, because of differences in section

thickness (Fig 3-4); repeated-measures ANOVA ($F = 40.476$; $p = 0.001$). Pair-wise comparisons indicated that *in vivo* MR imaging gave significantly shorter injury lengths than *in vitro* MR imaging ($p = 0.001$) and histology ($p = 0.001$), but were within the range of difference in section thickness (length difference standard deviation = 0.50 mm) for each method used (section thickness *in vitro* of 0.2 mm and *in vivo* of 1.0 mm). Additionally, there were significant differences ($p < 0.001$, one-way between subjects ANOVA, $F = 34.134$, $p < 0.001$) in injury lengths between QL1 (X01 and X03) and QL2 animals (S01, S02, and S04–S06; Fig 3-4).

Histologic Findings

Histologic results confirmed the pathologic characteristics observed with *in vivo* and *in vitro* MR imaging. Injection tracts were visible in all QUIS-injured animals, as well as saline-injected animals. Neuronal loss in the dorsal horn ipsilateral to the injury was observed in all QUIS-injured animals. Neuronal loss in the dorsal horn contralateral to the injection site was observed in all QL2 animals but not in QL1 animals. Central canal expansion was observed in four of five QL2 animals and cavity formation was observed only in QL2 animals, being present both ipsilateral and contralateral to the side of QUIS injection. Sections from three of three animals (S01, S06, and X03) stained positive for the Prussian Blue reaction, confirming the presence of hemorrhage at the same location of hypointense signal intensity as observed in the *in vivo* and *in vitro* images.

Because of histologic artifacts, complete injury lengths could not be determined for all cords. In animals with minimal histologic damage (all but X03), however, the total injury lengths determined from histologic evaluation showed no significant differences to those determined with *in vitro* images (Fig 3-4; $p = 0.05$). However, here were

significant differences ($p < 0.01$, one-way between subjects ANOVA, $F = 34.134$, $p < 0.001$) in injury lengths between QL1 (X01 and X03) and QL2 animals (S01, S02, and S04–S06; Fig 3-4).

Figures 3-5 and 3-6 show a summary of data collected from a representative QL2 (S06) and QL1 (X03) animal, respectively. Sufficient detail is visible in the *in vivo* images to determine the type and extent of pathologic damage. There was narrowing of the dorsal horn with sparing of the superficial laminae bilaterally in all QL2 animals. This is in contrast to QL1 animals, in which sparing was observed only unilaterally. A significant observation in this study was that following the more superficial injury (laminae I–III, QL1); damage occurred only ipsilateral to the side of QUIS injections and included only evidence of hemorrhage. In contrast, lesions deeper in the gray matter (QL2) produced damage both ipsilateral and contralateral to the injection site, showing evidence of both hemorrhage and cavitation. In addition, evidence for differences between QL1 and QL2 injuries were seen in the rostrocaudal and ventral extent of injury (e.g., less extensive in QL1 animals compared with QL2 animals [Fig 3-6]).

Discussion

Clinically, MR imaging has been a useful tool for the study of secondary complications associated with SCI. For example, MR imaging can play an important role in the study of post-traumatic syringomyelia. The excitotoxic injury model has been shown to produce pathologic changes similar to those observed in this condition (Yeziarski et al., 1993; Schwartz et al., 1999a). Considering the lack of understanding of the pathologic mechanism responsible for cavity formation in the injured cord (Madsen et al., 1994), it may be possible to gain insight into the mechanism of cavitation by using *in vivo* MR imaging at different time points following excitotoxic SCI. In the past,

clinicians have relied on patient descriptions of behavioral changes in determining clinical outcome (Williams, 1990; Oakes, 1996); however, MR imaging recently has been used to monitor changes associated with intraspinal transplantation, graft-mediated functional recovery, and changes in syrinx morphology after transplantation (Wirth et al., 2002) and to differentiate between cyst and scar or tumor formation with the help of MR contrast agent administration (Schwartz et al., 1999a). With the importance and many uses for MR imaging, continued research is needed to enhance this technique and expand its uses to provide a better understanding of the mechanisms responsible for pathologic changes associated with SCI. For example, an important question related to SCI is the temporal profile of pathologic changes in the acute and chronic stages post-injury. Using *in vivo* MR imaging, it should be possible to monitor these changes in the same animal. In the present study the feasibility of using a complement of *in vivo* and *in vitro* MR imaging, along with histologic methods to study experimental SCI was examined.

The results have shown that MR images provide details of pathologic changes, which correlated with histologic findings, and were easily detected both *in vivo* and *in vitro*. These changes include cavities, central canal expansion, hemorrhage, and tissue loss. These characteristics of injury are similar to those previously reported in both experimental (Weirich et al., 1990; Wirth et al., 1992; Falconer et al., 1994; Wirth et al., 1995; Ohta et al., 1999; Schwartz et al., 1999a; Bilgen et al., 2000; Metz et al., 2000) and clinical studies (Flanders et al., 1990; Weirich et al., 1990; Yamashita et al., 1990; Yamashita et al., 1991; Ohshio et al., 1993; Flanders et al., 1999; Selden et al., 1999; Rattliff and Voorhies, 2000; Ishida and Tominaga, 2002). The present study is one of the

first that has attempted to compare all three methods (see also a recent study in the mouse [Bonny et al., 2004]).

An important finding in this study was the sensitivity of *in vivo* MR imaging to detect differences in pathology between two different strategies of injury. Despite the small differences in injury depths between QL1 and QL2, there were significant differences in the overall pathology detected in the *in vivo* MR images. Following the shallower injury (i.e., QL1), damage was observed only unilaterally in the gray matter and did not show any cavitation or central canal expansion. In contrast, following the deeper injury (i.e., QL2), damage was more severe, and showed cavitation, hemorrhage, and neuronal loss bilaterally. These differences could be due to the connectivity between regions of the cord at different depths in the gray matter. For example, propriospinal connections involving laminae IV–VII are far more extensive within and between segments than those involving more superficial laminae (Yeziarski et al., 1980; Menetrey et al., 1985). Although speculative, it is possible that, once damaged, a signal is relayed to other parts of the gray matter that induces further damage. The deeper lesion (QL2) resulted in damage of the contralateral side of the cord similar in pathologic characteristics to the side that received the QUIS injection. This suggests a similar mechanism of injury (i.e., excitotoxicity). From this, one might conclude that propriospinal connections exert a trophic influence on other parts of the gray matter and once damaged, leads to an injury induced release of excitatory amino acids and subsequent pathologic changes. This observation may be important from the standpoint of providing insight into the mechanism responsible for the progression of pathologic changes following spinal injury.

There was a corresponding loss of gray matter illustrated in *in vitro* MR images and histology. These changes could be quantified with sufficient information about volumes of normal white and gray matter. Volume quantification of white and gray matter loss is important; however, it was beyond the scope of this study and was considered in future studies (Chapter 4).

All three methods used in this study were directly compared, because they all showed similar pathologic changes. For example, *in vitro* MR images were the most precise in determining injury length, rather than histologic sections due to histologic artifacts. Although significant differences were detected between total lengths of injury, these differences were within the thickness of sections of the methods used. For this reason, the present data support the conclusion that *in vivo* MR imaging is a useful technique to study the evolution of pathologic changes following SCI. This feature may be especially important when correlated with the profile of changes related to the disruption of the BSCB.

The observation of changes in the BSCB is important in characterizing the excitotoxic model of SCI, because BSCB disruption can contribute to events leading to detrimental pathologic processes following SCI (Rapoport, 1976; Bradbury, 1979). At the time points used in this study, 17–24 days post-injury, our measurement of the BSCB indicated that the barrier was intact; however, previous studies indicate an opening at earlier time points following contusion injury (Runge et al., 1997; Bilgen et al., 2001). Therefore, longitudinal studies will be necessary to detect the temporal characteristics of how the BSCB is affected following excitotoxic SCI. Preliminary data from a subsequent

study suggest that there are changes over time in the integrity of the BSCB following excitotoxic injury (S. A. Berens, P. Yeziarski, T. H. Mareci; Chapter 4).

There are several advantages and disadvantages associated with each of the methods used in the present study. *In vivo* MR imaging can be used to non-invasively monitor the progression of pathologic changes over time in the same animal. This feature provides the opportunity to study the neuroprotective and neurorestorative properties of therapeutic interventions (e.g., transplants, drugs, etc). *In vivo* MR imaging methods, however, lack the higher resolution that *in vitro* MR imaging and histologic methods provide. Despite the higher resolution, *in vitro* MR imaging and histologic methods have the disadvantage that they cannot be used at different time points in the same animal, and there is a risk of losing tissue in histologic analysis because of processing artifacts. Another advantage of *in vivo* MR imaging is the ability to analyze the injured cord in transverse and sagittal planes of section at different time points in the same animal. This capability allows one to easily determine the overall extent of injury as well as gross pathologic changes, two important characteristics used in the evaluation of therapeutic interventions. With continued technological improvements in *in vivo* MR imaging, this technique will continue to be an important analytical tool in the study of SCI.

In some regions, *in vivo* MR images, collected on a 4.7T magnet, appear different from *in vitro* MR images collected on a 14.1T magnet. The *in vivo* MR images were collected by using T2-weighted fast spin-echo sequences, whereas *in vitro* MR images were collected by using proton density-weighted spin-echo sequences. *In vivo* MR images show cavitation as hyperintense signals due to T2-weighting, which is

comparable to what is used in human MR imaging. This is in contrast with *in vitro* MR images, because cavities appear isointense due to proton attenuation weighting.

A limited number of studies have used *in vivo* MR imaging in experimental animal models, with an even smaller number using *in vitro* MR imaging techniques. In the present study, we have used customized hardware (coils) and high magnetic fields to obtain high-quality *in vivo* and *in vitro* images in the rat. Continued improvement of these MR components should lead to an increased utility of these methods. In our study, *in vivo* MR images show high resolution and greater pathologic detail than reported in previous MR imaging studies at this magnetic field strength or lower (Hackney et al., 1986; Runge et al., 1997; Fraidakis et al., 1998; Ohta et al., 1999; Iannotti et al., 2002; Brodbelt et al., 2003). As expected, higher quality MR images can be obtained at higher magnetic fields (Bonny et al., 2004; Franconi et al., 2000) or with chronically implanted MR coils (Bilgen et al., 2000; Bilgen et al., 2001; Wirth et al., 1993; Ford et al., 1994b; Fenyes and Narayana, 1998; Narayana et al., 1999; Silver et al., 2001). Although we have been involved in the development of implanted coil technology (Wirth et al., 1993; Silver et al., 2001), we did not use implanted coils in this study because we wanted to eliminate the possible confounding effects of coil implantation and also eliminate additional damage to the cord. By comparing the results of *in vitro* and histologic methods, details seen *in vivo* can be confirmed, thus strengthening the rationale for using *in vivo* MR imaging as an important tool in the study of SCI.

CHAPTER 4
USE OF MAGNETIC RESONANCE IMAGING TO STUDY THE
NEUROPROTECTIVE EFFECTS OF AGMATINE FOLLOWING SPINAL CORD
INJURY IN THE RAT

Introduction

The excitotoxic events following a quisqualic acid lesion play an important role in the pathologic sequelae of spinal injury (Regan and Choi, 1994). The use of antagonists of glutamate receptor subtypes has provided evidence for the involvement of excitotoxic cascades in the pathological outcomes of QUIS induced spinal injury (Fairbanks et al., 2000). Studies involving the QUIS model have shown, for example, pathophysiological changes, up-regulation in gene expression for NMDA receptors and inducible nitric oxide synthase (Plunkett et al., 2001). Agmatine (decarboxylated arginine) is an endogenous neurotransmitter/neuromodulator that has been shown to have both NMDA receptor antagonist (Yang and Reis, 1999) and NOS inhibitor properties (Auguet et al., 1995; Galea et al., 1996). The multifaceted capacity of this agent makes it a promising therapeutic agent in targeting secondary injury.

In the present research, the effects of agmatine, an agent with known pharmacological actions, was evaluated in relation to blood-spinal cord-barrier disruption, edema and cavity formation, and blood vessel leakage. It is believed that limiting BSCB disruption reduces the entry of inflammatory mediators into the spinal cord. The BSCB may therefore represent an important target of therapeutic intervention. Applying the use of MRI to monitor the above pathological characteristics longitudinally following administration of a known neuroprotective agent will provide insight into the

site of action and mechanism of a drug with known pharmacological actions as well as further validate the use of MRI in the study of spinal cord injury. A preliminary description of this study has been reported (Berens et al., 2004).

Materials and Methods

Animals, Surgery, and *In Vivo* MR Imaging

Sprague-Dawley male rats weighing 250-300g were subjected to excitotoxic spinal cord injury as described in Chapter 3. Rats received an *in vivo* MRI prior to injury to serve as their own controls, with animal preparation as described in Chapter 3. Following MRI, animals were assigned to one of four injury/treatment groups (see “Neuroprotection” below) and then were injected with QUIS or saline (sham injury) at a depth of 500 μm .

Neuroprotection

Agmatine was purchased from Sigma (St. Louis, MO), and dissolved in 0.9% saline. Animals were separated into 4 injury/treatment groups as follows: (1) Saline-SCI (sham injury, N = 5); (2) QUIS-SCI plus vehicle (0.9% saline, N = 6); (3) QUIS-SCI plus Agmatine I (25 mg/kg, N = 7); and (4) QUIS-SCI plus Agmatine II (80 mg/kg, N = 7). Rats were given treatment intraperitoneally 30 minutes post-QUIS injury and once a day for 14 days (refer to Fig. 4-1 for a summary of the surgery and MR imaging timeline).

***In Vivo* High-Resolution Magnetic Resonance Imaging Data Acquisition**

In vivo MRI and DCE-MRI were performed on days 1, 3, 7, 15, and 25 post-injury (see Fig. 4-1). All *in vivo* NMR measurements were performed on an 11.1 T, 40 cm clear bore Oxford magnet at 470 MHz by using a Bruker BIOSPEC Avance DBX console (Bruker NMR Instruments, Billerica, MA) and 200 mT/m actively shielded gradients. A highly sensitive quadrature MR surface coil was constructed specifically for imaging the

rat spinal cord (please refer to Chapter 2 for coil specifications). Pilot images were T1-weighted (TR/TE = 1000ms/15 ms, NA = 1), with a FOV of 8 cm in each direction, a 1 mm slice, and a 128 x 128 matrix. Fat suppression was done using a CHESS-type sequence (Haase et al., 1985). To compensate for breathing artifacts and eliminate aliasing, the read direction was changed to head-foot (sagittal MR images) or left-right orientation (transverse MR images), and a slice saturation pulse was added to the sequence of high-resolution images. The slice saturation pulse had a sinc (modified sinc) pulse shape and was a single 30 mm thick slice in the coronal direction. Once the position was confirmed, a set of fat suppressed, slice saturated, high-resolution sagittal and transverse images was collected. Sagittal T1-weighted (TR/TE = 1000 ms/15 ms, NA = 4) spin echo images were acquired over 5 slices, each 1 mm thick without a gap between slices. Additional acquisition parameters were a FOV of 2 cm x 2 cm, read out in the head-foot direction, and a matrix of 128 x 128. The scan time with these parameters was 8.58 min. Transverse T1-weighted (TR/TE = 1000 ms/15 ms, NA = 4) spin echo images were acquired over 14 slices, each 1 mm thick without a gap between slices. Other acquisition parameters were a FOV of 2 cm x 2 cm, read out in the left-right direction, and a matrix of 128 x 128. The scan time was 8.58 min.

Sagittal T2-weighted (TR/effective TE = 2000 ms/62.5 ms, NA = 12) fast spin echo images with phase-encode segmentation were acquired over 5 slices, each 1 mm thick without a gap between slices. Additional acquisition parameters were a FOV of 2 cm x 2 cm, read out in the head-foot direction, phase-encode segmentation factor of 4, and a matrix of 128 x 128. The scan time with these parameters was 13.35 min. Transverse T2-weighted (TR/effective TE = 2000 ms/62.5 ms, NA = 12) fast spin echo images with

phase-encode segmentation were acquired over 14 slices, each 1 mm thick without a gap between slices. Other acquisition parameters were a FOV of 2 cm x 2 cm, read out in the anterior-posterior direction, phase-encode segmentation factor of 4, and a matrix of 128 x 128. The scan time with these parameters was 13.35 min.

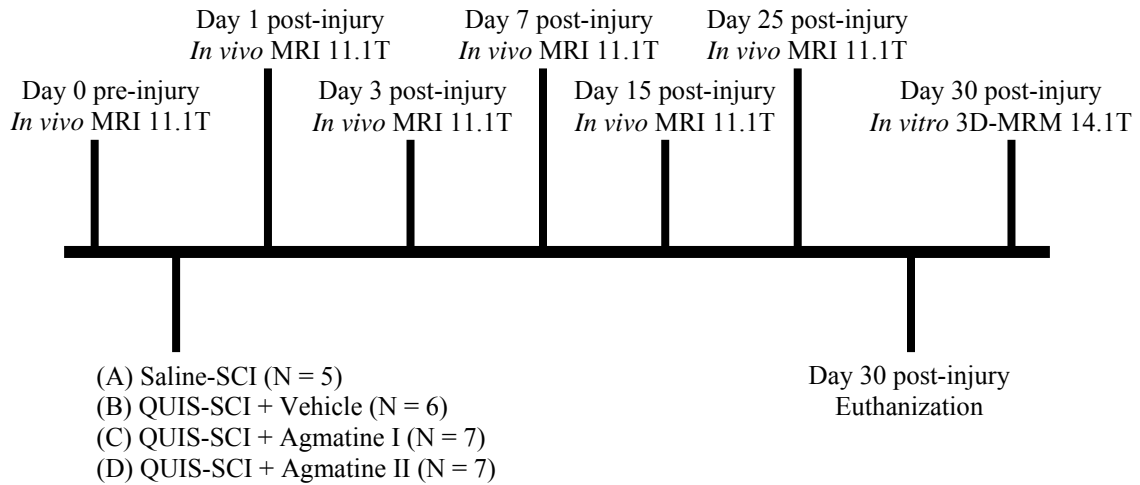


Figure 4-1. Surgery and MR imaging timeline. Each animal was subjected to a pre-injury MRI, and then assigned to one of four injury/treatment groups. Animals then received an *in vivo* MRI on days 1, 3, 7, 15, and 25 post-injury, and were sacrificed on day 30 post-injury. Cords were excised and undergo *in vitro* three dimensional MR microscopy.

***In Vivo* DCE-MR Imaging Data Acquisition**

After 4 sets of high-resolution images were collected, a series of dynamic contrast-enhanced MR images was acquired as described in Chapter 3. Only sagittal images were acquired before and after the contrast agent was injected due to extreme heating effects caused by the transverse DCE-MR image acquisition (as described in Chapter 2). Fat suppressed, slice saturated sagittal images were acquired with a FOV = 2 cm x 2 cm, matrix = 96 x 96, over 3 slices, both with 1 mm thick, without a gap between slices. Three sagittal T1-weighted pre-contrast multi-slice images (with a 3 minute gap between each image) (TR/TE = 330 ms/9.4 ms, NA = 6) were collected. After acquisition of the

pre-contrast images, Gd was injected over a period of approximately 5 seconds with continuous pressure, to prevent backflow, through the implanted catheter while the animal was in the magnet. Immediately after injection, nine sagittal T1-weighted post-contrast multi-slice images (3 minutes between each image) (TR/TE = 330 ms/ 9.4 ms, NA = 6) were collected. These images were collected over a 60 minute timeframe, which was chosen based on previous experience with a peak enhancement for the cord at 3 min. The receiver gain was adjusted to one-third the value used for the high-resolution images because Gd provides approximately 3 times the contrast enhancement.

***In Vitro* Three-Dimensional MR Microscopy**

All excised cords were subjected to *in vitro* three-dimensional MR microscopy, with cord preparation as described in Chapter 3. Images were acquired with a three-dimensional gradient echo pulse sequence using a TR = 150 ms, TE = 10 ms with NA = 2. The image FOV was 2 cm x 0.5 cm x 0.5 cm in a matrix of 512 x 128 x 128 in a total data acquisition time of 1.5 hrs. Therefore, MR images were acquired with an isotropic resolution of 40 microns. A 3D Fourier transformation was applied to the acquired data matrix to produce the 3D image. General image processing and analysis was performed using custom software written in the Interactive Data Language (IDL, from Research Systems, Boulder, CO).

Data Analysis

To compare results obtained between the four injury/treatment groups, the amount of edema, blood vessel leakage, cavitation, and total longitudinal injury lengths were determined and compared. To determine the amount of edema, the total number of MR transverse image slices (please refer to Chapter 3 for justification in using transverse slice orientation), with evidence of edema (diffuse hyperintense signal on T2-weighted MR

images, evident in early time points) were counted and multiplied by the section thickness appropriate for the method used. For *in vivo* MR imaging, T2-weighted transverse images were counted and multiplied by 1 mm; for *in vitro* MR imaging, transverse images were counted and multiplied by 39 μm . This same method was used to determine blood vessel leakage (hypointense signal on T2-weighted images), cavitation (focal hyperintense signal, evident in later time points), and total longitudinal injury length (summation of the individual pathological changes). Results for each group for each day were averaged together and compared. Statistical analysis of these data included a one-way between subjects ANOVA test to determine differences in injury severity between the four injury/treatment groups (SPSS, Chicago, IL). This was followed by a Tukey HSD post hoc test to interpret the significance of the ANOVA. Power analysis (power = 0.80) was done for results showing non-significant trends, including: (A) blood vessel leakage and (B) total longitudinal injury length.

Dynamic contrast-enhanced MR imaging processing was performed as described in Chapter 3. Peak enhancement was determined for each animal each day. Results were averaged for each injury/treatment group for each day and compared. Statistical analysis of these data included a one-way between subjects ANOVA test to determine differences in injury severity between the four injury/treatment groups (SPSS, Chicago, IL). This was followed by a Tukey HSD post hoc test to interpret the significance of the ANOVA.

Volume Analysis

For further quantification of injury characteristics, volumes were calculated for edema, blood vessel leakage, cavitation, and total injury for each of the four injury/treatment groups. Volume analysis was done using the OsiriX-Dicom Viewer (<http://homepage.mac.com/rossetantoine/osirix>). To calculate the volume of edema for a

specific cord, a data set was imported into OsiriX, and an ROI was drawn around all areas showing edema for each slice. Once the ROI's were drawn, they were summed together (to obtain an area) and multiplied by the slice thickness appropriate for each method used (to obtain a volume). For *in vivo* MR imaging, areas were multiplied by 1 mm; for *in vitro* MR imaging, areas were multiplied by 39 μm . Results were averaged for each group for each day and compared. Statistical analysis of these data included a one-way between subjects ANOVA test to determine differences in injury severity between the four injury/treatment groups (SPSS, Chicago, IL). This was followed by a Tukey HSD post hoc test to interpret the significance of the ANOVA. Power analysis (power = 0.80) was done for results showing non-significant trends (volume of blood vessel leakage).

Results

***In Vivo* High Resolution Magnetic Resonance Imaging**

Figure 4-2 shows a representative collection of T2-weighted MR images for the four injury/treatment groups for each day. Please refer to Chapter 3, Figure 3-1 for a description of the pathological findings seen on an *in vivo* T2-weighted MR image. All post-injury MR images for an animal were compared to their respective day 0 MR images, thus each animal served as its own control. T2-weighted images gave the best representation of injury, which showed hyperintense (i.e., bright) and hypointense (i.e., dark) signals, compared to a day 0 T2-weighted MR image, representing edema or cavitation and blood vessel leakage, respectively. The only information obtained from T1-weighted images was the injection track, which was seen as a hypointense signal as compared to a day 0 T1-weighted MR image.

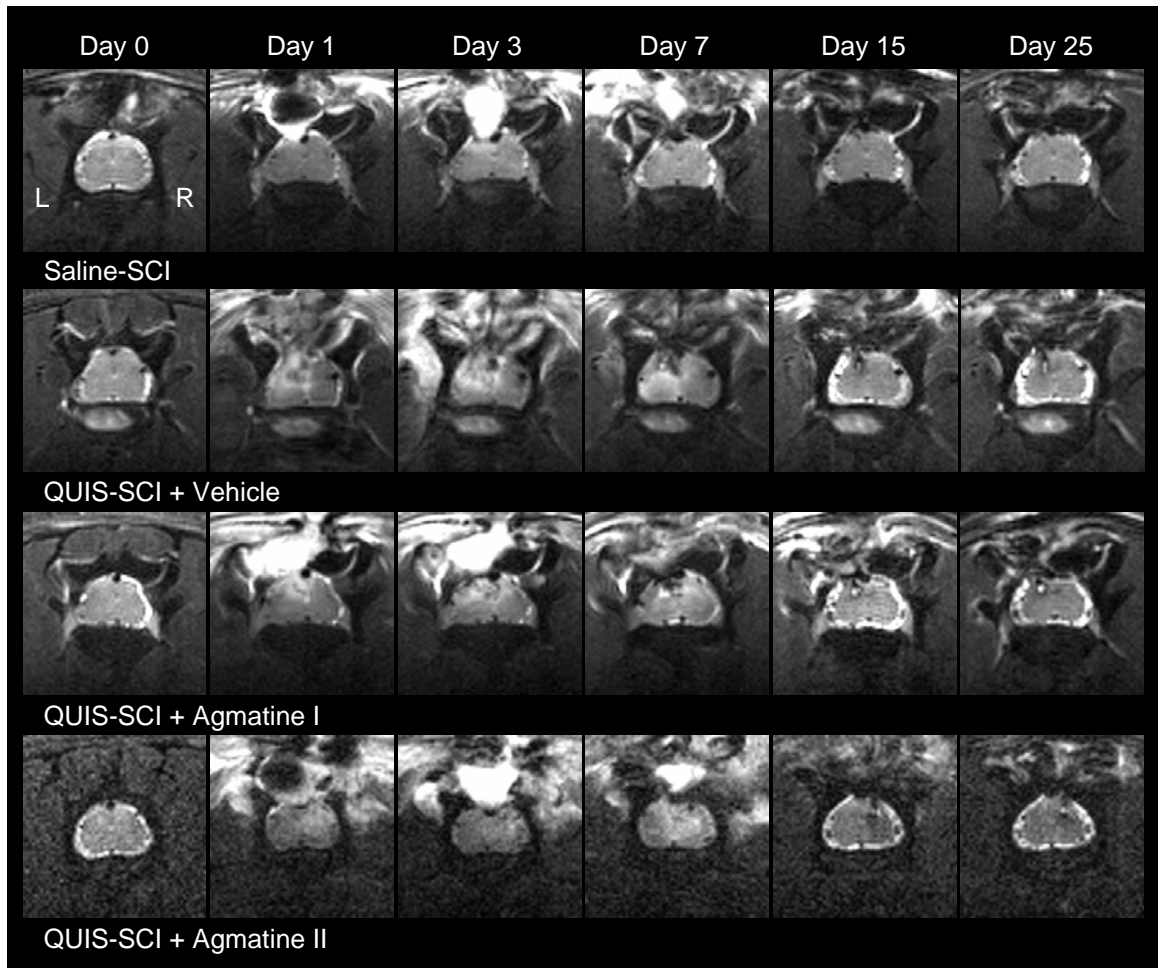


Figure 4-2. Representative T2-weighted (TR/effective TE = 2000 ms/62.5 ms; NA = 12) MR images for each injury/treatment group for each day. *In vivo* MR images are displayed with image size = 1.0 cm x 1.0 cm. MR images are sampled from the epicenter of the injury. Images are oriented with dorsal at the top. L, left side of cord; R, right side of cord, for all images.

The presence of edema was distinguished from the presence of cavitation, which both show as hyperintense signals on T2-weighted MR images, by the observation that edema is only observed in the earlier time points (completely subsides between days 7 and 15, Fig. 4-3) and is seen as a more diffuse, widespread hyperintense signal, whereas the presence of cavitation is only observed as early as day 15 (see Fig. 4-4) and is seen as a more intense and focal hyperintense signal. For example, in Figure 4-2, refer to the QUIS-SCI plus Vehicle MR images. Notice the difference in the hyperintense signal

seen on days 1, 3, and 7 versus days 15 and 25. The hyperintense signal is more widespread throughout the injured cord on the injection side on days 1, 3, and 7, whereas, the hyperintense signal seen on days 15 and 25 is more intense and focused mainly in the injection track.

To quantify the pathological changes (edema, cavitation, and blood vessel leakage) following either saline or QUIS injury, the number of transverse MR slices that contained edema (Fig. 4-3), cavitation (Fig. 4-4), or blood vessel leakage (Fig. 4-5) were counted and multiplied by the slice thickness for each day to show a longitudinal profile of each

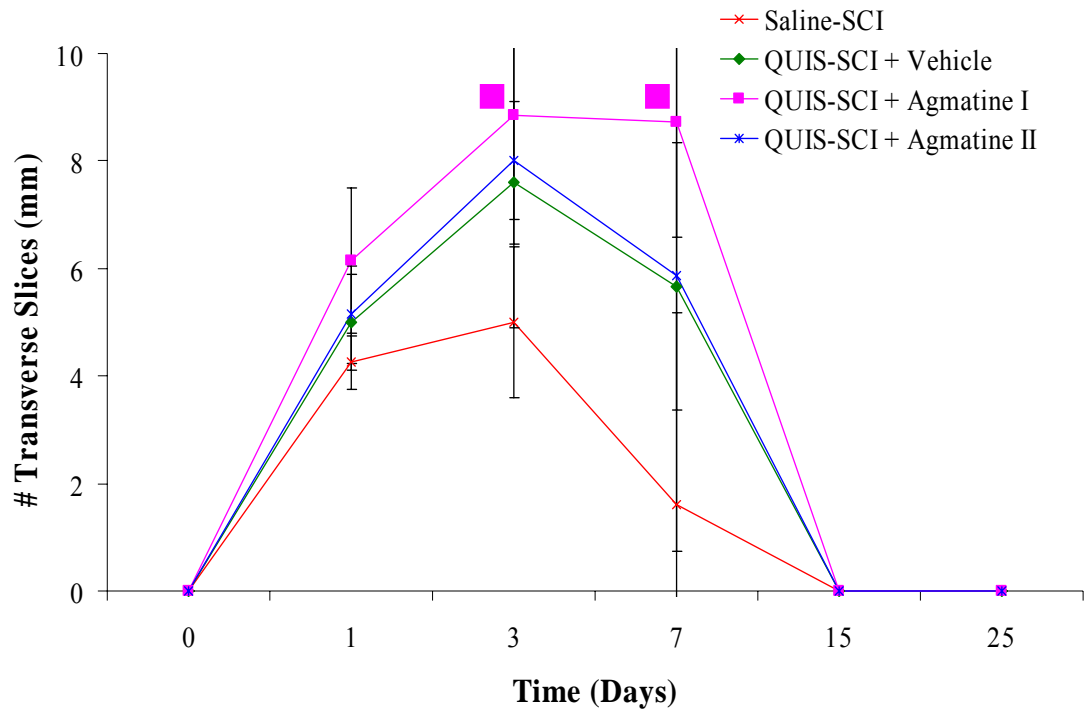


Figure 4-3. Longitudinal profile of the presence of edema for all injury/treatment groups as determined from *in vivo* T2-weighted transverse MR images. (■) $p < 0.02$, QUIS-SCI + Agmatine I versus Saline-SCI. Error bars represent one standard deviation. Data is represented as the number of transverse slices in millimeters showing edema. Edema is present on day 1 post-injury and subsides completely by day 15 for all injury/treatment groups.

pathological change. Additionally, the number of transverse slices that showed any combination of the above-mentioned pathological changes was summed and multiplied by the slice thickness to give a total injury length (Fig. 4-6).

In Figure 4-3, edema is observed immediately following injury (day 1 post-injury) in all injury/treatment groups, persists until day 7, and completely subsides by day 15. For the QUIS-SCI plus Agmatine I group, there was a significant increase in the number of transverse slices containing edema on days 3 ($p = 0.018$, one-way between subjects ANOVA, $F = 3.459$, $p = 0.024$) and 7 ($p = 0.007$, one-way between subjects ANOVA, $F = 4.390$, $p = 0.008$) as compared to the Saline-SCI group. There were no significant

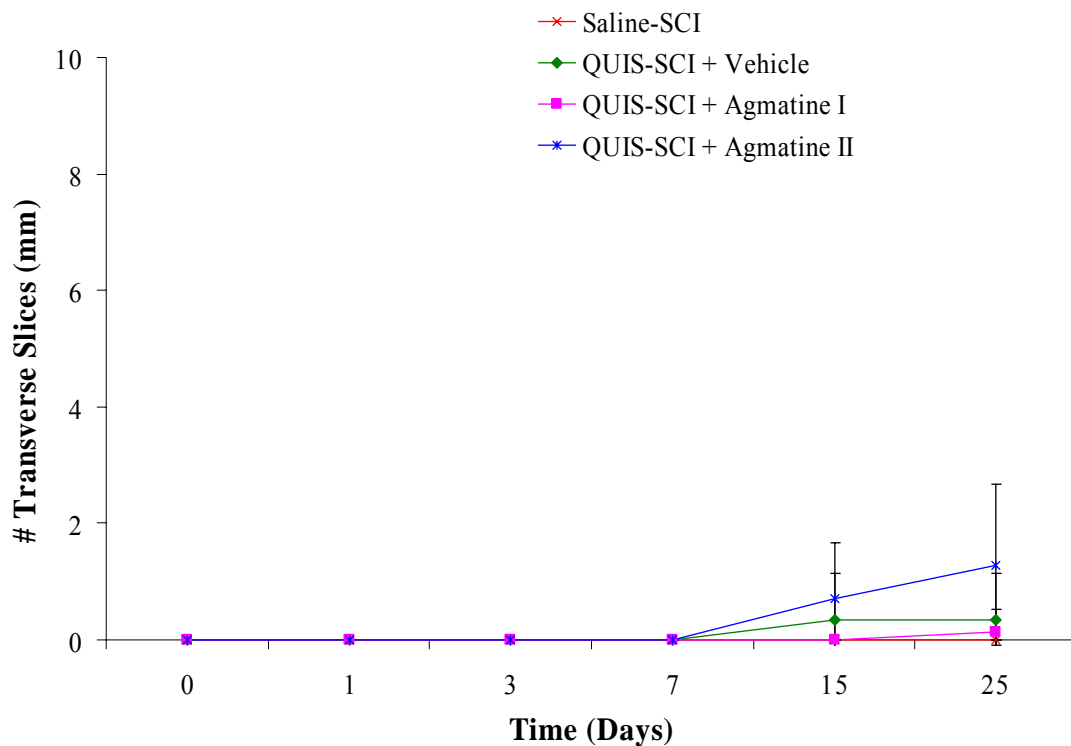


Figure 4-4. Longitudinal profile of the presence of cavitation for all injury/treatment groups as determined from *in vivo* T2-weighted transverse MR images. Error bars represent one standard deviation. Data is represented as the number of transverse slices in millimeters showing cavitation. Cavitation is present beginning on day 15 post-injury and continues on day 25 for all QUIS-SCI groups. No cavitation was observed in the Saline-SCI group.

differences in the presence of edema for the QUIIS-SCI plus Vehicle and QUIIS-SCI plus Agmatine II groups as compared to the Saline-SCI group for any of the time-points.

In Figure 4-4, cavitation is observed beginning at day 15 for only the QUIIS-SCI injury groups, regardless of treatment, and persists on day 25. No cavitation was observed for the Saline-SCI group. There were no significant differences in the number transverse slices containing cavitation for any of the QUIIS-SCI injury groups as compared to the Saline-SCI group.

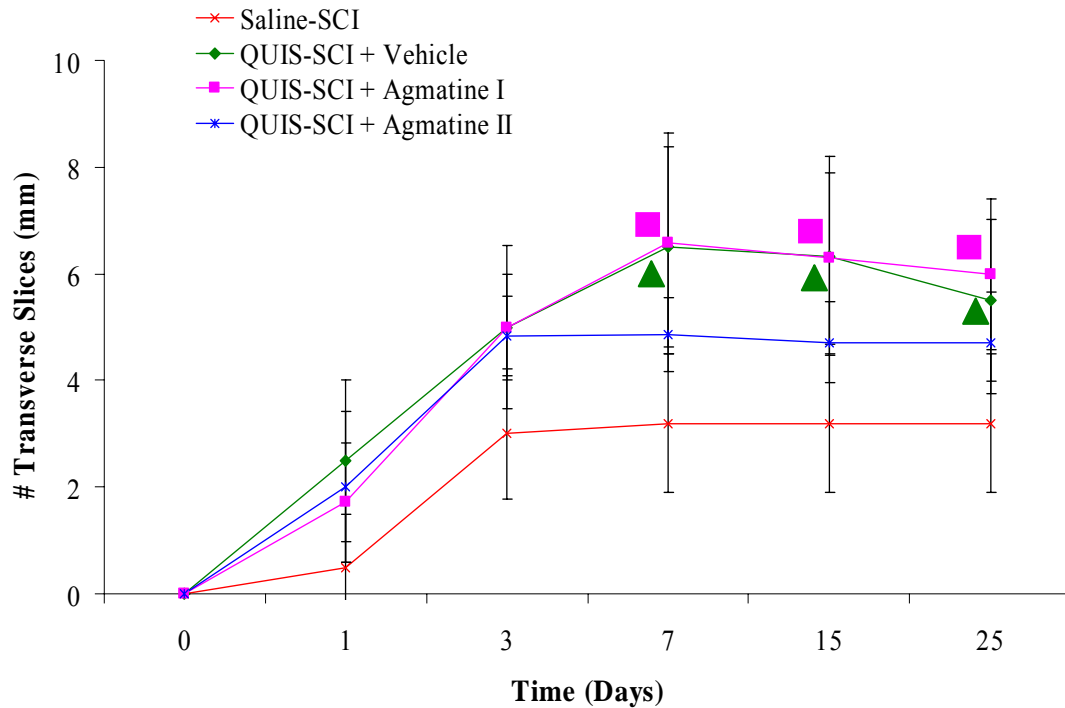


Figure 4-5. Longitudinal profile of the presence of blood vessel leakage for all injury/treatment groups as determined from *in vivo* T2-weighted transverse MR images. (■) $p < 0.01$, QUIIS-SCI + Agmatine I versus Saline-SCI; (▲) $p < 0.05$, QUIIS-SCI + Vehicle versus Saline-SCI. Error bars represent one standard deviation. Data is represented as the number of transverse slices in millimeters showing blood vessel leakage. Blood vessel leakage is observed on day 1 post-injury and continues to increase until day 7, at which point it seems to stabilize for all injury/treatment groups.

In Figure 4-5, blood vessel leakage is observed throughout all experimental time-points for all injury/treatment groups, increasing from day 1 to day 7, at which point, the amount of blood vessel leakage appears to remain constant. There was a significant increase, versus Saline-SCI, in the number of transverse slices containing blood vessel leakage on days 7 (one-way between subjects ANOVA, $F = 4.661$, $p = 0.006$) for the QUIS-SCI plus Vehicle ($p = 0.012$) and QUIS-SCI plus Agmatine I ($p = 0.007$) groups; 15 (one-way between subjects ANOVA, $F = 5.037$, $p = 0.004$) for the QUIS-SCI plus

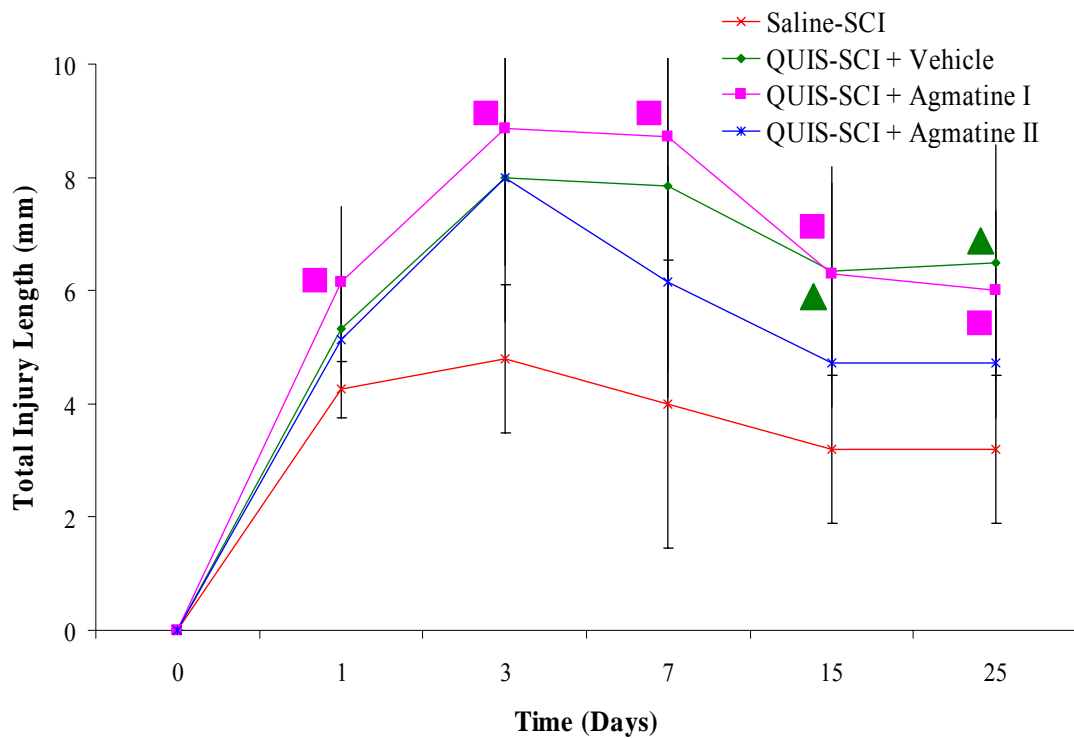


Figure 4-6. Longitudinal profile of the total pathology injury length (the presence of edema, blood vessel leakage, and cavitation combined) for all injury/treatment groups as determined from *in vivo* T2-weighted transverse MR images. (■) $p < 0.05$, QUIS-SCI + Agmatine I versus Saline-SCI; (▲) $p < 0.02$, QUIS-SCI + Vehicle versus Saline-SCI. Error bars represent one standard deviation. Data is represented as the number of transverse slices in millimeters showing any combination of edema, blood vessel leakage, and cavitation. The presence of edema is the largest contributor to the total injury length in the earlier time-points (days 1, 3, and 7), whereas, blood vessel leakage is the main contributor in the later time-points (days 15 and 25).

Vehicle ($p = 0.007$) and QUIS-SCI plus Agmatine I ($p = 0.006$) groups; and 25 (one-way between subjects ANOVA, $F = 4.390$, $p = 0.008$) for the QUIS-SCI plus Vehicle ($p = 0.042$) and QUIS-SCI plus Agmatine I ($p = 0.007$) groups. There were no significant differences in the presence of blood vessel leakage for the QUIS-SCI plus Agmatine II group as compared to the Saline-SCI group for any of the time-points. Although no significant differences were detected between QUIS-SCI plus Agmatine II and QUIS-SCI plus Vehicle groups, power analysis revealed that 8 animals for day 7, 8 animals for day 15, and 35 animals for day 25 would be required to obtain a significance at $p = 0.05$ at a power = 0.80.

The longitudinal profile of total injury length measured with *in vivo* transverse MR images is represented in Figure 4-6. The presence of edema is the primary contributor to the total injury length in the earlier post-injury time-points (days 1, 3, and 7), whereas, blood vessel leakage is the foremost contributor in the later post-injury time-points (days 15 and 25). For the QUIS-SCI plus Vehicle group, there was a significant increase in the total injury length on days 15 ($p = 0.007$, one-way between subjects ANOVA, $F = 5.037$, $p = 0.004$), and 25 ($p = 0.006$, one-way between subjects ANOVA, $F = 4.577$, $p = 0.007$) as compared to the Saline-SCI group. For the QUIS-SCI plus Agmatine I group, there was a significant increase in the total injury length on days 1 ($p = 0.049$, one-way between subjects ANOVA, $F = 2.672$, $p = 0.058$), 3 ($p = 0.009$, one-way between subjects ANOVA, $F = 4.087$, $p = 0.013$), 7 ($p = 0.029$, one-way between subjects ANOVA, $F = 3.430$, $p = 0.024$), 15 ($p = 0.006$, one-way between subjects ANOVA, $F = 5.037$, $p = 0.004$), and 25 ($p = 0.019$, one-way between subjects ANOVA, $F = 4.577$, $p = 0.007$), as compared to the Saline-SCI group. There were no significant differences in

total injury length for the QUIIS plus Agmatine II group as compared to the Saline-SCI group for any of the time-points. Although no significant differences were detected between QUIIS-SCI plus Agmatine II animals and QUIIS-SCI plus Vehicle, power analysis revealed that 31 animals for day 7, 13 animals for day 15, and 9 animals for day 25 would be required to obtain a significance at $p = 0.05$ at a power of 0.80. Refer to Table 4-1 for a summary of significance.

***In Vivo* Dynamic Contrast-Enhanced Magnetic Resonance Imaging**

To determine whether there was BSCB disruption at the day 0 and days 1, 3, 7, 15, and 25 post-injury time-points, DCE-MR imaging was performed using Gd as a contrast agent. Disruption of the BSCB was indicated by a significant Gd enhancement ($>10\%$) within the cord at the site of injury. Figure 4-7 provides a peak enhancement profile for all four injury/treatment groups for all time-points. No significant Gd enhancement was observed in any of the four injury/treatment groups at the day 0 (pre-injury) time-point. Gadolinium enhancement, however, was observed in surrounding muscle of all animals, approximately 300% peak signal intensity enhancement, which indicates that the procedure was performed correctly.

For the Saline-SCI group (sham injury), there was a significant increase in peak enhancement (one-way between subjects ANOVA, $F = 13.966$, $p < 0.001$) on days 1 ($p = 0.001$) and 3 ($p < 0.001$) as compared to day 0. For the QUIIS-SCI plus Vehicle group, there was a significant increase in peak enhancement (one-way between subjects ANOVA, $F = 52.422$, $p < 0.001$) on days 1 ($p < 0.001$), 3 ($p < 0.001$), and 7 ($p = 0.02$) as compared to day 0. For the QUIIS-SCI plus Agmatine I group, there was a significant increase in peak enhancement (one-way between subjects ANOVA, $F = 59.234$, $p < 0.001$) on days 1 ($p < 0.001$), 3 ($p < 0.001$), and 7 ($p = 0.012$) as compared to day 0. For

the QUIS-SCI plus Agmatine II group, there was a significant increase in peak enhancement (one-way between subjects ANOVA, $F = 31.807$, $p < 0.001$) on days 1 ($p < 0.001$), 3 ($p < 0.001$) and 7 ($p = 0.005$) as compared to day 0. When comparing between groups on individual days, there were no significant differences.

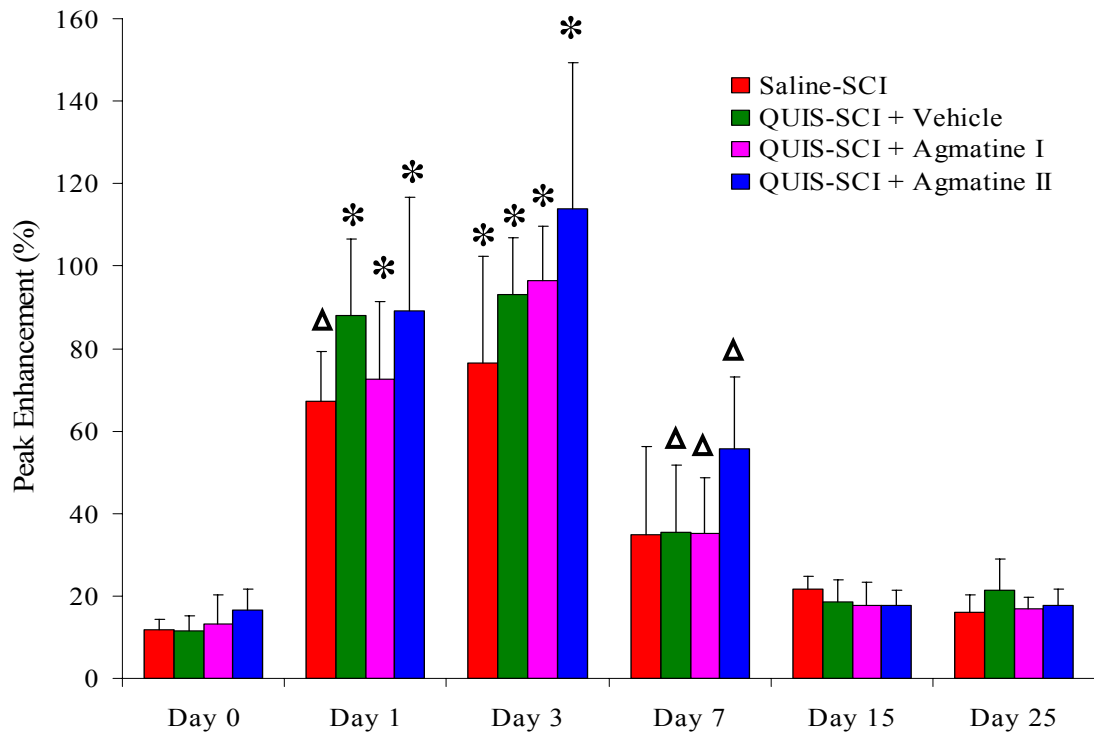


Figure 4-7. Summary of DCE-MRI BSCB disruption. Peak enhancement is represented as a percentage. There were significant differences in peak enhancement for all injury/treatment groups on days 1 and 3 as compared to day 0. There were significant differences in peak enhancement for the QUIS-SCI injury groups, but not the saline-SCI group on day 7 as compared to day 0. No significant disruption was observed on days 15 and 25 as compared to day 0. Additionally, no significant differences were observed between the injury/treatment groups for any of the days. (*) $p < 0.001$, (Δ) $p < 0.01$. Error bars represent one standard deviation.

Volume Analysis

To further quantify pathological changes (edema, cavitation, and blood vessel leakage) following either saline or QUIS injury, regions of interest were drawn, using transverse MR images, around areas showing edema (Fig. 4-8), blood vessel leakage (Fig. 4-9), or cavitation (Fig. 4-10), and were summed and multiplied by the appropriate slice thickness for each animal and time-point to obtain a volume for each of the above mentioned pathological changes. Additionally, a region of interest was drawn around the entire injured area (edema, blood vessel leakage, and cavitation combined) for each slice,

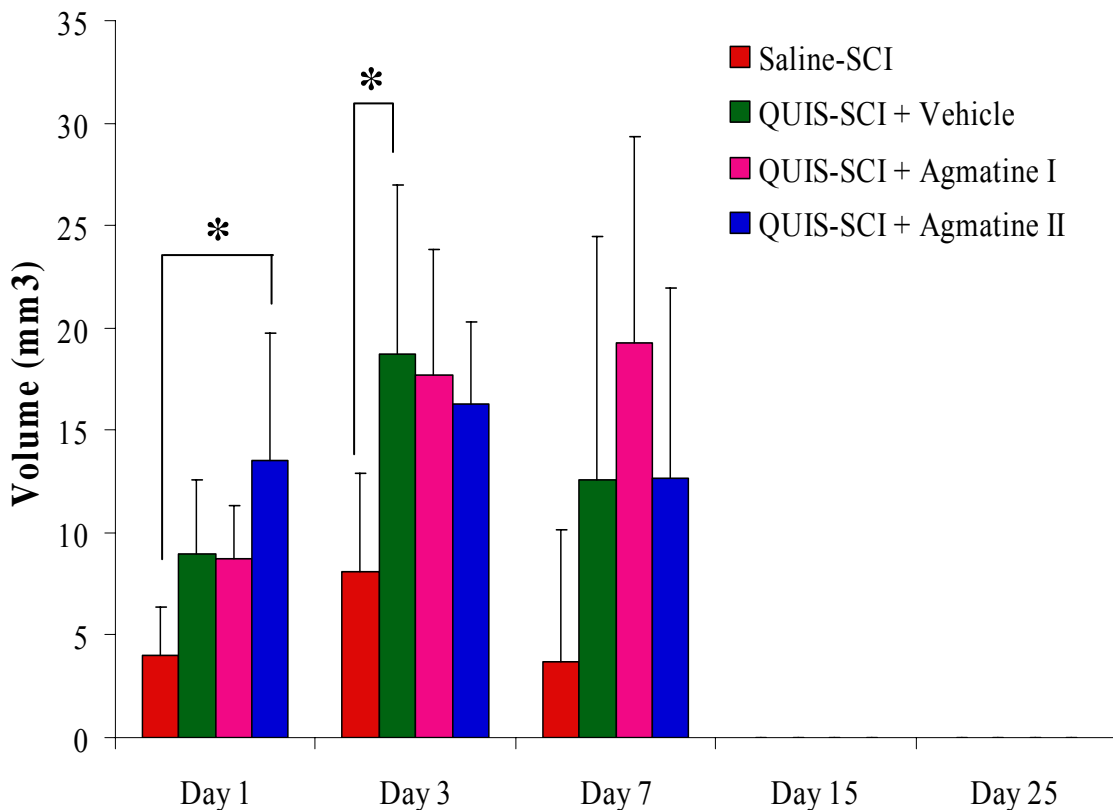


Figure 4-8. Volume of edema for all injury/treatment groups as determined from *in vivo* T2-weighted transverse MR images. (*) $p \leq 0.05$. Error bars represent one standard deviation. Data is represented as the volume in cubic millimeters.

summed and multiplied by the appropriate slice thickness for each animal and time-point to give an overall volume of injury (Fig. 4-11).

The volume of edema peaks at day 3 and starts diminishing day 7 for all injury/treatment groups except the QUIS-SCI plus Agmatine I group. This profile closely matches that shown in Figure 4-3. There was a significant increase in volume of edema on day 1 (one-way between subjects ANOVA, $F = 3.286$, $p = 0.03$) between the QUIS-SCI plus Agmatine II and Saline-SCI groups ($p = 0.014$). Additionally, the QUIS-SCI plus Vehicle group showed a significantly higher volume of edema ($p = 0.05$, one-way between subjects ANOVA, $F = 3.053$, $p = 0.037$) as compared to the Saline-SCI

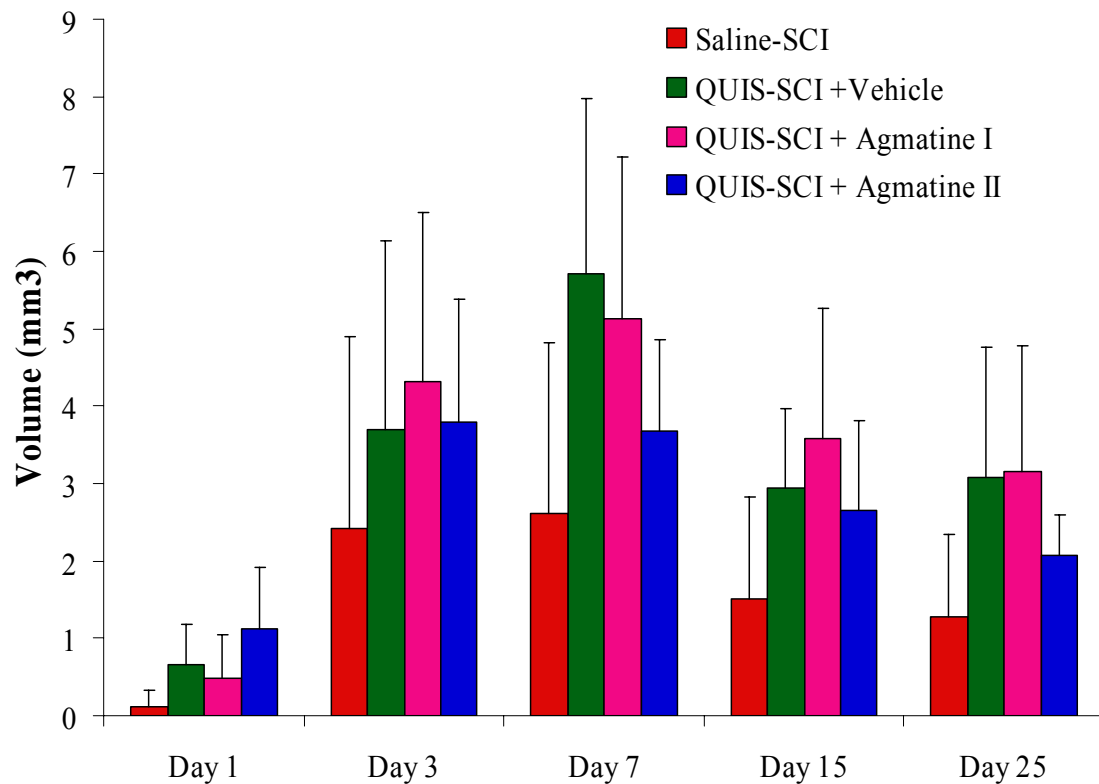


Figure 4-9. Volume of blood vessel leakage for all injury/treatment groups as determined from *in vivo* T2-weighted transverse MR images. Error bars represent one standard deviation. Data is represented as the volume in cubic millimeters.

group. No significant differences were observed on day 7 for any of the QUIS-SCI groups as compared to the Saline-SCI group.

Figure 4-9 illustrates the volume of blood vessel leakage profile, and shows an increase in volume through day 7 and a slight decrease in volume on days 15 and 25. The increase seen is consistent with that seen in Figure 4-5; however, volume analysis becomes a more sensitive outcome measure for days 15 and 25, as Figure 4-5 shows a constant level of blood vessel leakage (due to the method of quantification), whereas the volume shows a slight decrease. No significant differences in volume of blood vessel

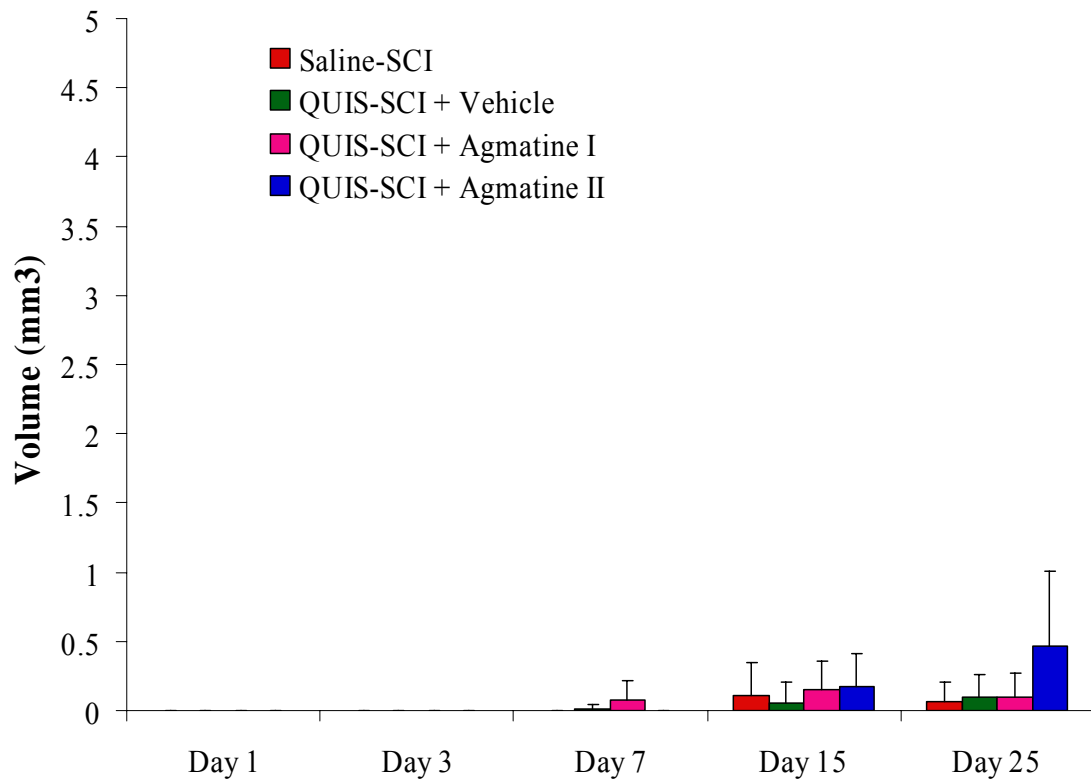


Figure 4-10. Volume of cavitation for all injury/treatment groups as determined from *in vivo* T2-weighted transverse MR images. Error bars represent one standard deviation. Data is represented as the volume in cubic millimeters.

leakage were detected between any of the QUIIS-SCI groups versus the Saline-SCI group. Although no significant differences were detected between QUIIS-SCI plus Agmatine II animals and QUIIS-SCI plus Vehicle, power analysis revealed that 9 animals for day 7, 252 animals for day 15, and 19 animals for day 25 would be required to obtain a significance at $p = 0.05$ at a power of 0.80.

The volume of cavitation following injury is presented in Figure 4-10. The volume profile is also consistent with the longitudinal profile of the presence of cavitation (Fig. 4-4). Cavitation was observed in all QUIIS-SCI groups, but was not present in the Saline-SCI group. Similar to the longitudinal profile data, there are no significant differences in the volume of cavitation following a QUIIS lesion as compared to a saline lesion.

Finally, the total injury volume, which consisted of edema, blood vessel leakage, and cavitation is shown in Figure 4-11. As seen with the individual volumes of pathological changes, the total injury volume profile is similar to the total longitudinal injury length profile (Fig. 4-6). The edema volume is highly represented in the earlier time-points post-injury, whereas the volume of blood vessel leakage is more highly represented in the later time-points. The only significant differences in total injury volume was seen on day 1 (one-way between subjects ANOVA, $F = 3.801$, $p = 0.017$) between the QUIIS-SCI plus Agmatine II group and the Saline-SCI group ($p = 0.007$). This is consistent with the significance seen in Figure 4-8. Refer to Table 4-2 for a summary of significance.

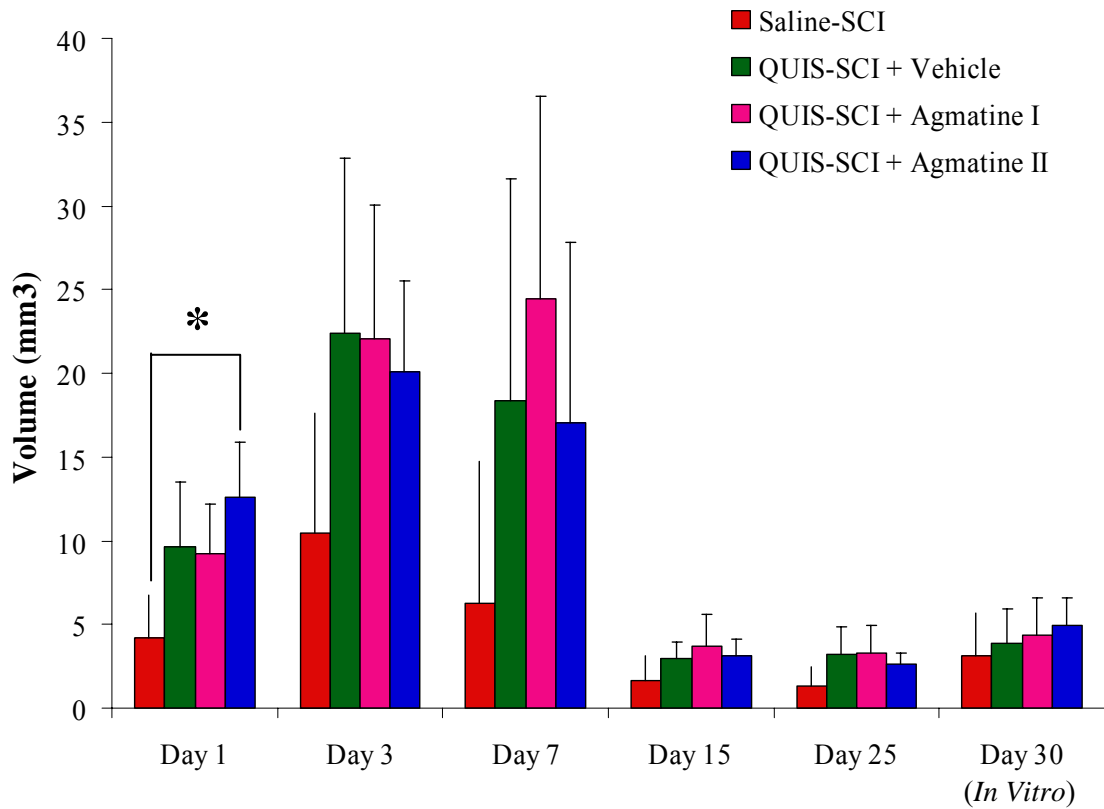


Figure 4-11. Volume of total injury (volume of edema, blood vessel leakage, and cavitation combined) for all injury/treatment groups as determined from *in vivo* T2-weighted transverse MR images (days 1, 3, 7, 15, and 25) and *in vitro* transverse 3D MRM images (day 30). (*) $p = 0.007$. Error bars represent one standard deviation. Data is represented as the volume in cubic millimeters.

Table 4-1. Summary of Significant Differences in Longitudinal Profiles of Edema, Cavitation, and Blood Vessel Leakage, and BSCB Disruption.

Injury/Treatment Group versus Saline-SCI	Edema (longitudinal profile) (A) Figure 4-3	Cavitation (longitudinal profile) (B) Figure 4-4	Blood Vessel Leakage (longitudinal profile) (C) Figure 4-5	Total Injury Length (A+B+C) Figure 4-6	BSCB Disruption Figure 4-7
QUIS + Vehicle	-	-	↑, p < 0.05 (days 7, 15, 25)	↑, p < 0.02 (days 15, 25)	-
QUIS + Agmatine I	↑, p < 0.02 (days 3, 7)	-	↑, p < 0.01 (days 7, 15, 25)	↑, p < 0.05 (days 1, 3, 7, 15, 25)	-
QUIS + Agmatine II	-	-	-	-	-

Table 4-2. Summary of Significant Differences in Volumes of Edema, Blood Vessel Leakage, and Cavitation.

Injury/Treatment Group versus Saline-SCI	Edema (Volume) (A) Figure 4-8	Blood Vessel Leakage (Volume) (B) Figure 4-9	Cavitation (Volume) (C) Figure 4-10	Total Injury Volume (A+B+C) Figure 4-11
QUIS + Vehicle	↑, p < 0.05 (day 3)	-	-	-
QUIS + Agmatine I	-	-	-	-
QUIS + Agmatine II	↑, p < 0.05 (day 1)	-	-	↑, p < 0.01 (day 1)

Discussion

The goal of the present study was to use magnetic resonance imaging to evaluate the neuroprotective effects of an agent, with known pharmacologic actions, on the excitotoxic spinal cord injury model at different time-points in the same animal. Major findings include: (1) high resolution, *in vivo* MRI can be used to quantitatively and qualitatively study the dynamic changes in spinal cord injury pathology and blood-spinal cord-barrier integrity over time in the same animal; and (2) administration of 80 mg/kg agmatine (Agmatine II) post-injury resulted in neuroprotection against blood vessel leakage and edema following QUIS-SCI when compared to the Saline-SCI group.

The results have shown that MR images provide details of pathologic changes, easily detected both *in vivo* and *in vitro*. These changes include cavities, blood vessel leakage, cavitation, and tissue loss. Injury was observed unilaterally in some animals and bilaterally in others. This difference is mainly due to inconsistency in the injection technique. Despite every effort to control the depth of injection, variance was found among injury depths, most likely accounting for differences in injury severity. As discussed previously (refer to Chapter 3, “Discussion”), injuries following a deeper injection resulted in a more extensive injury both rostrocaudally and ventrally, showing bilateral blood vessel leakage and cavitation, whereas with a shallower lesion, damage was less severe resulting only in ipsilateral blood vessel leakage.

Differences in injury severity may also account for the significant increase in edema following the administration of 25 mg/kg agmatine (Agmatine I). There were variances in injection depth in each group; the QUIS-SCI plus Agmatine I group showing the highest variability in injury severity. More animals would need to be analyzed to reduce the variability and rule out the action of the drug as the cause. Additionally,

although there were no significant differences observed between any of the four injury/treatment groups, a neuroprotective trend was observed following 80 mg/kg agmatine (Agmatine II) seen in the volume of edema on days 3 and 7; blood vessel leakage on days 3, 7, 15, and 25; and total injury volume on days 3, 7, 15, and 25. Increasing the number of animals would also reduce variability and provide significance.

An equally important finding in this study was the sensitivity and capability of *in vivo* MR imaging to study the neuroprotective effects of agmatine in a progressive model of spinal injury over time in the same animal. It is important in research to affectively minimize resources and cost. With the capability of using an animal as its own control in a time-course study, the need for an excessive number of animals to obtain multiple data time-points is eliminated, as shown in the current study. The data is thus more accurately comparable, as it allows you to compare pre- and post-injury data for a single animal.

Secondary injury events, such as neural degeneration and cavitation in spinal injury, both a result of glutamate induced excitotoxicity, have been well documented (Faden and Simon, 1988; Nag and Riopelle, 1990; Hao et al., 1991; Yeziarski et al., 1993; Wrathall et al, 1994). These studies indicate that elevations in glutamate signify the initiation of cellular cascades that influence excitability and survivability of surrounding neurons. Limiting such events through the use of neuroprotective agents would have a profound impact on secondary processes involved in the mediation of cell death and the progression of secondary injury in SCI. Agmatine, a cationic amine formed by the decarboxylation of arginine, is such an agent that has been shown to affectively block NMDA receptor activity (Yang and Reis, 1999) and reduce the production of nitric oxide by inhibiting NOS (Auguet et al., 1995; Galea et al., 1996).

The present results showed that during a survival period of 30 days, 80 mg/kg agmatine (Agmatine II) provided neuroprotection most strongly against edema and blood vessel leakage. The vehicle and 25 mg/kg agmatine (Agmatine I) treatment groups did not show neuroprotection, as expected. Although a higher volume of edema was observed in the QUIS-SCI plus Agmatine II group compared to the Saline-SCI group, it was not as widespread, which is evident in the longitudinal profile of edema, meaning that the edema was more concentrated around the epicenter of the injury. The same is true for the total volume of injury; while the QUIS-SCI plus Agmatine II group had a higher volume of injury compared to the Saline-SCI group, the injury was not as widespread along the rostral-caudal axis of the cord. This raises the question of whether volume or rostral-caudal extent is more important. Previous studies have shown that length is a more determining factor in relation to behavioral outcome. For example, studies have shown a relationship between the onset of excessive grooming behavior and the longitudinal extent of excitotoxic damage produced by a QUIS lesion (Yeziarski et al., 1998; Gorman et al., 2001; Plunkett et al., 2001; Yu et al., 2003). Yu et al. (2003) suggested that by limiting the spread of QUIS induced excitotoxic damage via neuroprotection, the expression of injury-induced pain behaviors may lessen. This is one indication that the longitudinal profile versus volume results hold a stronger indication of neuroprotection.

Observing changes in the dynamics of the BSCB is important in understanding the destructive pathologic processes resulting from an excitotoxic lesion (Rapoport, 1976; Bradbury, 1979). Understanding the time course of permeability of the BSCB and the subsequent pathological consequences is crucial in understanding the secondary

mechanisms associated with spinal cord injury. Previous studies by Runge et al. (1997) and Bilgen et al. (2001) involving the contusion injury have shown cord-barrier disruption during the acute phase of injury. Previously, it was shown that in later time-points (i.e., 17-24 days post-injury), the barrier was intact following a QUIS lesion (Chapter 3, Berens et al., 2005). At the time-points used in this study, a dynamic profile of BSCB disruption was achieved. The BSCB showed disruption immediately (day 1) following injury, and persisted until day 7 post-injury, with a maximum disruption on day 3 post-injury. Repair of the barrier was evident, because on day 7, even though there was a significant increase in peak enhancement, there was an overall decrease in value as compared to earlier time-points (days 1 and 3). No significant differences were observed between any of the injury/treatment groups compared to the Saline-SCI group indicating that agmatine may not play a significant role in attenuating cord-barrier disruption.

CHAPTER 5
DIFFUSION WEIGHTED MR IMAGING OF THE EXCISED QUISQUALIC ACID
LESIONED RAT SPINAL CORD

Introduction

Diffusion weighted MR imaging of water translational diffusion has been utilized to provide information beyond the anatomic and spatial resolution of conventional magnetic resonance imaging. It has a greater sensitivity, compared to conventional MR techniques, in evaluating the integrity of injured white matter (Ford et al., 1994a), and assessing the degree of neuroprotection, axonal sprouting, and regeneration following therapy (Nevo et al., 2001; Schwartz et al., 2003; Schwartz et al., 2005).

White and gray matter vary in their diffusion characteristics due to their structural makeup. When considering diffusion properties, it is important to consider microstructure properties, such as cell size and density, cell orientation, membrane permeability, and intracellular and extracellular viscosity of the tissue. In addition, cell membranes and myelin can also restrict water diffusion along the axis perpendicular to white matter tracts (Beaulieu, 2002; Schwartz and Hackney, 2003). Water diffusion in gray matter is fairly unrestricted and its directionality is more random than white matter. However in white matter, diffusion is along bundles of parallel, myelinated axons, is restricted (Moseley et al., 1990). Thus, normal spinal cord is considered anisotropic, since there are more barriers to diffusion in the plane transverse to the long axis of the cord (Schwartz and Hackney, 2003).

In the present study, DWI was used to detect changes in fiber structure in white and gray matter following excitotoxic spinal injury. It is hypothesized that DWI can be employed to evaluate the long term effects of excitotoxic injury on fiber tracts, and that it has the sensitivity to detect differences in gray matter fiber structure between control (non-injured) and QUIS lesioned cords.

Materials and Methods

Animals, Surgery, and Neuroprotection

Sprague-Dawley male rats weighing 250-300g were subjected to excitotoxic spinal cord injury as described in Chapter 4. Rats were randomly assigned to one of three injury groups: (1) Control (no injury, N = 3); (2) Saline-SCI (sham injury, N = 5); and (3) QUIS-SCI (N = 8). Animals were sacrificed on day 30 post-injury, and cords prepared as described in Chapter 3. Different groups were used than those described in Chapter 4 in order to verify the technique. Differences needed to be observed between the three groups listed above before using this methodology in the assessment of neuroprotective treatment (see Chapter 6, “Future Directions”).

***In Vitro* Three Dimensional MR Microscopy and Diffusion Weighted Imaging**

All *in vitro* NMR measurements were performed on a 14.1T, 51-mm-bore Oxford magnet, at 600 MHz, using a Bruker BIOSPEC Avance DBX console. All excised cords were subjected to *in vitro* three-dimensional MR microscopy as described in Chapter 4, with cord preparation described in Chapter 3. Following 3D MRM acquisition, diffusion weighted MR images were acquired using a spin-echo, high angular resolution diffusion imaging (HARDI, Tuch et al., 2002) acquisition sequence (TR/TE = 1400 ms/25 ms) with gradients applied in 46 directions with a gradient strength of 664 mT/m (b-value of 1250 s/mm²). A low b-value image was also obtained with a gradient strength of 175

mT/m (b-value of 100 s/mm²) applied in 6 directions. Additional parameters were echo crusher duration = 0.12ms, Δ value = 17.5 ms, δ value = 1.5 ms, bandwidth = 32 kHz, FOV = 4.2 x 4.2 x 12.0 mm³, matrix = 70 x 70 with 40 slices, and resolution = 60 x 60 x 300 μ m³. Scan times were 9.5 hours for each cord. General image processing and analysis was performed using custom software written in the Interactive Data Language (IDL, from Research Systems, Boulder, CO).

Data Analysis

Diffusion weighted MR data were fit to a rank-2 tensor model as the initial method of analysis. To determine the fractional anisotropy and average diffusivity of the white and gray matter for each animal of each injury group, regions of interest (ROI) were drawn using the S₀ MR image in the following regions of white matter (Fig. 5-1): A, dorsal column, right side; B, dorsal column, left side; C, lateral, right side; D, lateral, left side; E, ventral, right side; and F, ventral, left side; and in the following regions of gray matter (Fig. 5-2): A, dorsal horn, non-injured side; B, lateral, right side; C, lateral, left side; D, ventral, right side; and E, ventral, left side. Regions of interest were not drawn in the dorsal horn on the injured side, because a value of zero would result; an outcome due to the hypointensity of the signal. For each outcome measurement (i.e., fractional anisotropy and average diffusivity), values were averaged for each ROI and injury group. Saline and QUIS injury groups were then compared to the control group.

To further characterize the QUIS lesions, a diffusion orientation transform (DOT) method (Ozarslan, et al., 2006) was applied to the analysis of excised rat spinal cord, diffusion-weighted image data acquired with the HARDI acquisition scheme. The DOT has recently been developed to resolve the architecture of complex structured tissue. The DOT transforms the HARDI measured diffusivity profiles into displacement probability

profiles, representing the probability of diffusion in a particular direction. Rather than fit the measured diffusion signal to a rank-2 model of diffusion, the DOT method assumes the signal attenuation (as a function of diffusion weighting) is represented by a mono-exponential decay. Then this signal attenuation is used to directly calculate the displacement probability, as a function of position, using a q-space Fourier transformation (Callaghan, 1991). Therefore, the peaks in these displacement probability profiles correspond to distinct fiber orientations. Using the DOT, the QUIS lesion can be further characterized to delineate and describe complex fiber structures, specifically in the gray matter.

Results

First, to determine the effects of saline and QUIS lesions on white matter as compared to control (no injury), average diffusivity (AD) and fractional anisotropy (FA) values were calculated for the six white matter regions described above for each injury group (see “Data Analysis”, Fig. 5-1). Data for each group was combined and averaged by matching and centering injured areas for each cord, because values along the rostrocaudal axis in a normal cord did not vary (i.e., it was not necessary to match the slices anatomically). Fractional anisotropy values of one indicate anisotropic (unidirectional) diffusion; zero indicates isotropic (non-preferential) diffusion. Figures 5-3 through 5-5 show the AD and FA values of white matter for the Control, Saline-SCI, and QUIS-SCI groups, respectively. The AD values in control cords were very consistent along the rostral-caudal axis (Fig. 5-3A). However, there was a marginal increase in AD from rostral to caudal in both Saline- and QUIS-SCI groups (Figs. 5-4A and 5-5A, respectively). Fractional anisotropy decreased slightly from rostral to caudal for all three groups but was equivalent between all six regions of interest in white matter

(Figs. 5-3B, 5-4B, and 5-5B). There were no significant differences in AD or FA values between any of the six white matter regions of interest for any of the three groups. There were no significant differences in AD or FA between any of the injury groups as compared to control.

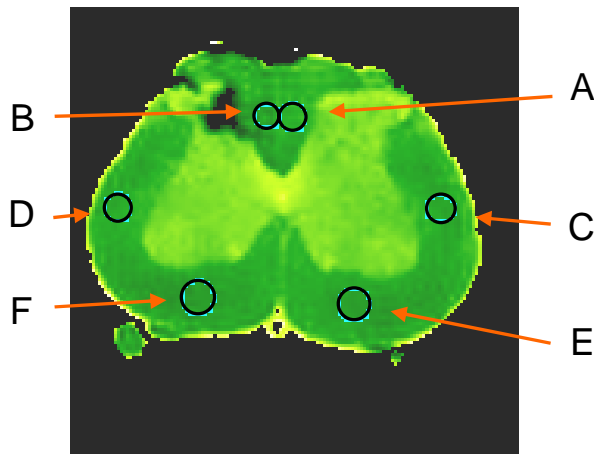


Figure 5-1. S_0 ($b = 100 \text{ s/mm}^2$) transverse MR image from a QUIs lesioned animal showing regions of interest drawn for analysis of the white matter. A, dorsal column white matter, right side; B, dorsal column white matter, left side; C, lateral white matter, right side; D, lateral gray matter, left side; E, ventral gray matter, right side; F, ventral gray matter, left side.

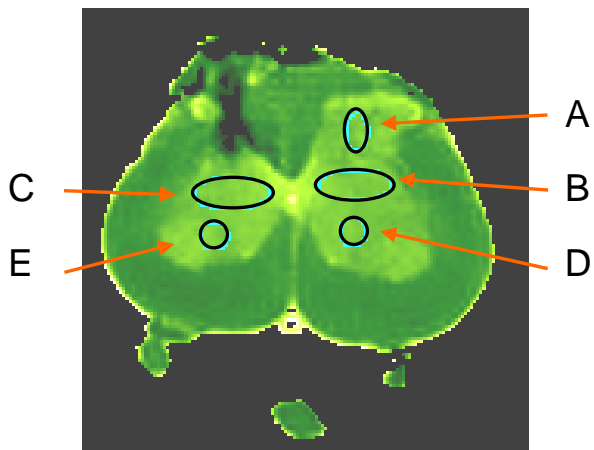
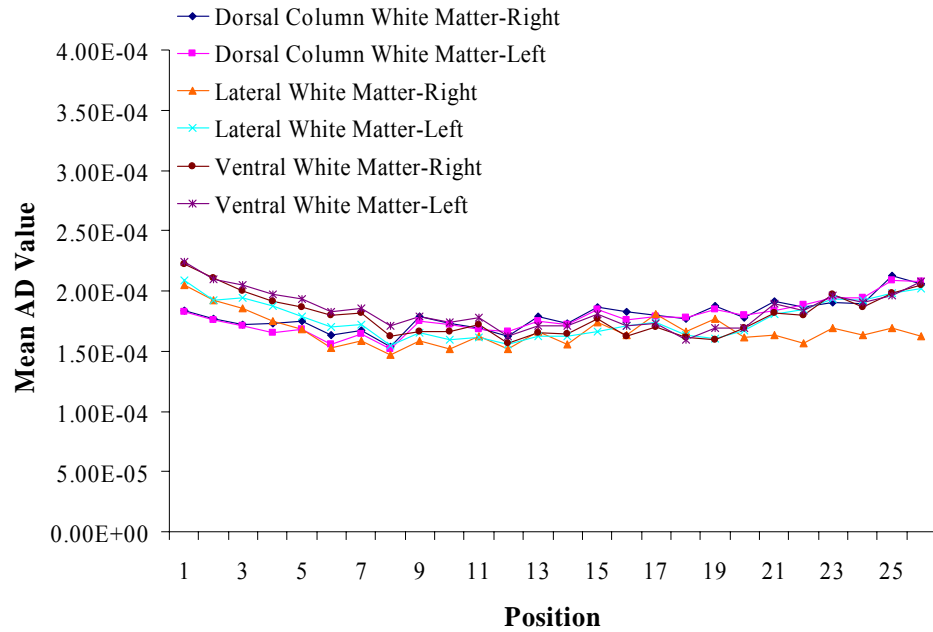


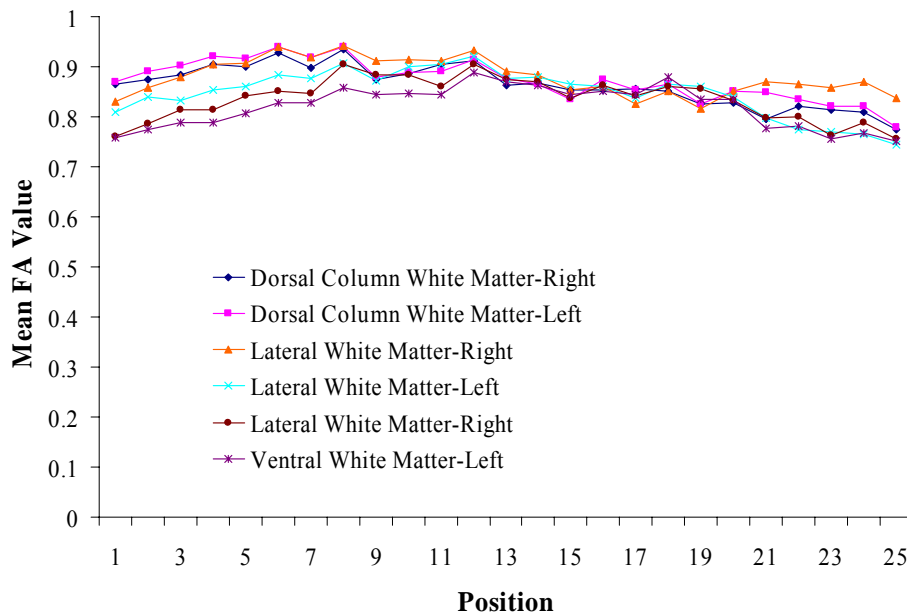
Figure 5-2. S_0 ($b = 100 \text{ s/mm}^2$) transverse MR image from a QUIs lesioned animal showing regions of interest drawn for analysis of the gray matter. A, dorsal horn gray matter, non-injured side; B, lateral gray matter, right side; C, lateral gray matter, left side; D, ventral gray matter, right side; E, ventral gray matter, left side.

Second, to determine the effects of the saline and QUIS lesions on gray matter as compared to control (no injury), AD and FA values were also calculated for the five gray matter regions described above for each injury group (see “Data Analysis”, Fig. 5-2). Figures 5-6 through 5-8 show the AD and FA values of gray matter for the Control, Saline-SCI, and QUIS-SCI groups, respectively. The AD values for gray matter for all three groups were very consistent along the rostral-caudal axis (Figs. 5-6A, 5-7A, 5-8A). Fractional anisotropy remained constant from rostral to caudal for the Saline-SCI group but had a negligible increase in the Control and QUIS-SCI groups (Figs. 5-6B and 5-8B, respectively). There were no significant differences in AD or FA values between any of the five gray matter regions of interest for any of the three groups. Surprisingly, there were no significant differences in AD or FA between any of the injury groups as compared to control.

Since, no differences were detected with the initial series of analysis, DOT analysis was used to determine if this more sensitive method could detect changes in white and gray matter fibers in control and QUIS-SCI cords (Fig. 5-9). In the Control group (Fig. 5-9A, C), white matter fiber orientation was observed to be out of the plane of section (i.e., along the long axis of the cord), as expected. Gray matter fibers showed a much more complex orientation and were observed to be in the plane section, also as expected. Fibers situated in the ventral regions of the gray matter appear to be more complex than those in dorsal regions of the dorsal horn. Most interestingly, however, are fibers in the substantia gelatinosa; they appear to align along the long axis of the cord. One would expect fibers to be within the transverse plane versus along the long axis, as fibers enter the substantia gelatinosa from the dorsal roots and traverse into the dorsal horn.

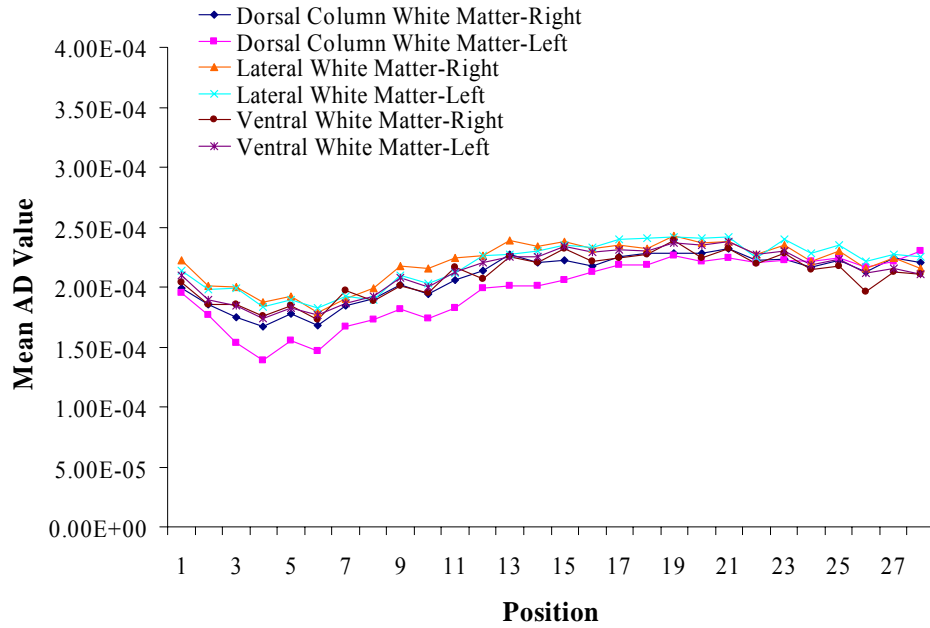


A

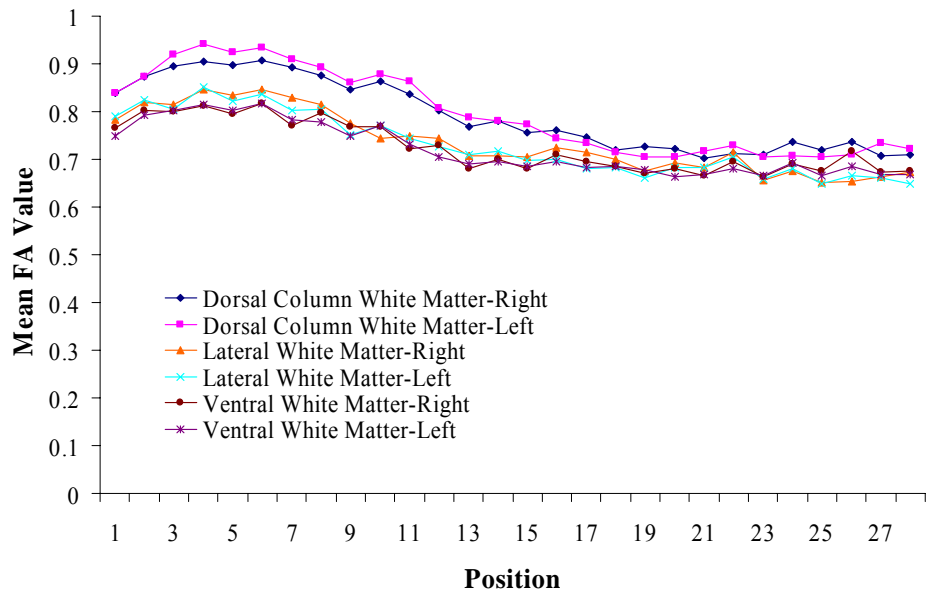


B

Figure 5-3. Average diffusivity and fractional anisotropy values for Control white matter. Position is rostral (left side of graph) to caudal (right side of graph). (A) Average diffusivity along the rostral-caudal axis of white matter is consistent. No significant differences were detected between any of the control white matter regions for either of the measurements. (B) There was a slight decrease in FA from rostral to caudal for all white matter regions.

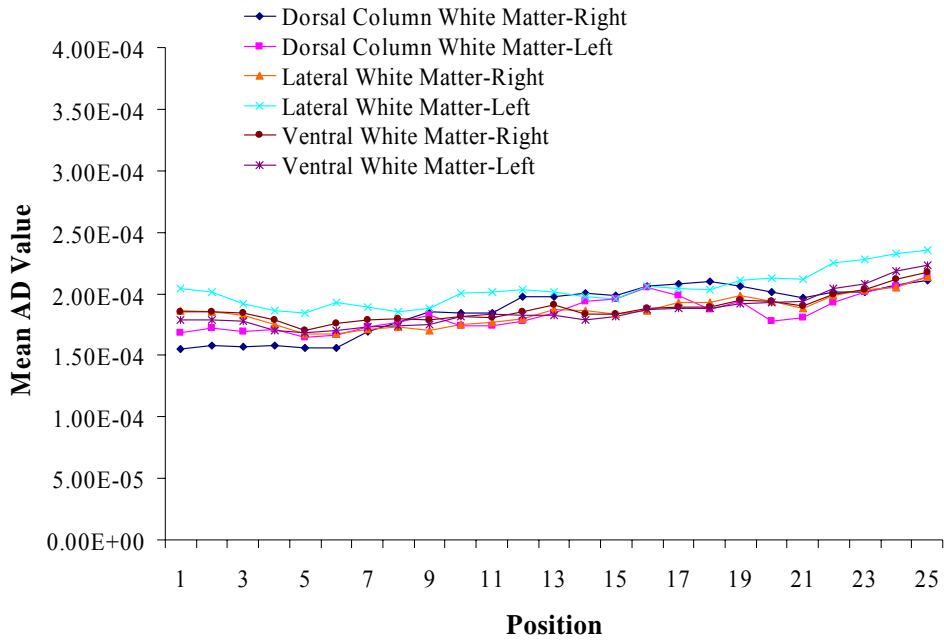


A

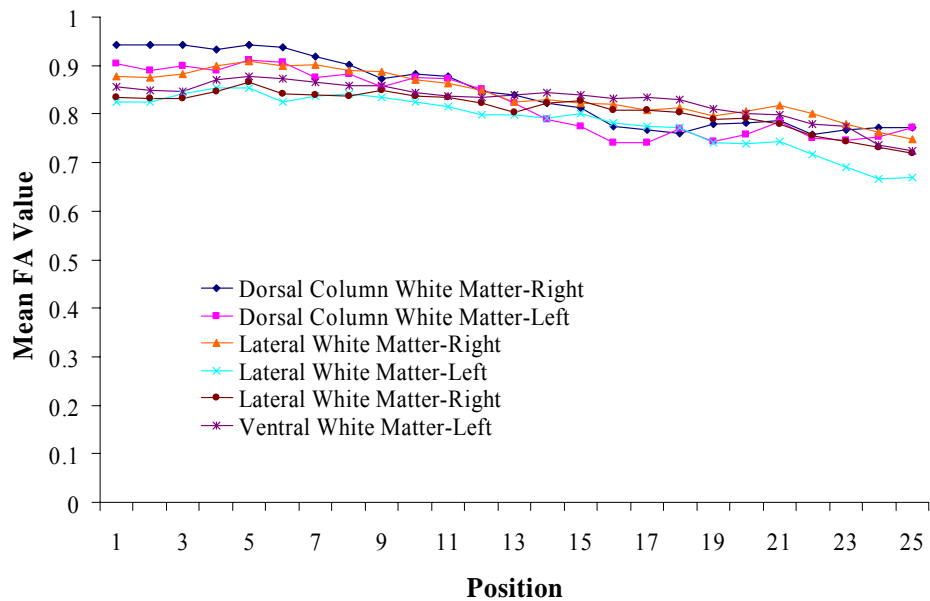


B

Figure 5-4. Average diffusivity and fractional anisotropy values for Saline-SCI white matter. Position is rostral (left side of graph) to caudal (right side of graph). (A) Average diffusivity along the rostral-caudal axis of white matter is consistent, with a slight increase along the rostral caudal axis. No significant differences were detected between any of the control white matter regions for either of the measurements. (B) There was a slight decrease in FA from rostral to caudal for all white matter regions.

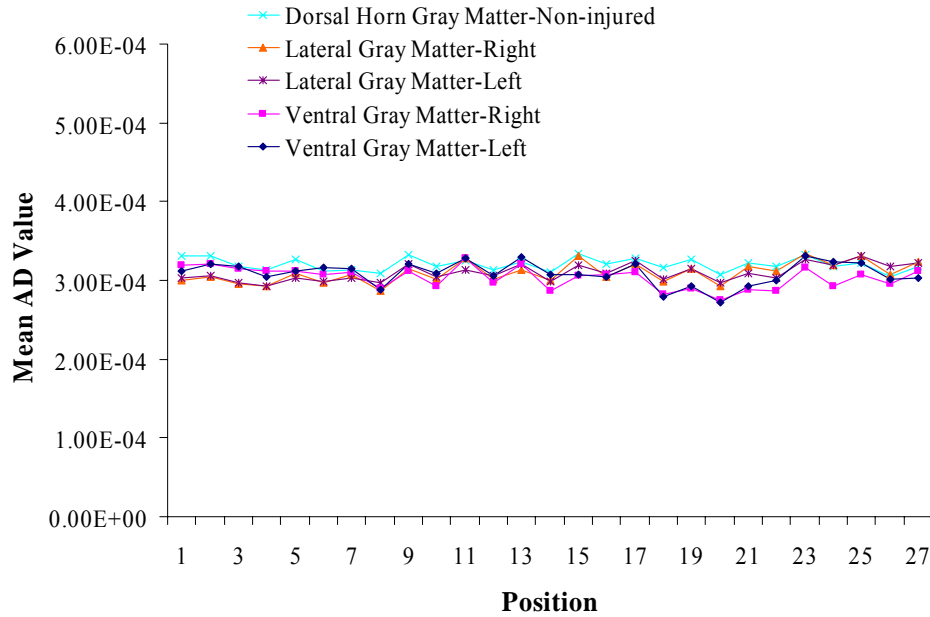


A

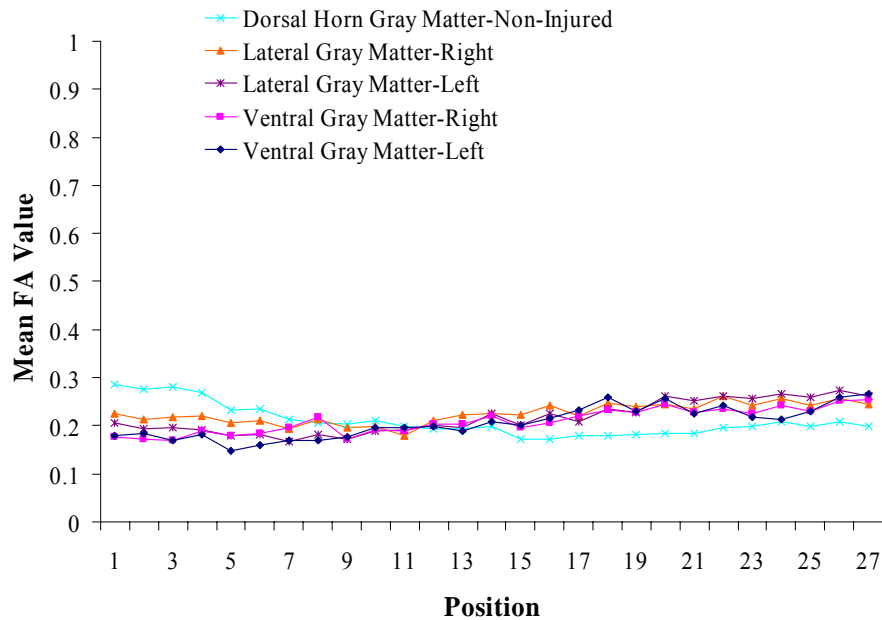


B

Figure 5-5. Average diffusivity and fractional anisotropy values for QUIS-SCI white matter. Position is rostral (left side of graph) to caudal (right side of graph). (A) Average diffusivity along the rostral-caudal axis of white matter is consistent, slightly increasing from rostral to caudal. No significant differences were detected between any of the control white matter regions for either of the measurements. (B) There was a slight decrease in FA from rostral to caudal for all white matter regions.

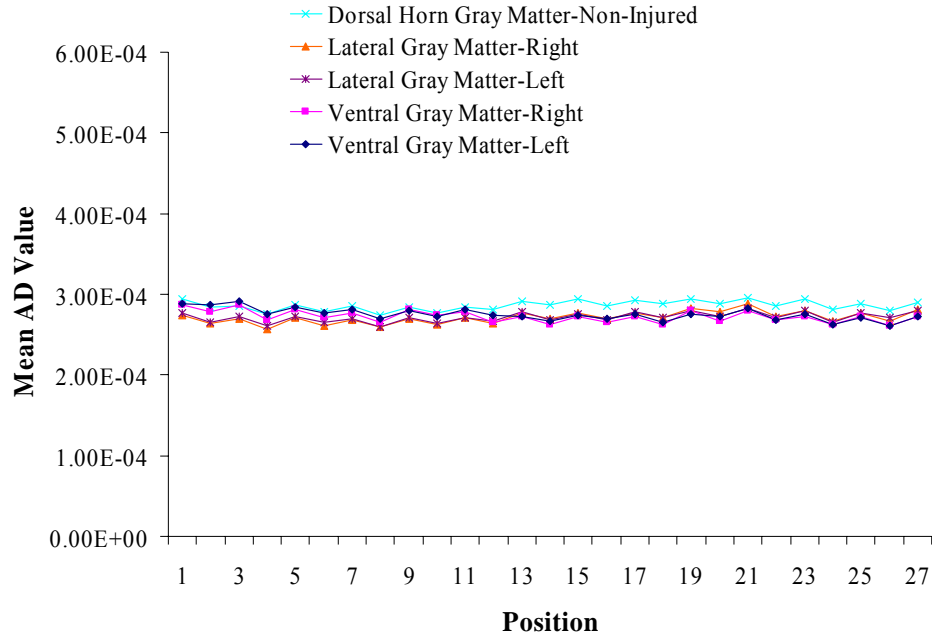


A

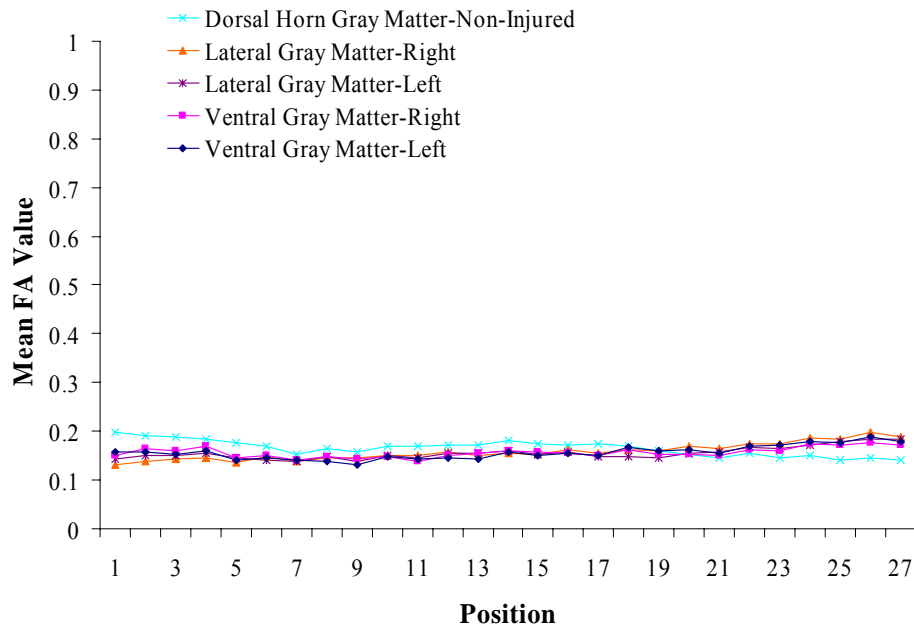


B

Figure 5-6. Average diffusivity and fractional anisotropy values for Control gray matter. Position is rostral (left side of graph) to caudal (right side of graph). (A) Average diffusivity along the rostral-caudal axis of gray matter is consistent from rostral to caudal. No significant differences were detected between any of the control white matter regions for either of the measurements. (B) Fractional anisotropy values also remain consistent from rostral to caudal for all gray matter regions.

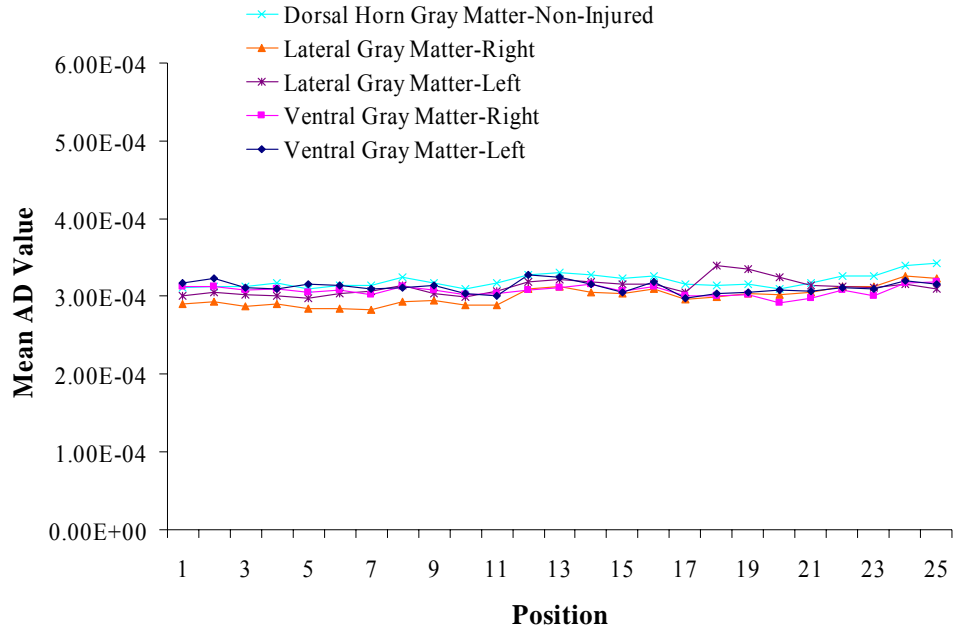


A

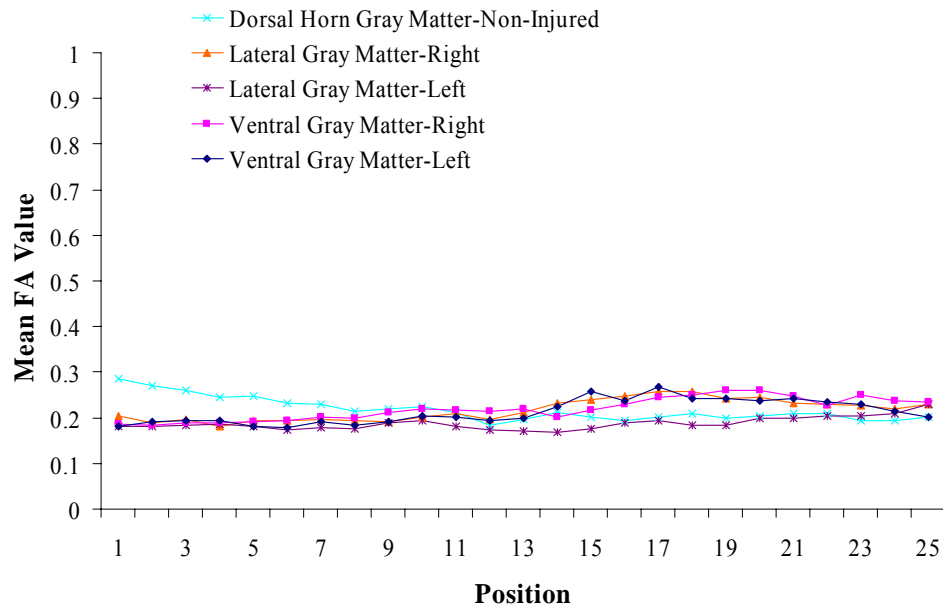


B

Figure 5-7. Average diffusivity and fractional anisotropy values for Saline-SCI gray matter. Position is rostral (left side of graph) to caudal (right side of graph). (A) Average diffusivity along the rostral-caudal axis of gray matter is consistent from rostral to caudal. No significant differences were detected between any of the control white matter regions for either of the measurements. (B) Fractional anisotropy values also remain consistent from rostral to caudal for all gray matter regions.



A



B

Figure 5-8. Average diffusivity and fractional anisotropy values for QUIS-SCI gray matter. Position is rostral (left side of graph) to caudal (right side of graph). (A) Average diffusivity along the rostral-caudal axis of gray matter is consistent from rostral to caudal. No significant differences were detected between any of the control white matter regions for either of the measurements. (B) Fractional anisotropy values also remain consistent from rostral to caudal for all gray matter regions.

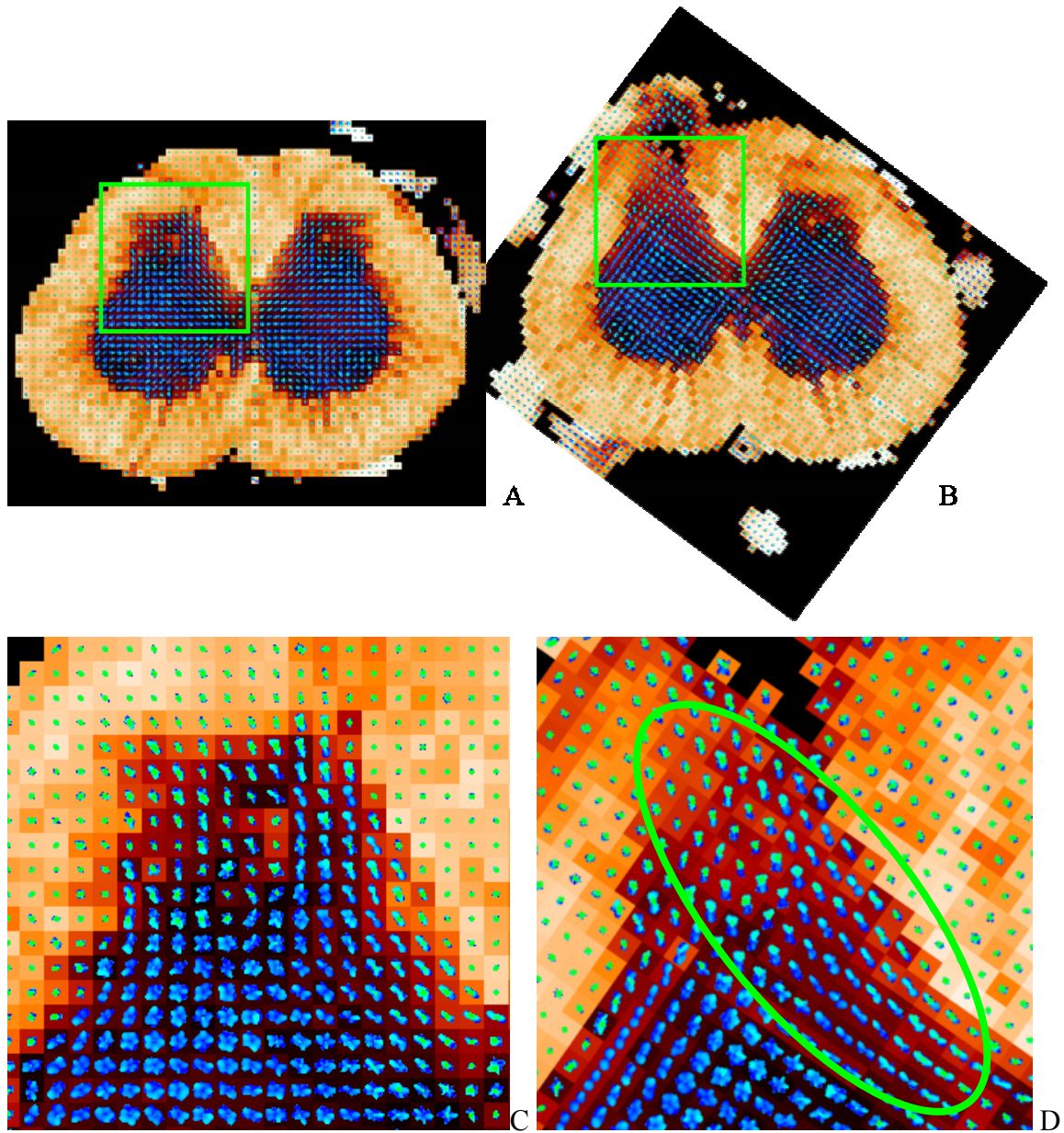


Figure 5-9. Probability maps calculated from diffusion weighted datasets collected from excised normal and QUIS injured spinal cords. (C) and (D) are enlargements taken from (A) normal; and (B) QUIS injured spinal cords, respectively. The orientation surfaces are color-coded such that portions in or out of the plane of section are blue and green, respectively. Notice the loss of complexity of fiber structure in the dorsal horn, specifically along the medial regions (green circle) in the QUIS injured cord.

While comparing the effects of a QUIS lesion (Fig. 5-9 B, D) versus Control (Fig. 5-9A, C), a loss of complexity in gray matter fiber structure is observed in the QUIS-SCI group. There appears to be a change in fiber orientation or a lining up of fibers along the medial dorsal horn gray matter (Fig. 5-9D, green circle) in the injured cord compared to a control cord. No changes were observed in fiber structure or orientation in the white matter or ventral regions of the gray matter in the QUIS injured cords.

Discussion

The goal of the present study was to use diffusion weighted MR imaging to evaluate changes in white and gray matter fibers in the spinal cord following excitotoxic injury. Major findings include: (1) DWI can be used to quantitatively and qualitatively study excitotoxic spinal cord injury; and (2) DWI has the sensitivity to detect changes in gray matter fiber structure between control (non-injured) and QUIS lesioned cords.

Differences were observed in FA and AD values between white and gray matter as expected. Their diffusion characteristics differ because of differences in their structural makeup. Gray matter consists of cell bodies and is reasonably unrestricted, with more random directionality in water diffusion (Moseley et al., 1990) than white matter. In contrast, white matter consists of long parallel bundles of myelinated axons, where water diffusion is mainly restricted to the long or rostrocaudal axis of the cord (Moseley et al., 1990). Thus, FA values in gray matter were lower than those in white matter and conversely, AD values higher in gray matter than white matter, because gray matter is considered more isotropic (unrestricted diffusion in all directions), whereas, diffusion in white matter is considered anisotropic (restricted diffusion in one direction).

With DOT, fiber structure and orientation in the white matter was fairly uniform. Contrastingly, fiber orientation in the gray matter varied among dorsal and ventral

regions. Fibers situated in the ventral regions of the gray matter appear to be more complex than those in the dorsal regions of the dorsal horn. This is because propriospinal connections involving laminae IV–VII are far more extensive within and between segments than those involving more superficial laminae (Yeziarski et al., 1980; Menetrey et al., 1985). Since DOT was able to define fiber orientation and had the sensitivity to detect changes following injury, it may be possible to apply this technique to gain further insight into the differences seen with the two different injury strategies described in Chapter 3 and ultimately more details about the timing of events and the resolution of spatial location of pathologic changes following spinal injury could finally be discovered.

When comparing FA and AD values in different regions of the cord, in Control and QUIS-SCI groups, results were three-fold. First, there were no differences in FA or AD values in any of the regions of white (6 ROI's) or gray matter (5 ROI's), separately, meaning all white matter in a particular section had similar values; the same being true for gray matter. However, values varied slightly along the rostrocaudal axis of the cord because of the change in structural makeup. Secondly, results predictably revealed no significant differences in FA or AD values in the white matter, because the QUIS lesion is a gray matter lesion. Thirdly, results surprisingly showed that there were no significant differences between Control and QUIS-SCI groups in the gray matter. A loss in FA and an increase in AD were expected in the QUIS-SCI group around the injury site in the initial analysis versus Control. Explanations might be that the method of analysis did not have the sensitivity to detect changes in FA or AD values for this particular injury model (i.e., changes may have been too subtle).

With this in mind, DOT analysis was then used to evaluate fiber structure in both white and gray matter. DOT, an accurate and fast technique for fiber orientation mapping (Özarslan et al., 2005), is a relatively new method for DWI analysis with far greater sensitivity in detecting changes in fibers following injury. With this method, it was then possible to identify fiber structure changes in the QUIS lesioned cord. QUIS-SCI animals showed a loss in complexity of fiber structure in the dorsal horn, specifically along the medial regions in the gray matter compared to Control. This may be attributed to a loss in fibers, a re-growth of fibers in a different orientation, or perhaps a reorganization of fibers in the post-injury state. The changes observed are likely a loss in fibers versus a re-growth or re-organization because QUIS lesions result in excitotoxic cell death of the gray matter. Future histological analysis will be critical in evaluating and validating these changes, in order to resolve these differences.

Experimentally, diffusion weighted MRI has given researchers a new tool to study disease and injury. Diffusion weighted MR imaging in *ex vivo* studies of spinal cord injury have been shown to be more sensitive in detecting changes in areas surrounding a contusion injury than conventional MRI (Ford et al., 1994a). It is also more sensitive than conventional MR techniques in early detection of cavity formation following excitotoxic spinal cord injury (Schwartz et al., 1999b). Additionally, Nevo et al. (2001) used DWI to study neuroprotection following a contusion injury in rats and found the method successful in evaluating neuroprotective effects and that the results corresponded with behavioral outcome. Diffusion weighted MRI has also proven to be a successful method in assessing the effects of brain derived neurotrophic factor secreting fibroblasts following spinal injury (Schwartz et al., 2003). This technique shows considerable

possibilities and has higher sensitivity in revealing pathology that would otherwise not show on conventional MR images.

Diffusion weighted imaging has also become a valuable tool in the clinical setting. Diffusion weighted MR images have been used to show diffusion changes within the spinal cord, which can sometimes be missed with conventional MRI, showing no signal abnormality, as demonstrated in patients with canal stenosis (Clark and Werring, 2002). Diffusion weighted MRI has also become an established method for the evaluation and early diagnosis of acute cerebral ischemia (van Gelderen et al., 1994; Schlaug et al., 1997; Lövblad et al., 1998; Loher et al., 2003). With Wallerian degeneration, there is a change in signal intensity as seen with conventional MRI; however, they cannot be differentiated from edema (Becerra et al., 1995; Schwartz et al., 2003). Previous diffusion studies using DWI have also shown that water diffusion may be altered in white matter tracts following Wallerian degeneration (Segawa et al., 1993; Beaulieu et al., 1996; Pierpaoli et al., 1996; Makris et al., 1997; Pierpaoli et al., 1998; Castillo and Mukherji, 1999). Ries et al., (2000) used diffusion weighted imaging to investigate patients suffering from narrowing of the cervical cord and concluded that DWI had the sensitivity to detect changes in diffusion characteristics in the cord. They were able to localize structural fiber damage in the spinal cord where T1- and T2-weighted images were unable to detect any lesion. DWI is clearly a useful tool in the investigation of disease, if one puts aside the expense and magnitude of space required in the laboratory.

There are several advantages and disadvantages associated with diffusion weighted MR imaging as compared with conventional MRI and histological methods in tracking neural pathways. It has the capability to provide more detailed information about tissue

structure and integrity than conventional MR methods (Schwartz et al., 2003). Diffusion weighted MRI also has the potential to detect ongoing changes in cerebral and spinal connections, specifically those in neural development and the acute and chronic study of diseases that affect white and gray matter (Rye, 1999). It is exceedingly sensitive in resolving white matter myelination (Sakuma et al., 1991; Wimberger et al., 1995) and determining the involvement of pathways by pathological processes (Makris et al., 1997) and evaluation of acute ischemic stroke (Koroshetz and Gonzalez, 1997; Fisher and Albers, 1999). Additionally, it has the capability to enhance detection and provide insights into the diagnosis and treatment of disorders such as multiple sclerosis, encephalomyelitis, and the leukodystrophies, all of which involve dysfunctional myelinated fibers (Rye, 1999). Unfortunately, however, diffusion weighted imaging cannot resolve individual components of large axon bundles (i.e., afferent and efferent fibers) and there are fiber-tracking difficulties when two pathways are adjacent and diverge near their terminations (Rye, 1999; Basser et al., 2000). Histological methods are advantageous over DWI and remain the gold standard for the visualization of fiber pathways (i.e., Nauta method, electron microscopy) and it is convenient to use (Rye, 1999). However, the use of histological tracer molecules to label pathways has considerable shortcomings because active transport requires viable surgical specimens or post-mortem tissue and inadequate transport prevents visualization of most pathways (Rye, 1999).

CHAPTER 6 CONCLUSION

Summary of Findings

High-resolution MRI can be used to study experimental SCI quantitatively and qualitatively with high field magnets using customized coils and optimized methods. *In vivo* MRI was sensitive enough to detect significant differences in pathological characteristics between two different strategies of injury (QL1 versus QL2). Although significant differences were found among injury lengths calculated from *in vivo* and *in vitro* images, they were within the range of difference in the slice thickness for each method used. These results indicate that *in vivo* MRI may underestimate total injury length by no more than one slice thickness due to volume averaging in the end slices.

High-resolution, *in vivo* MRI methods can also be used to effectively evaluate the progression of pathological changes longitudinally in the same animal. Additionally, *in vivo* MRI has the capability to monitor the efficacy of a pharmacological agent with known neuroprotective properties to protect the injured spinal cord. Results revealed a specific temporal profile of pathological changes (edema, cavitation, and blood vessel leakage) as well as a specific pattern of change in the integrity of the blood-spinal cord-barrier following excitotoxic spinal cord injury. The use of 80 mg/kg agmatine following spinal cord injury has a significant effect on pathological outcomes, specifically blood vessel leakage and edema.

Structure and orientation of white and gray matter fiber tracts can be effectively evaluated with sophisticated diffusion weighted MR imaging methods. Diffusion

weighted MRI had the sensitivity to detect fiber patterns in a normal cord, showing orientation differences between white and gray matter, as well as differences within regions of gray matter. When comparing to Control, DWI also had the capability to detect changes in fibers in a QUIS lesioned spinal cord. Future studies will need to be carried out to understand and validate these changes in fiber orientation.

Future Directions

Numerous experiment ideas arose from the experiments described in Chapters 3-5, as expected. Below is a description of several future studies that would nicely complement the aforementioned experiments.

In order to further understand changes in pathology following the excitotoxic lesion, magnetic resonance spectroscopy (MRS) could be used to gain noninvasive insight into the biochemical changes responsible for the dynamic changes in pathology following spinal cord injury. Currently, it is known that vasoactive substances (e.g., reactive oxygen molecules, bradykinins, histamines, and nitric oxide) are released by trauma-activated endothelial and glial cells, which facilitate the crossing of plasma-derived molecules into the cord, further exacerbating the injury (Hausmann, 2003). Using MRS, it may be possible to discover additional events that take place leading up to and consequences of BSCB disruption. Future studies could also use MRI techniques for the study of angiogenesis as well as examine the use of different contrast agents ('smart contrast agents') for the noninvasive study of gene expression following SCI (Bell and Taylor-Robinson, 2000). These agents have the capability to be 'switched on' in response to physiological changes within a cell. This could lead to a further understanding of events following changes in the integrity of the BSCB. *In vivo* high-resolution MRI could also be used clinically and experimentally to observe neural tissue

transplantation (Reier et al., 1992a; Reier et al., 1992b; Thompson et al., 2001; Wirth et al., 2001) following spinal cord injury at multiple time-points.

Future studies could examine the effects of other neuroprotective agents (e.g., L-Phenylalanine derivatives; Kagiya et al., 2004) using similar outcome measures as those described in previous chapters and compare the efficacy of these agents to agmatine. An obvious future direction will be to correlate the neuroprotective effects with functional outcomes. Additionally, agmatine could be analyzed further, using other outcome measures at multiple time-points (e.g., Yu and Yeziarski, 2004).

Diffusion weighted MR imaging is becoming an undeniably valuable tool in understanding changes in spinal cord fiber tracts following spinal injury. Chapter 5 involved comparing normal and QUIS lesioned cords. Histology, which serves a gold standard for the visualization of fiber pathways, can be done to further comprehend and verify the changes observed. Additionally, once these changes are confirmed, DWI could then be used to further understand the neuroprotective effects of agmatine, as well as other treatment regimens. With continued improvements to these techniques, more details about the timing of events and the resolution of spatial location of pathologic changes following spinal injury could finally be discovered.

LIST OF REFERENCES

- Abraham KE, McGinty JF, Brewer KL. Spinal and supraspinal changes in opioid mRNA expression are related to the onset of pain behaviors following excitotoxic spinal cord injury. *Pain* 2001; 90:181-90.
- Akins PT, Atkinson RP. Glutamate AMPA receptor antagonist treatment for ischemic stroke. *Curr Med Res Opin* 2002;18:9-13.
- Albers GW, Atkinson RP, Kelley RE, Rosenbaum DM. Safety, tolerability, and pharmacokinetics of the NMDA antagonist dextrorphan in patients with acute stroke. *Stroke* 1995; 26:254-258.
- Amar AP, Levy ML. Pathogenesis and pharmacological strategies for mitigating secondary damage in acute spinal cord injury. *Neurosurgery* 1999; 44:1027-1040.
- Anderson D, Hall E. Pathophysiology of spinal cord trauma. *Ann Emerg Med* 1993; 22:987-992.
- Anderson DK, Demediuk P, Saunders RD, Dugan LL, Means ED, Horrocks LA. Spinal cord injury and protection. *Ann Emerg Med* 1985; 14:816-21.
- Anis N, Sherby S, Goodnow R Jr, Niwa M, Konno K, Kallimopoulos T, Bukownik R, Nakanishi K, Usherwood P, Eldefrawi A. Structure-activity relationships of philanthotoxin analogs and polyamines on N-methyl-D-aspartate and nicotinic acetylcholine receptors. *J Pharmacol Exp Ther* 1990; 254:764-773.
- Auguet M, Viossat I, Marin JG, Chabrier PE. Selective inhibition of inducible nitric oxide synthase by agmatine. *Jpn J Pharmacol* 1995; 69:285-287.
- Bancroft JD, Cook HC. Pigments. In: *Manual of Histological Techniques*. Edinburgh: Churchill Livingstone; 1984:151-152.
- Bareyre FM, Schwab ME. Inflammation degeneration and regeneration in the injured spinal cord: insights from DNA microarrays. *Trends Neurosci* 2003; 26:555-563.
- Basser PJ, Pajevic S, Pierpaoli C, Duda J, Aldroubi A. *In vivo* fiber tractography using DT-MRI data. *Magn Reson Med* 2000; 44:625-632.
- Beaulieu C. The basis of anisotropic water diffusion in the nervous system: a technical review. *NMR Biomed* 2002; 15:435-455.

- Beaulieu C, Does MD, Snyder RE, Allen PS. Changes in water diffusion due to Wallerian degeneration in peripheral nerve. *Magn Reson Med* 1996; 36:627-631.
- Becerra JL, Puckett WR, Hiester ED, Quencer RM, Marcillo AE, Donovan Post MJ, Bunge RPA. MR-pathologic comparisons of Wallerian degeneration in spinal cord injury. *Am J Neuroradiol* 1995; 16:125-133.
- Berens SA, Colvin DC, Yu CG, Yeziarski RP, Mareci TH. Evaluation of the pathologic characteristics of excitotoxic spinal cord injury with MR imaging. *AJNR Am J Neuroradiol* 2005; 26:1612-1622.
- Berens SA, Yeziarski RP, Mareci TH. Application of In Vivo Magnetic Resonance Imaging to Define the Pathological Characteristics of Excitotoxic Spinal Cord Injury. National Neurotrauma Symposium Abstract, November 2003, Biloxi, MS.
- Berens SA, Yeziarski RP, Mareci TH. Use of MRI to Study the Neuroprotective Effects of Agmatine Following Excitotoxic SCI in the Rat. National Neurotrauma Society Symposium Abstract, October 2004, San Diego, CA.
- Beck BL, Jenkins KA, Rocca JR, Fitzsimmons JR. Tissue-equivalent phantoms for high frequencies. *Magn Reson Engineering* 2004; 20B:30-33.
- Bell JD, Taylor-Robinson SD. Assessing gene expression *in vivo*: magnetic resonance imaging and spectroscopy. *Gene Ther* 2000; 7:1259-1264.
- Bilgen M, Abbe R, Liu SJ, Narayana PA. Spatial and temporal evolution of hemorrhage in the hyperacute phase of experimental spinal cord injury: *in vivo* magnetic resonance imaging. *Magn Reson Med* 2000; 43:594-600.
- Bilgen M, Abbe R, Narayana PA. Dynamic contrast-enhanced MRI of experimental spinal cord injury: *in vivo* serial studies. *Magn Reson Med* 2001; 45:614-622.
- Bilgen M, Dogan B, Narayana PA. *In vivo* assessment of blood-spinal cord-barrier permeability: serial dynamic contrast enhanced MRI of spinal cord injury. *Magn Reson Imaging* 2002; 20:337-341.
- Bilgen M, Narayana PA. A pharmacokinetic model for quantitative evaluation of spinal cord injury with dynamic contrast-enhanced magnetic resonance imaging. *Magn Reson Med* 2001; 46:1099 -1106.
- Blight AR, Zimmer MP. Acute spinal cord injury: pharmacotherapy and drug development perspectives. *Curr Opin Investig Drugs* 2001; 2:801-808.
- Bonny JM, Gaviria M, Donnat JP, Jean B, Privat A, Renou JP. Nuclear magnetic resonance microimaging of mouse spinal cord *in vivo*. *Neurobiol Dis* 2004; 15:474-482.

- Bracken MB. Methylprednisolone and acute spinal cord injury: an update of the randomized evidence. *Spine* 2001; 26(24s):s47-s54.
- Bradbury M. Breakdown of the blood-brain barrier. In: *The Concept of a Blood-Brain Barrier*. Chichester, UK: Wiley; 1979:351-382.
- Brewer KL, Yeziarski RP. Effects of adrenal medullary transplants on pain related behaviors following excitotoxic spinal cord injury. *Brain Res* 1998; 798:83-92.
- Brewer KL, Bethea JR, Yeziarski RP. Neuroprotective effects of interleukin-10 following excitotoxic spinal cord injury. *Exp Neurol* 1999; 159:484-493.
- Broadbent AR, Stoodley MA, Watling A, Rogan C, Tu J, Brown CJ, Burke S, Jones NR. The role of excitotoxic injury in post-traumatic syringomyelia. *J Neurotrauma* 2003; 20:883-893.
- Bunge RP, Puckett WR, Becerra JL, Marcillo A, Quencer RM. Observations on the pathology of human spinal cord injury, a review and classification of 22 new cases with details from a case of chronic cord compression with extensive demyelination. *Adv Neurol* 1993; 59:75-89.
- Bunge RP, Puckett WR, Hiester ED. Observations on the pathology of several types of human spinal cord injury, with emphasis on the astrocyte response to penetrating injuries. In: FJ Seil, ed. *Advances in Neurology*. Philadelphia: Lippincott-Raven; 1997:305-315.
- Callaghan PT. *Principles of Nuclear Magnetic Resonance Microscopy*. Oxford: Clarendon Press; 1991.
- Carlson GD, Gorden C. Current developments in spinal cord injury research. *Spine J* 2002; 2:116-128.
- Castillo M, Mukherji SK. Early abnormalities related to postinfarction Wallerian degeneration: evaluation with MR diffusion-weighted imaging. *J Comput Assist Tomogr* 1999; 23:1004-1007.
- Caudle RM, Perez FM, King C, Yu CG, Yeziarski RP. N-methyl-D-aspartate receptor subunit expression and phosphorylation following excitotoxic spinal cord injury in rats. *Neurosci Lett* 2003; 349:37-40.
- Clark CA, Werring DJ. Diffusion tensor imaging in spinal cord: methods and applications -a review. *NMR Biomed* 2002; 15:578-586.
- Crowe M, Bresahan J, Shuman S, Masters JN, Beattie MS. Apoptosis and delayed degeneration after spinal cord injury in rats and monkeys. *Nat Med* 1997; 3:73-76.

- Dumont RJ, Okonkwo DO, Verma S, Hurlbert RJ, Boulos PT, Ellegala DB, Dumont AS. Acute spinal cord injury, part I: pathophysiologic mechanisms. *Clin Neuropharmacol* 2001; 24:254-64.
- Faden AI. Neuroprotection and traumatic brain injury: theoretical option or realistic proposition. *Curr Opin Neurol* 2002; 15:707-712.
- Faden AI, Simon RP. A potential role for excitotoxins in the pathophysiology of spinal cord injury. *Ann Neurol* 1988; 23:623-626.
- Fairbanks CA, Schreiber KL, Brewer KL, Yu CG, Stone LS, Kitto KF, Nguyen HO, Grocholski BM, Shoeman DW, Kehl LJ, Regunathan S, Reis DJ, Yeziarski RP, Wilcox GL. Agmatine reverses pain induced by inflammation, neuropathy, and spinal cord injury. *Proc Natl Acad Sci* 2000; 97:10584-10589.
- Falconer JC, Narayana PA, Bhattacharjee MB, Liu SJ. Quantitative MRI of spinal cord injury in a rat model. *Magn Reson Med* 1994; 32:484-491.
- Fehlings MG, Sekhon LHS, Tator CH. The role and timing of decompression in acute spinal cord injury. *Spine* 2001; 26(24s):s101-s110.
- Fenyés DA, Narayana PA. *In vivo* echo-planar imaging of rat spinal cord. *Magn Reson Imaging* 1998; 16:1249-1255.
- Fisher M, Albers G. Applications of diffusion-perfusion magnetic resonance imaging in acute ischemic stroke. *Neurology* 1999; 52:1750-1756.
- Flanders AE, Schaefer DM, Doan HT, Mishkin MM, Gonzalez CF, Northrup BE. Acute cervical spine trauma: correlation of MR imaging findings with degree of neurologic deficit. *Radiology* 1990; 177:25-33.
- Flanders AE, Spettell CM, Friedman DP, Marino RJ, Herbison GJ. The relationship between the functional abilities of patients with cervical spinal cord injury and the severity of damage revealed by MR imaging. *AJNR Am J Neuroradiol* 1999; 20:926-934.
- Ford JC, Hackney DB, Alsop DC, Jara H, Joseph PM, Hand CM, Black P. MRI characterization of diffusion coefficients in a rat spinal cord injury model. *Magn Reson Med* 1994a; 31:488-494.
- Ford JC, Hackney DB, Joseph PM, Phelan M, Alsop DC, Tabor SL, Hand CM, Markowitz RS, Black P. A method for *in vivo* high resolution MRI of rat spinal cord injury. *Magn Reson Med* 1994b; 31:218-223.
- Fraidakis M, Klason T, Cheng H, Olson L, Spenger C. High-resolution MRI of intact and transected rat spinal cord. *Exp Neurol* 1998; 153:299-312.

- Franconi F, Lemaire L, Marescaux L, Jallet P, Le Jeune JJ. *In vivo* quantitative microimaging of rat spinal cord at 7T. *Magn Reson Med* 2000; 44:893-898.
- Galea B, Regunathan S, Eliopoulos V, Feinstein DL, Reis DJ. Inhibition of mammalian nitric oxide synthases by agmatine, an endogenous polyamine formed by decarboxylation of arginine. *Biochem J* 1996; 316:247-249.
- Gaviria M, Privat A, d'Arbigny P, Kamenka JM, Haton H, Ohanna F. Neuroprotective effects of gacyclidine after experimental photochemical spinal cord lesion in adult rats: dose-window and time-window effects. *J Neurotrauma* 2000; 17:19-30.
- Germano A, Costa C, DeFord SM, Angileri FF, Arcadi F, Pike BR, Bramanti P, Bausano B, Zhao X, Day AL, Anderson DK, Hayes RL. Systemic administration of a calpain inhibitor reduces behavioral deficits and blood-brain barrier permeability changes after experimental subarachnoid hemorrhage in the rat. *J Neurotrauma* 2002; 19:887-96.
- Gilad GM, Gilad VH. Accelerated functional recovery and neuroprotection by agmatine after spinal cord ischemia in rats. *Neurosci Lett* 2000; 196:97-100.
- Gilad GM, Salame K, Rabey JM, Gilad VH. Agmatine treatment is neuroprotective in rodent brain injury models. *Life Sci* 1996; 58:141-146.
- Gorman AL, Yu CG, Ruenes GR, Daniels L, Yeziarski RP. Conditions affecting the onset, severity, and progression of a spontaneous pain-like behavior after excitotoxic spinal cord injury. *J Pain* 2001; 2:229-240.
- Guilfoyle DN, Helpert JA, Lim KO. Diffusion tensor imaging in fixed brain tissue at 7.0T. *NMR Biomed* 2003; 16:77-81.
- Haase A, Frahm J, Hanicke W, Matthaei D. 1H NMR chemical shift selective (CHESS) imaging. *Phys Med Biol* 1985; 30:341-344.
- Hackney DB, Asato R, Joseph PM, Carvlin MJ, McGrath JT, Grossman RI, Kassab EA, DeSimone D. Hemorrhage and edema in acute spinal cord compression: demonstration by MR imaging. *Radiology* 1986; 161:387-390.
- Hains BC, Black JA, Waxman SG. Primary cortical motor neurons undergo apoptosis after axotomizing spinal cord injury. *J Comp Neurol* 2003; 462:328-341.
- Hall ED. Pharmacological treatment of acute spinal cord injury: how do we build on past success? *J Spinal Cord Med* 2001; 24:142-46.
- Hall ED, Yonkers PA, Andrus PK, Cox JW, Anderson DK. Biochemistry and pharmacology of lipid antioxidants in acute brain and spinal cord injury. *J Neurotrauma* 1992; 9(2S):s425-s442.

- Hao JX, Xu XJ, Aldskogius H, Sieger A, Wiesenfeld-Hallin Z. The excitatory amino acid receptor antagonist MK-801 prevents the hypersensitivity induced by spinal cord ischemia in the rat. *Exp Neurol* 1991; 113:182-191.
- Hausmann ON. Post-traumatic inflammation following spinal cord injury. *Spinal Cord* 2003; 41:369-378.
- Hausmann ON, Fouad K, Wallimann T, Schwab ME. Protective effects of oral creatine supplementation on spinal cord injury in rats. *Spinal Cord* 2002; 40:449-456.
- Hong H, Liu GQ. Current status and perspectives on the development of neuroprotectants for ischemic cerebrovascular disease. *Drugs Today (Barc)* 2003; 39:213-22.
- Hulsebosch CE. Recent advances in pathophysiology and treatment of spinal cord injury. *Adv Physiol Educ* 2002; 26:238-255.
- Iannotti C, Li H, Stemmler M, Perman WH, Xu XM. Identification of regenerative tissue cables using *in vivo* MRI after spinal cord hemisection and Schwann cell bridging transplantation. *J Neurotrauma* 2002; 19:1543-1554.
- Ishida Y, Tominaga T. Predictors of neurologic recovery in acute central cervical cord injury with upper extremity impairment. *Spine* 2002; 27:1652-1657.
- Kakulas BA. The clinical neuropathology of spinal cord injury: a guide to the future. *Paraplegia* 1987; 25:212-216.
- Koroshetz W, Gonzalez G. Diffusion-weighted MRI: an ECG for "brain attack"? *Ann Neurol* 1997; 41:565-566.
- Kwon BK, Tetzlaff W, Grauer JN, Beiner J, Vaccaro AR. Pathophysiology and pharmacologic treatment of acute spinal cord injury. *Spine J* 2004; 4:451-464.
- Lee BH, Lee KH, Kim UJ, Yoon do H, Sohn JH, Choi SS, Yi IG, Park YG. Injury in the spinal cord may produce cell death in the brain. *Brain Res* 2004; 1020:37-44.
- Lemaire C, Duncan EG, Solsberg MD, Armstrong RL. *In vitro* magnetic resonance microimaging of the spinal cord. *Magn Reson Med* 1990; 14:97-104.
- Li G, Regunathan S, Barrow CJ, Eshragi J, Cooper R, Reis DJ. Agmatine: an endogenous clonidine-displacing substance in the brain. *Science* 1994; 263:966-969.
- Li G, Regunathan S, Reis DJ. Agmatine is synthesized by a mitochondrial arginine decarboxylase in rat brain. *Ann NY Acad Sci* 1995; 763:325-329.
- Li GL, Brodin G, Farooque M, Funa K, Holtz A, Wang, WL, Oisson Y. Apoptosis and expression of Bcl-2 after compression trauma to rat spinal cord. *J Neuropathol Exp Neurol* 1996; 55:280-289.

- Liu S, Ruenes GL, Yeziarski RP. NMDA and non-NMDA receptor antagonists protect against excitotoxic spinal cord injury in the rat. *Brain Res* 1997; 756:160-167.
- Loher TJ, Bassetti CL, Lövblad KO, Stepper FP, Sturzenegger M, Kiefer C, Nedeltchev K, Arnold M, Remonda L, Schroth G. Diffusion-weighted MRI in acute spinal cord ischaemia. *Neuroradiol* 2003; 45:557-561.
- Lövblad KO, Laubach HJ, Baird AE, Curtin F, Schlaug G, Edelman RR, Warach S. Clinical experience with diffusion-weighted MR in patients with acute stroke. *AJNR* 1998; 19:1061-1066.
- Lu J, Ashwell KWS, Waite P. Advances in spinal cord injury: role of apoptosis. *Spine* 2000; 25:1859-1866.
- Madsen PW, Yeziarski RP, Holets VR. Syringomyelia: clinical observations and experimental studies. *J Neurotrauma* 1994; 11:241-254.
- Makris N, Worth AJ, Sorensen AG, Papadimitriou GM, Wu O, Reese TG, Wedeen VJ, Davis TL, Stakes JW, Caviness VS, Kaplan E, Rosen BR, Pandya DN, Kennedy DN. Morphometry of *in vivo* human white matter association pathways with diffusion-weighted magnetic resonance imaging. *Ann Neurol* 1997; 42:951-962.
- Martinez-Vila E, Sieira PI. Current status and perspectives of neuroprotection in ischemic stroke treatment. *Cerebrovasc Dis* 2001; 11 :60-70.
- Matute C, Sanchez-Gomez MV, Martinez-Millan L, Miledi R. Glutamate receptor-mediated toxicity in optic nerve oligodendrocytes. *PNAS Proc Natl Acad Sci* 1997; 94:8830-8835.
- McDonald JW, Levine JM, Qu Y. Multiple classes of the oligodendrocyte lineage are highly vulnerable to excitotoxicity. *NeuroReport* 1998; 9:2757-2762.
- Melhem ER, Mori S, Mukundan G, Kraut MA, Pomper MG, van Zijl PC. Diffusion tensor MR imaging of the brain and white matter tractography. *AJR Am J Roentgenol* 2002; 178:3-16.
- Menetrey D, de Pommery J, Roudier F. Propriospinal fibers reaching the lumbar enlargement in the rat. *Neurosci Lett* 1985; 31:257-261.
- Metz GA, Curt A, van de Meent H, Klusman I, Schwab ME, Dietz V. Validation of the weight-drop contusion model in rats: a comparative study of human spinal cord injury. *J Neurotrauma* 2000; 17:1-17.
- Mills CD, Fullwood SD, Hulsebosch CE. Changes in metabotropic glutamate receptor expression following spinal cord injury. *Exp Neurol* 2001; 170:244-257.

- Morrow TJ, Paulson PE, Brewer KL, Yezierski RP, Casey KL. Chronic, selective forebrain responses to excitotoxic dorsal horn injury. *Exp. Neurol.* 2000; 161:220-226.
- Moseley ME, Cohen Y, Kucharczyk J, Mintorovitch J, Asgari HS, Wendland MF, Tsuruda J, Norman D. Diffusion-weighted MR imaging of anisotropic water diffusion in cat central nervous system. *Radiology* 1990; 176:439-445.
- Nag S, Riopelle RJ. Spinal neuronal pathology associated with continuous intrathecal infusion of N-methyl-D-aspartate in the rat. *Acta Neuropath (Berl)* 1990; 81:7-13.
- Narayana P, Abbe R, Liu S, Johnston D. Does loss of gray- and white-matter contrast in injured spinal cord signify secondary injury? *In vivo* longitudinal studies. *Magn Reson Med* 1999; 41:315-320.
- Nevo U, Hauben E, Yoles E, Agranov E, Akselrod S, Schwartz M, Neeman M. Diffusion anisotropy MRI for quantitative assessment of recovery in injured rat spinal cord. *Magn Reson Med* 2001; 45:1-9.
- Nguyen HOX, Gorackle-Postle CJ, Kaminski LL, Overland AC, Morgan AD, Fairbanks CA. Neuropharmacokinetic and dynamic studies of agmatine (decarboxylated arginine). *Ann NY Acad Sci* 2003; 1009:82-105.
- Oakes WJ. Chiari malformations, hydromyelia, syringomyelia. In: Wilkins RH, Rengachary SS, eds. *Neurosurgery*. New York: McGraw-Hill; 1996:3593-3616.
- Ohshio I, Hatayama A, Kaneda K, Takahara M, Nagashima K. Correlation between Histopathologic features and magnetic resonance images of spinal cord lesions. *Spine* 1993; 18:1140-1149.
- Ohta K, Fujimura Y, Watanabe M, Yato Y. Experimental study on MRI evaluation of the course of cervical spinal cord injury. *Spinal Cord* 1999; 37:580-584.
- Olmos G, DeGregorio-Rocasolano N, Paz Regalado M, et al. Protection by imidazo (ine) drugs and agmatine of glutamate-induced neurotoxicity in cultured cerebellar granule cells through blockade of NMDA receptor. *Br J Pharmacol* 1999; 127:1317-1326.
- Özarslan E, Shepard TM, Vemuri BC, Blackband SJ, Mareci TH. Resolution of complex tissue microarchitecture using the diffusion orientation transform (DOT). *Neuroimage* 2006; 31:1086-1103.
- Park E, Velumian AA, Fehlings MG. The role of excitotoxicity in secondary mechanisms of spinal cord injury: a review with an emphasis on the implications for white matter degeneration. *J Neurotrauma* 2004; 21:754-774.

- Pattany PM, Widerstrom-Noga E, Bowen BC, Martinez-Arizala A, Garcia BR, Cuevo E, Quencer RM, Yeziarski RP. Proton magnetic spectroscopy following spinal cord injury: evaluation of patients with chronic neuropathic pain. In: Yeziarski RP, Burchiel K, eds. *Spinal Cord Injury Pain: Assessment, Mechanisms, Management*. Seattle: IASP Press; 2002:301-311.
- Pierpaoli C, Barnett A, Penix L, De Graba T, Basser PJ, Di Chiro G. Identification of fiber degeneration and organized gliosis in stroke patients by diffusion tensor MRI. *ISMRM Proc* 1996; 563.
- Pierpaoli C, Barnett A, Virta A, Penix L, Chen R. Diffusion MRI of Wallerian degeneration. A new tool to investigate neural connectivity *in vivo*? *ISMRM Proc* 1998; 1247.
- Piletz JE, May PJ, Wang G, Zhu H. Agmatine crosses the blood-brain barrier. *Ann NY Acad Sci* 2003; 1009:64-74.
- Plunkett JA, Yu CG, Easton J, Bethea JR, Yeziarski RP. Effects of interleukin-10 (IL-10) on pain behavior and gene expression following excitotoxic spinal cord injury in the rat. *Exp Neurol* 2001; 168:144-154.
- Popovich PG, Horner PJ, Mullin BB, Stokes BT. A quantitative spatial analysis of the blood-spinal cord barrier. I. permeability changes after experimental spinal contusion injury. *Exp Neurol* 1996; 142:258-275.
- Profyris C, Cheema SS, Zang D, Azari MF, Boyle, Petratos S. Degenerative and regenerative mechanisms governing spinal cord injury. *Neurobiol Dis* 2004; 15:415-436.
- Purves D, Augustine GJ, Chikaraishi DM, Fitzpatrick D, Katz LC, LaMantia AS, McNamara JO. *Neuroscience*. 2nd ed. Sunderland: Sinauer Associates, Inc; 2001:38.
- Rabchevsky AG, Fugaccia I, Sullivan PG, Blades DA, Scheff SW. Efficacy of methylprednisolone therapy for the injured rat spinal cord. *J Neuroscience Res* 2002; 68:7-18.
- Rapoport SI. Pathological alterations of the blood brain barrier. In: *Blood-Brain Barrier in Physiology and Medicine*. New York: Raven Press; 1976:129-152.
- Ratliff J, Voorhies R. Increased MRI signal intensity in association with myelopathy and cervical instability: case report and review of the literature. *Surg Neurol* 2000; 53:8-13.
- Regan R, Choi DW. Excitotoxicity and central nervous system trauma. In: Salzman FK and Faden AL, eds. *The Neurobiology of Central Nervous System Trauma*. New York: Oxford Press; 1994:173-181.

- Reier PJ, Anderson DK, Thompson FJ, Stokes BT. Neural tissue transplantation and CNS trauma: anatomical and functional repair of the injured spinal cord. *J Neurotrauma* 1992a; 9S:s223-s248.
- Reier PJ, Stokes BT, Thompson FJ, Anderson DK. Fetal cell grafts into resection and contusion/compression injuries of the rat and cat spinal cord. *Exp Neurol* 1992b; 115:177-188.
- Reis M, Jones RA, Dousset V, Moonen CTW. Diffusion tensor MRI of the spinal cord. *Magn Reson Med* 2000; 44:884-892.
- Reis DJ, Regunathan S. Agmatine: a novel neurotransmitter? *Adv Pharmacol* 1998; 42:645-649.
- Reis DJ, Yang XC, Milner TA. Agmatine containing axon terminals in rat hippocampus form synapses on pyramidal cells. *Neurosci Lett* 1998; 250:185-188.
- Runge VM, Wells JW, Baldwin SA, Scheff SW, Blades DA. Evaluation of the temporal evolution of acute spinal cord injury. *Invest Radiol* 1997; 32:105-110.
- Rye DB. Tracking neural pathways with MRI. *TINS* 1999; 22:373-374.
- Sakuma H, Nomura Y, Takeda K, Tagami T, Nakagawa T, Tamagawa Y, Ishii Y, Tsukamoto T. Adult and neonatal human brain: diffusional anisotropy and myelination with diffusion-weighted MR imaging. *Radiology* 1991; 180:229-233.
- Sastre M, Regunathan S, Galae E, Reis DJ. Agmatinase activity in rat brain: a metabolic pathway for the degradation of agmatine. *J Neurochem* 1996; 67:1761-1765.
- Sastre M, Regunathan S, Reis DJ. Agmatine is transported by a specific uptake system into rat brain synaptosomes. *J Neurochem* 1997; 69:2421-2426.
- Schlaug G, Siewart B, Benfield A, Edelman PR, Warach S. Time course of the apparent diffusion coefficient (ADC) abnormality in human stroke. *Neurology* 1997; 49:113-119.
- Schwartz ED, Chin C, Shumsky JS, Jawad AF, Brown BK, Wehrli S, Tessler A, Murray M, Hackney DB. Apparent diffusion coefficients within spinal cord transplants and surrounding white matter correlate with degree of axonal dieback following injury. *Am J Neuroradiol* 2005; 26:7-18.
- Schwartz ED, Falcone SF, Quencer RM, Green BA. Posttraumatic syringomyelia: pathogenesis, imaging, and treatment. *AJNR Am J Neuroradiol* 1999a; 173:487-492.
- Schwartz ED, Hackney DB. Diffusion-weighted MRI and the evaluation of spinal cord axonal integrity following injury and treatment. *Exp Neurol* 2003; 84:570-589.

- Schwartz ED, Shumsky JS, Wehrli S, Tessler A, Murray M, Hackney DB. *Ex vivo* MR determined apparent diffusion coefficients correlate with motor recovery mediated by intraspinal transplants of fibroblasts genetically modified to express BDNF. *Exp Neurol* 2003; 182:49-63.
- Schwartz ED, Yeziarski RP, Pattany PM, Quencer RM, Weaver RG. Diffusion-weighted MR imaging in a rat model of syringomyelia after excitotoxic spinal cord injury. *AJNR Am J Neuroradiol* 1999b; 20:1422-1428.
- Segawa F, Kinoshita J, Kishibayashi K, Kamada K, Sunohara K, Shimizu Y, Hashimoto Y. Diffusion images of Wallerian degeneration. *ISMRM Proc* 1993; 595.
- Sekhon LHS, Fehlings MG. Epidemiology, demographic, and pathophysiology of acute spinal cord injury. *Spine* 2001; 26(24S):S2-S12.
- Selden NR, Quint DJ, Patel N, d'Arcy HS, Papadopoulos SM. Emergency magnetic resonance imaging of cervical spinal cord injuries: clinical correlation and prognosis. *Neurosurgery* 1999; 44:785-792.
- Siddall PJ, Yeziarski RP, Loeser JD. Taxonomy and epidemiology of spinal cord injury pain. In: Yeziarski RP, Burchiel K eds. *Spinal Cord Injury Pain: Assessment, Mechanisms, Management*. Seattle: IASP Press; 2002.
- Silver X, Ni X, Mercer EV, Beck BL, Bossart EL, Inglis B, Mareci TH. *In vivo* 1H magnetic resonance imaging and spectroscopy of the rat spinal cord using an inductively-coupled chronically implanted RF coil. *Magn Reson Med* 2001; 46:1216-1222.
- Springer JE, Asbill RD, Knapp PE. Activation of the caspase-3 apoptotic cascade in traumatic spinal cord injury. *Nat Med* 1999; 5:943-946.
- Stokes BT, Fox P, Hollinden G. Extracellular calcium activity in the injured spinal cord. *Exp Neurol* 1983; 80:561-572.
- Tator CH. Review of experimental spinal cord injury with emphasis on the local and systemic circulatory effects. *Neurochirurgie* 1991; 37:291-302.
- Tator CH, Fehlings MG. Review of the secondary injury theory of acute spinal cord trauma with emphasis on vascular mechanisms. *J Neurosurg* 1991; 75:15-26.
- Tator CH, Koyanagi I. Vascular mechanisms in the pathophysiology of human spinal cord injury. *J Neurosurg* 1997; 86:483-492.
- Tekkok S, Goldberg MP. AMPA/kainite receptor activation mediates hypoxic oligodendrocyte death and axonal injury in cerebral white matter. *J Neurosci* 2001; 21:4237-4248.

- Thomalla G, Glauche V, Koch MA, Beaulieu C, Weiller C, Rother J. Diffusion tensor imaging detects early wallerian degeneration of the pyramidal tract after ischemic stroke. *Neuroimage* 2004; 22:1767-74.
- Thompson FJ, Reier PJ, Uthman B, Mott S, Fessler RG, Behrman A, Trimble M, Anderson DK, Wirth ED III. Neurophysiological assessment of the feasibility and safety of neural tissue transplantation in patients with syringomyelia. *J Neurotrauma* 2001; 18:931-945.
- Tuch DS, Reese TG, Wiegell MR, Makris N, Belliveau JW, Wedeen VJ. High angular resolution diffusion imaging reveals intravoxel white matter fiber heterogeneity. *Magn Reson Med* 2002; 48:577-582.
- van Gelderen P, Vleeschouwer MHM, DesPres D, Pekar J, van Zijl PCM, Moonen CTW. Water diffusion in acute stroke. *Magn Reson Med* 1994; 31:154-163.
- Weirich SD, Cotler HB, Narayana PA, Hazle JD, Jackson EF, Coupe KJ, McDonald CL, Langford LA, Harris JH Jr. Histopathologic correlation of magnetic resonance imaging signal patterns in a spinal cord injury model. *Spine* 1990; 15:630-638.
- Wells JEA, Hurlbert RJ, Fehlings MG, Yong W. Neuroprotection by minocycline facilitates significant recovery from spinal cord injury in mice. *Brain* 2003; 126:1628-1637.
- Werring DJ, Toosy AT, Clark CA, Parker GJ, Barker GJ, Miller DH, Thompson AJ. Diffusion tensor imaging can detect and quantify corticospinal tract degeneration after stroke. *J Neurol Neurosurg Psychiatry* 2000; 69:269-72.
- Williams B. Post-traumatic syringomyelia, an update. *Paraplegia* 1990; 28:296-313.
- Wimberger DM, Roberts TP, Barkovich AJ, Prayer LM, Moseley ME, Kucharczyk J. Identification of "premyelination" by diffusion-weighted MRI. *J Comput Assist Tomogr* 1995; 19:28-33.
- Wirth ED III, Mareci TH, Beck BL, Fitzsimmons JR, Reier PJ. A comparison of an inductively coupled implanted coil with optimized surface coils for *in vivo* NMR imaging of the spinal cord. *Magn Reson Med* 1993; 30:626-633.
- Wirth ED III, Reier PJ, Fessler RG, Thompson FJ, Uthman B, Behrman A, Beard J, Vierck CJ, Anderson DK. Feasibility and safety of neural tissue transplantation in patients with syringomyelia. *J Neurotrauma* 2001; 18:911-929.
- Wirth ED III, Theele DP, Mareci TH, Anderson DK, Reier PJ. Dynamic assessment of intraspinal neural graft survival using magnetic resonance imaging. *Exp Neurol* 1995; 136:64-72.

- Wirth ED III, Theele DP, Mareci TH, Anderson DK, Brown SA, Reier PJ. *In vivo* magnetic resonance imaging of fetal cat neural tissue transplants in the adult cat spinal cord. *J Neurosurg* 1992; 76:261-274.
- Wirth ED III, Vierck CJ, Reier PJ, Fessler RG, Anderson DK. Correlation of MRI findings with spinal cord injury pain following neural tissue grafting into patients with post-traumatic syringomyelia. In: Yeziarski RP, Burchiel KJ, eds. *Spinal Cord Injury Pain: Assessment, Mechanisms, Management*. Seattle: IASP Press; 2002:313-330.
- Wrathall JR, Choiniere D, Teng YD. Dose-dependent reduction of tissue loss and functional impairment after spinal cord trauma with the AMPA/kainate antagonist NBQX. *J Neurosci* 1994; 14:6598-6607.
- Xu J, Kim GM, Ahmed SH, Xu JM, Yan P, Xu XM, Hsu CY. Glucocorticoid receptor-mediated suppression of activator protein-1 activation and matrix metalloproteinase expression after spinal cord injury. *J Neuroscience* 2001; 21:92-97.
- Yam PS, Dunn LT, Graham DI, Dewar D, McCulloch J. NMDA receptor blockade fails to alter axonal injury in focal cerebral ischemia. *J Cereb Blood Flow Metab* 2000; 20:772-779.
- Yamashita Y, Takahashi M, Matsuno Y. Chronic injuries of the spinal cord: assessment with MR imaging. *Radiology* 1990; 175:849-854.
- Yamashita Y, Takahashi M, Matsuno Y. Acute spinal cord injury: magnetic resonance imaging correlated with myelopathy. *Br J Rad* 1991; 64:201-209.
- Yang XC, Reis DL. Agmatine selectively blocks the NMDA subclass of glutamate receptor channels in rat hippocampal neurons. *J Pharmacol Exp Ther* 1999; 288:544-549.
- Yeziarski RP. Pain following spinal cord injury: pathophysiology and central mechanisms. *Prog Brain Res* 2001; 129:429-449.
- Yeziarski RP. Pathophysiology and animal models of spinal cord injury pain. In: Yeziarski RP, Burchiel K, eds. *Spinal Cord Injury Pain: Assessment, Mechanisms, Management*. Seattle: IASP Press; 2002:117-136.
- Yeziarski RP, Burchiel KJ. Future directions for the study and treatment of spinal cord injury. In: Yeziarski RP, Burchiel K eds. *Spinal Cord Injury Pain: Assessment, Mechanisms, Management*. Seattle: IASP Press; 2002.
- Yeziarski RP, Culberson JL, Brown PB. Cells of origin of propriospinal connections to cat lumbosacral gray as determined with horseradish peroxidase. *Exp Neurol* 1980; 69:493-512.

- Yeziarski RP, Liu S, Ruenes GL, Kajander KL, Brewer KL. Excitotoxic spinal cord injury: Behavior and morphological characteristics of a central pain model. *Pain* 1998; 75:141-155.
- Yeziarski RP, Park SH. The mechanosensitivity of spinal sensory neurons following intraspinal injections of quisqualic acid. *Neurosci Lett* 1993; 157:115-119.
- Yeziarski RP, Santana M, Park SH, Madsen PW. Neuronal degeneration and spinal cavitation following intraspinal injections of quisqualic acid. *J Neurotrauma* 1993; 10:445-456.
- Yong C, Arnold PM, Zoubine MN, Citron BA, Watanabe I, Berman NE, Festof BW. Apoptosis in cellular compartments of rat spinal cord after severe contusion injury. *J Neurotrauma* 1998; 15:459-472.
- Yoshioka A, Bacskai B, Pleasure D. Pathophysiology of oligodendroglial excitotoxicity. *J Neurosci Res* 1996; 46:427-437.
- Young W, Yen V, Blight A. Extracellular calcium ionic activity in experimental contusion injury. *Brain Res* 1982; 253:105-113.
- Yu CG, Marcillo AE, Fairbanks CA, Wilcox GL, Yeziarski RP. Agmatine improves locomotor function and reduces tissue damage following spinal cord injury. *NeuroReport* 2000; 11:3203-3207.
- Yu CG, Fairbanks CA, Wilcox GL, Yeziarski RP. Effects of agmatine, interleukin-10, and cyclosporine on spontaneous pain behavior after excitotoxic spinal cord injury in rats. *J Pain* 2003; 4: 129-140
- Yu CG, Yeziarski RP. Activation of the ERK1/2 signaling cascade by excitotoxic spinal cord injury. *Mol Brain Res* 2005; 138:244-255.
- Yu, CG, Yeziarski RP. Agmatine targets multiple signaling pathways to produce neuroprotective effects following spinal cord injury. *Society for Neuroscience*. 2004; San Diego, CA.
- Zhu MY, Piletz JE, Halavis A, Regunathan S. Effect of agmatine against cell death induced by NMDA and glutamate in neurons and PC12 cells. *Cell Mol Neurobiol* 2003; 23:865-872.

BIOGRAPHICAL SKETCH

Sara Ann Berens was born in Hays, Kansas, in 1979, but grew up in Jacksonville, Florida. During her years at Mandarin High School, Sara was a member of the National Honor Society. Sara also played clarinet and alto clarinet in the band throughout her high school years, during which the band participated and placed highly in numerous marching and concert competitions. After graduating with honors in 1998, Sara enrolled at the University of Florida, becoming a member of the National Society of Collegiate Scholars. Sara had worked all through her undergraduate years, gaining research experience in hopes of attending medical school. She gained valuable laboratory experience as a laboratory stockroom assistant for the organic chemistry lab. Simultaneously, she also began working for Dr. Robert Yeziarski, as an undergraduate laboratory student assistant. However, another professor, Dr. Wolfgang Streit, whom Sara collaborated with, had enlightened her about the graduate opportunities in the University of Florida College of Medicine's Interdisciplinary Program (IDP) in Biomedical Sciences, and she decided that this route was more suited to her interests. Sara graduated with a Bachelor of Science in chemistry in 2002, and entered the IDP program that Fall, where she joined the laboratory of Dr. Yeziarski once again. It was his interest for collaboration with Dr. Thomas H. Mareci that set Sara up for her dissertation work. She played the role as bridge between two collaborators who might not have worked together due to the volume of time and work involved, thereby interconnecting two unrelated fields of expertise. Her dissertation work has focused on the use of

magnetic resonance imaging in the study of the dynamics of excitotoxic spinal cord injury. Upon graduation, Sara hopes to continue her research in a neuroscience related field in the pharmaceutical, medical, or biomedical industry.